PORE-SCALE SIMULATION OF SOLUTE AND COLLOID TRANSPORT AND DIRECT
COMPARISON WITH COLUMN AND MICROFLUIDICS EXPERIMENTS

by

Jae Kyoung Cho

A thesis submitted to the Faculty and the Board of Trustees of the Colorado School of Mines in partial fulfillment of the requirements for the degree of Doctor of Philosophy (Petroleum Engineering).

Golden, Colorado

Date _____

Signed: _____
Jae Kyoung Cho

Signed: _____
Dr. Xiaolong Yin
Thesis Advisor

Golden, Colorado

Date _____

Signed: _____
Dr. Erdal Ozkan
Professor and Department Head
Department of Petroleum Engineering

ABSTRACT

In this study, pore-scale simulation tools to resolve flow and transport using the lattice Boltzmann (LB) method and the random walk particle tracking method (RWPT) were developed to solve advection-diffusion of solute or colloidal particles through porous media. Both LB and RWPT codes were parallelized to enable direct simulations of column and microfluidic experiments, conducted by collaborators, in acceptable computational times. The RWPT code, specifically, can generate tracer concentration profiles at the outlet known as breakthrough curves (BTCs).

To directly compare with column experiments, digitalized images of the columns that contains about 10 million fluid voxels were directly used in LB and RWPT simulations. LB simulation was used to obtain the velocity field in the column. Using the average advection velocity from the LB simulation, input parameters for the RWPT simulation were determined to match the Péclet number of the column experiment. The breakthrough curves of the column experiment for non-adsorbing solutes such as iodide (I^-) agree with those from the experiments. For transport of solute involved in equilibrium sorption-desorption processes between the solution and the porous medium such as cesium ($137Cs^+$), a probabilistic method was developed. Numerical batch experiments were performed to determine the probabilities that reproduce the partition coefficients measured in the experiments. Without relying on curve fitting methods or empirical correlations, RWPT simulations reproduced retarded breakthrough curves matching the experimental data.

To simulate colloid transport experiments conducted in microfluidic porous media models with embedded collectors, which are beads with surface charge that irreversibly adsorbs colloidal particles with finite adsorptive capacities, RWPT was extended to include linear and nonlinear finite adsorptivity models. Flow and transport in bead-based microfluidic porous media analogues with mixed surface charges were simulated. Colloid transport and deposition from simulations were compared to experiments on the level of breakthrough curves. With the inclusion of physics-based electrostatic interaction range and dynamic blocking functions, RWPT simulations captured the kinetics of this complex advection-diffusion-adsorption process and generated breakthrough curves that are in good agreement with the experiments. Lastly, the movement of colloids under

the influence of hydrodynamic lubrication that hinders colloid deposition was modeled as an anisotropic random walk. Preliminary numerical simulations, performed on a body centered cubic (BCC) domain, suggested that near-wall hindered diffusion can facilitate transport of reactive colloids.

TABLE OF CONTENTS

LIST OF FIGURES

viii

LIST OF TABLES

LIST OF SYMBOLS – ENGLISH

Ratio of radius between a particle and a collector .... A

Radius of a spherical particle .... a

Surface area of a bead .... A_s

Effective particle radius .... a^*

Diffusive movement .... $\boldsymbol{B}$

Surface blocking function .... B

Average or effluent solute concentration C

Solute concentration c

Lattice velocity .... c_i

Initial solute concentration .... C_0

Speed of sound .... c_s

Grain diameter .... d

Diffusion coefficient .... D

Dispersion tensor .... $\boldsymbol{D}$

Apparent dispersion coefficient .... D_a

Effective diffusion coefficient .... D_e

Near-wall hindered diffusivity tensor .... $\boldsymbol{D}^H$

Longitudinal dispersion coefficient .... D_L

Mechanical dispersion coefficient .... D_m

Molecular diffusion coefficient .... D_0

Molecular diffusion tensor .... $\boldsymbol{D}_0$

Brownian diffusivity .... D_B

Vertical diffusivity term for hindered diffusion .... $D_\perp^H$

Horizontal diffusivity term for hindered diffusion .... $D_\parallel^H$

Kinetic energy / electron charge .... e

Force vector .... $\boldsymbol{F}$

LIST OF SYMBOLS – OTHERS

ACKNOWLEDGEMENTS

CHAPTER 1

INTRODUCTION

This chapter presents the motivation and objectives of this dissertation. Pore-scale direct numerical models for studying advection-dispersion in porous media is introduced, and the organization of this dissertation follows at the end of this chapter.

1.1 Motivation of pore-scale models

Advection-dispersion of reactive and non-reactive species in porous media is a subject of active research in many branches of science and engineering including biology, hydrology, environmental engineering and petroleum engineering. Practical engineering applications pertaining to this transport phenomenon in porous media include groundwater contamination (Batu 2005; Fetter 2008; Bear and Cheng 2010), bacteria transport in soil (Abu-Ashour et al. 1994), engineered nanoparticle (ENP) transport for soil remediation (Tungittiplakorn et al. 2004), CO_2 sequestration (Molins et al. 2012), radionuclide transport in nuclear waste repository (Flury et al. 2002), flow and diffusion in water and oil reservoirs (Perkins and Johnston 1963).

A large number of transport models have been developed and applied successfully to solve continuum- and field-scale problems. The mathematical foundation for these classical transport models is to apply physical laws such as mass and momentum conservation over a representative element volume (REV) (Wiest 1969; Bear 1972) where effects of small-scale features of porous medium are averaged out. These models are usually in the form of partial differential equations (PDEs), and they are solved analytically or numerically with given initial and boundary conditions. Analytical solutions for some simple problems are still efficient tools to understand and analyze laboratory column experiments, e.g., those for the one dimensional advection-dispersion equation (1D-ADE) (van Genuchten and Wierenga 1976). Analytic models are, however, limited in that they can only be applied to simple systems. For complex problems, numerical solutions are preferred (Rhodes 2008). Transport properties of REV needed to close the transport models, in the past, were usually obtained from laboratory experiments (including empirical correlations developed from laboratory experiments) or derived from theoretical or numerical analysis of smaller systems.

Traditional Eulerian approaches were limited in solving flow and transport in heterogeneous porous media particularly for advection-dominated problems. This limitation was mainly attributed to that the solutions of traditional models are susceptible to numerical dispersion (Jiménez-Hornero et al. 2005). As an alternative to traditional Eulerian approaches in which governing partial differential equations are solved, Lagrangian particle tracking (LPT) methods emerged to solve field-scale ground water contaminant transport problems (Tompson et al. 1987; Ackerer 1988).

With advances in high performance computing and image acquisition / processing techniques, particle tracking methods started to be used to solve pore-scale transport with complex pore and solid geometries explicitly considered, and pore-scale processes that contribute to macroscopic flow and transport explicitly modeled. Salles et al. (1993) applied particle tracking methods to porous media at pore-scale. They performed the pore-scale numerical simulation using random walks to study macroscopic transport coefficients of porous media. They validated their numerical solutions of dispersion tensor with analytic solutions for a plane Poiseuille flow. For arrays of cylinders and spheres, they reproduced dimensionless longitudinal dispersion tensor agreeable with existing data. They extended their approaches to three-dimensional porous medium that was reconstructed from Fontainebleau sandstones. In this line of work, Maier et al. (2000) studied pore-scale Taylor dispersion using the lattice-Boltzmann and random walk particle tracking (RWPT) methods. Flow and transport of tracer in periodic random packings was simulated to evaluate the time-dependent dispersion tensor. The numerical results of pre-asymptotic and asymptotic dispersion coefficients were compared with those from nuclear magnetic resonance (NMR) spectroscopy. In these earlier works, pore-scale simulations focused on obtaining macroscopic transport properties including dispersion coefficients on statistically generated porous medium replicas.

Interests in recent studies include incorporating physio-chemical interactions between transported species and porous surface and simulating column-scale breakthrough experiments of more complex or natural porous media. Hlushkou et al. (2013) employed random walk particle tracking (RWPT) combined with the lattice Boltzmann method to simulate microscopic advective-diffusive transport in statistically generated porous media of chromatographic beds. To study the separation process in chromatography, they incorporated adsorption kinetics of analyte molecules

at the interface of solid and liquid phase. The numerical model was validated using Taylor-Aris dispersion with adsorption-desorption processes on the adsorbent wall of a tube (Hlushkou et al. 2014).

Pham et al. (2014) studied the transport of nanoparticles under advection-diffusion-adsorption through columns packed with spherical particles using LB/RWPT methods. Pore surface retention was modeled using a probability of adsorption and desorption that is pre-assigned to each tracer. They conducted breakthrough experiments in a column randomly packed with spheres. In the simulations, simple ideal packing arrays such as simple cubic, body centered cubic (BCC), and face centered cubic (FCC) were used. Breakthrough curves for conservative tracer were constructed to be compared with theoretical predictions. They also investigated into transport and retention of nanoparticles under surface charge heterogeneity combined with surface blocking conditions. In that study, they analyzed the mineralogy of Berea sandstones based on their micro-CT-scanned images, and then assigned charge heterogeneity to the pore surface.

To simulation laboratory column experiments of nature porous media, Scheibe et al. (2015) performed direct numerical simulations, particularly on the images of decimeter-scale soil column samples that were obtained in a nuclear waste repository. The images of the column samples were captured with X-ray computed tomography (XCT) and reconstructed into computation domains thorough image segmentation processes. They used a multiscale Stoke-Darcy simulation for flow field and solved the advection-diffusion equation to obtain the distribution of solute concentration. Breakthrough curves constructed from their simulations were compared with those from the column experiments.

In this dissertation, we performed pore-scale direct numerical simulations to make direct comparisons with laboratory experiments conducted by collaborators: 1) solute transport experiments conducted in bead-packed columns, and 2) colloid transport experiments conducted in microfluidic porous media analogues packed with engineered beads. To generate realistic computational domains, 1) CT-scanned images of bead-packed columns were processed and assembled, and 2) coordinates and radius of beads in microfluidic devices were used to reconstruct digital replicas. Pore-scale processes including 1) equilibrium adsorption-desorption of solute and 2) irreversible adsorption of colloid were modeled to investigate into the effect of surface-related phenomena on macroscopic transport behavior. As with recent trends in direct simulations of

3

advection-diffusion, our numerical results were compared with those of the laboratory experiments on the level of breakthrough curves. Lattice Boltzmann (LB) and random walk particle tracking (RWPT) codes were parallelized to meet high computational demands in solving flow and advection-dispersion-adsorption of solutes / colloids.

1.2 Objectives

The primary objectives of this research are to 1) develop pore-scale simulation methods for transport of solutes and colloids in porous media with retention, and 2) to directly compare numerical solutions from pore-scale simulations with experimental data on the level of breakthrough curves. On 1) simulation methods for transport, we specifically focus on the random walk particle tracking (RWPT) method, which is also known as Lagrangian particle tracking in the literature (Tompson and Gelhar 1990; Maier et al. 2000; Jiménez-Hornero et al. 2005; Boek and Venturoli 2010; Pham et al. 2014; Scheibe et al. 2015) to solve advection and dispersion in porous media.

To these ends, we first developed a framework of pore-scale numerical methods to simulate decimeter-scale column and millimeter-scale microfluidics experiments. RWPT was massively parallelized to handle high computational demands. A robust specular reflection scheme was implemented. These efforts enabled generation of breakthrough curves directly from pore-scale simulations for quantitative comparisons with laboratory experimental data.

Computational domains for direct numerical simulations were reconstructed both for column and microfluidics experiments. For the bead-packed column experiments, the digitalized column replica was reconstructed from the images scanned by a microfocus XCT scanner. Customized routines were developed to differentiate the pores and glass beads in the column. In this binary segmentation process, a different threshold value was assigned to each image to match the bulk porosity of the column used in the experiment. Whereas in the microfluidics experiments, we used the center coordinates and radius of beads obtained in the image processing in the experiments.

Direct comparisons on the level of breakthrough curves were performed. We first aimed to obtain agreeable predictions from pore-scale simulations for a non-reactive solute and colloid. Our pore-scale models were further extended to incorporate microscale physio-chemical interactions

including 1) equilibrium partitioning processes in the column experiments, and 2) colloid deposition in the microfluidics experiments.

1.3 The contents of dissertation

This dissertation is organized to provide an introduction to pore-scale simulations of advection-diffusion in porous media with motivations and objectives of this research in Chapter 1, to provide a brief review of continuum-scale transport models in Chapter 2, to provide an overview of lattice Boltzmann method (LBM) and random walk particle tracking (RWPT) in Chapter 3 and Chapter 4, respectively. Comparisons between pore-scale simulations and bead-packed columns and between simulations and microfluidics experiments are presented in Chapter 5 and Chapter 6, respectively. In Chapter 7, anisotropic random walk was introduced and simulated over a simple BCC domain. Lastly, Chapter 8 closes this dissertation with summary and recommendations for future work.

CHAPTER 2
TRADITIONAL APPROACHES TO TANSPORT IN POROUS MEDIA

This chapter briefly reviews the fundamentals of solute and particle transport in porous media including three major processes: advection, diffusion and dispersion. Traditional continuum transport models formulated based on the classical advection-dispersion equation (ADE) are presented. Extended advection-dispersion equations for equilibrium partitioning and kinetic deposition are also presented to facilitate a comparative discussion with pore-scale simulations. Breakthrough curves from analytic solutions of one-dimensional advection dispersion equation (1D-ADE) are illustrated for further discussion.

2.1 An overview of traditional approaches to flow and transport in porous media

In our subsurface system, solute, in the form of dissolved substance in the solvent, exists everywhere. Physical mechanisms of flow and transport of solute in porous media are advection (or convection) and diffusion. Advection refers to transport of solutes by the motion of fluid. The advective flux through a saturated porous media with effective porosity (ϕ_e) is the product of the interstitial velocity or pore velocity (V) of flow and macroscopic concentration of the solute (C) (Eq. 2-1). Diffusion, on the other hand, is the result of thermal motion of solute molecules in solution that drives solutes to move from regions of high concentration to regions of low concentration (Eq. 2-4). On the level of a representative element volume (REV), total flux is the sum of advective and dispersive fluxes (Eq. 2-3), and the many tortuous paths of porous medium within REV slows down the spreading of solutes from high concentration to low concentration. Therefore, the effective diffusion coefficient (D_e) in porous media is usually smaller than the molecular diffusion coefficient in bulk solution (D_o) by a factor of tortuosity (τ) of porous media (Eq. 2-4). When flow is present, spreading of solutes is also attributed to the sub-REV velocity variations relative to the mean velocity due to the many different paths that solutes travel through. The net spreading of solutes on the REV level during flow is called dispersion. Both microscopic advection and diffusion contribute to dispersion and it is not possible to clearly separate their contributions. That said, the effective diffusion coefficient D_e may be phenomenologically subtracted from the apparent dispersion coefficient D_a (Eq. 2-2), leading to the definition of the *mechanical* dispersion coefficient D_m (Bear 1972) (Eq. 2-5). Apparent dispersion coefficient D_a is

an anisotropic property that is usually expressed as a tensor. The longitudinal component of D_a (in the direction of flow) is named the longitudinal dispersion coefficient (D_L) (Bear 1972). Apparent dispersion is also called "hydrodynamics dispersion". As described above, it is the result of collective processes by molecular diffusion and advection.

$$J_{advective} = \phi_e V C \tag{2-1}$$

$$J_{dispersive} = -\phi_e D_a \frac{dC}{ds} \tag{2-2}$$

$$J = J_{advective} + J_{dispersive} \tag{2-3}$$

$$J_{diffusive} = -\phi_e D_0 \tau \frac{dC}{ds} = -\phi_e D_e \frac{dC}{ds} \tag{2-4}$$

$$J_{dispersive} - J_{diffusive} = -\phi_e D_a \frac{dC}{ds} + \phi_e D_e \frac{dC}{ds} = -\phi_e (D_a - D_e) \frac{dC}{ds} = -\phi_e D_m \frac{dC}{ds} \tag{2-5}$$

The advective and dispersive processes in porous media have been extensively studied since they are related to a wide range of practical engineering problems. Phenomenological observations using column scale laboratory experiments played a pivotal role in understanding physical mechanisms of flow and transport of solute in porous media (Lowe and Frenkel 1996). Mass and momentum conservation over a REV of porous media with the effective porosity (ϕ_e) yields the following partial differential form of the classical advection-dispersion equation (Eq. 2-6).

$$\phi_e \frac{\partial C}{\partial t} + \nabla \cdot (\phi_e V C) = \nabla \cdot (\phi_e \boldsymbol{D} \nabla C) \tag{2-6}$$

Eq. 2-6 is the governing differential equation in the most general form of the advective-dispersive transport in a fully saturated porous media without sorption and retardation (Batu 2005). The velocity term V is the interstitial velocity, and the macroscopic solute concentration C is volume averaged concentration, the mass of solute dissolved over a unit volume of solution in an REV.

The dispersion term **D** can be written in a tensorial form for anisotropic dispersive processes (Eq. 2-7) (Bear 1961).

$$[D_{ij}] = \begin{bmatrix} D_{11} & D_{12} & D_{13} \\ D_{21} & D_{22} & D_{23} \\ D_{31} & D_{32} & D_{33} \end{bmatrix}$$

(2-7)

For a homogeneous isotropic media, Eq. 2-6 is reduced to one-dimensional from with the uniform interstitial velocity U in the flow direction or x direction (Eq. 2-8).

$$\frac{\partial C}{\partial t} = D_L \frac{\partial^2 C}{\partial x^2} - U \frac{\partial C}{\partial x}$$

(2-8)

, where D_L is the longitudinal dispersion coefficient.

2.2 Equilibrium and Non-equilibrium sorption models

A sink or source term (G) can be added to the Eq. 2-8 when there a mass transfer between the solid and liquid phases.

$$\frac{\partial C}{\partial t} = D_L \frac{\partial^2 C}{\partial x^2} - U \frac{\partial C}{\partial x} + G$$

(2-9)

The sink or source term (G) is normally expressed in terms of the rate of solute concentration on the solid phase (S) (van Genuchten and Wierenga 1976; Gillham and Cherry 1983; Batu 2005).

$$\frac{\partial C}{\partial t} = D_L \frac{\partial^2 C}{\partial x^2} - U \frac{\partial C}{\partial x} - \frac{\rho_b}{\phi} \frac{\partial S}{\partial t}$$

(2-10)

ρ_b is the bulk density of porous media and S is the mass of the solute adsorbed onto the solid phase. Now the sink-source term for sorption-desorption is further expanded by chain rule (Eq. 2-11) on the premises that 1) the sorption-desorption processes occurs almost instantaneously to achieve thermodynamic equilibrium, and 2) the process is isothermal controlled only by the mass of the solute on the solid phase (Batu 2005).

$$\frac{\partial C}{\partial t} = D_L \frac{\partial^2 C}{\partial x^2} - U \frac{\partial C}{\partial x} - \frac{\rho_b}{\phi} \frac{\partial S}{\partial C} \frac{\partial C}{\partial t}$$

(2-11)

Rearranging Eq. 2-11 yields,

$$\left(1 + \frac{\rho_b}{\phi}\frac{\partial S}{\partial C}\right)\frac{\partial C}{\partial t} = D_L \frac{\partial^2 C}{\partial x^2} - U\frac{\partial C}{\partial x} \qquad (2\text{-}12)$$

Assuming that the concentration of the solute in solution (C) is proportional to the concentration of the solute on the solid phase (S), i.e., a linear sorption isotherm, Eq. 2-12 is rewritten in terms of the partitioning coefficient or distribution coefficient (K_d).

$$\left(1 + \frac{\rho_b}{\phi}K_d\right)\frac{\partial C}{\partial t} = D_L \frac{\partial^2 C}{\partial x^2} - U\frac{\partial C}{\partial x} \qquad (2\text{-}13)$$

By defining the retardation factor (R_d),

$$R_d = 1 + \frac{\rho_b}{\phi}K_d \qquad (2\text{-}14)$$

the one-dimensional advection-dispersion equation (1D-ADE) for a homogeneous porous medium with uniform flow under retardation is given,

$$R_d \frac{\partial C}{\partial t} = D_L \frac{\partial^2 C}{\partial x^2} - U\frac{\partial C}{\partial x} \qquad (2\text{-}15)$$

A mass transfer between the liquid and solid phases in porous media may occur when equilibrium conditions are not met. For example, the mass transfer under a very high flow rate may not satisfy the thermodynamic equilibrium condition, then it becomes a kinetic process (Fetter 2008). The kinetic process can be modeled as reversible or irreversible of any order (Cameron and Klute 1977). If the process is reversible, i.e., the solutes once sorbed on the solid phase are not desorbed, it is modeled as the first order irreversible kinetic reaction (Eq. 2-16 and Eq. 2-17) (Kretzschmar et al. 1997).

$$\frac{\partial C}{\partial t} = D_L \frac{\partial^2 C}{\partial x^2} - U\frac{\partial C}{\partial x} - \frac{\rho_b}{\phi_e}\frac{\partial S}{\partial t} \qquad (2\text{-}16)$$

$$\frac{\rho_b}{\phi_e}\frac{\partial S}{\partial t} = kC \qquad (2\text{-}17)$$

where k is the first order kinetic deposition rate constant.

2.3 Analytic solution of 1D-ADE

The dispersion tensor $\boldsymbol{D}$ (Eq. 2-7) represents the ensemble average of microscopic transport processes by molecular diffusion and advection in isotropic and anisotropic natural porous media (Icardi et al. 2014). Dispersion coefficients are still among the most controversial properties of porous media. A lot of studies have been made to understand fundamental mechanisms of dispersion in flow and transport and determination of the hydrodynamic dispersion coefficients. Those research efforts include laboratory or field experiments in combination with analytic or numerical transport models. Traditionally, laboratory column flow-through experiments were widely used to determine the longitudinal dispersion coefficient by analyzing the effluent concentration profile scaled by inlet solute concentration (i.e., breakthrough curve or BTC) with one-dimensional advection-dispersion equation (1D-ADE). The longitudinal dispersion coefficient D_L is obtained by fitting the measured concentration data to analytic or numerical solutions with given boundary conditions. For example, the analytic solution of Eq. 2-8 with unit step input is given in Eq. 2-18 (Ogata and Banks 1961),

$$C = \frac{1}{2}C_0\left[erfc\left(\frac{x-Ut}{2\sqrt{D_L t}}\right) + \exp\left(\frac{Ux}{D_L}\right) erfc\left(\frac{x+Ut}{2\sqrt{D_L t}}\right)\right] \tag{2-18}$$

, where C is effluent concentration, C_0 is inlet concentration, t is time, x is the location in the column in the flow direction, and U is the uniform velocity (interstitial velocity) in the flow direction. For column experiments, Eq. 2-18 is rearranged to get the effluent concentration (C) at the column exit ($x = L$) as a function of pore volume (t_R) (Eq. 2-19).

$$C = \frac{1}{2}C_0\left[erfc\left(\frac{Pe}{4t_R}\right)^{1/2}(1-t_R) + \exp(Pe)\,erfc\left(\left(\frac{Pe}{4t_R}\right)^{1/2}(1+t_R)\right)\right]$$
$$t_R = Ut/L$$
$$Pe = UL/D_L \tag{2-19}$$

The characteristic length in the Péclet number is a column length (L) and D_L is a longitudinal dispersion coefficient. Figure 2-1 shows breakthrough curves with three different Péclet numbers obtained using Eq. 2-19.
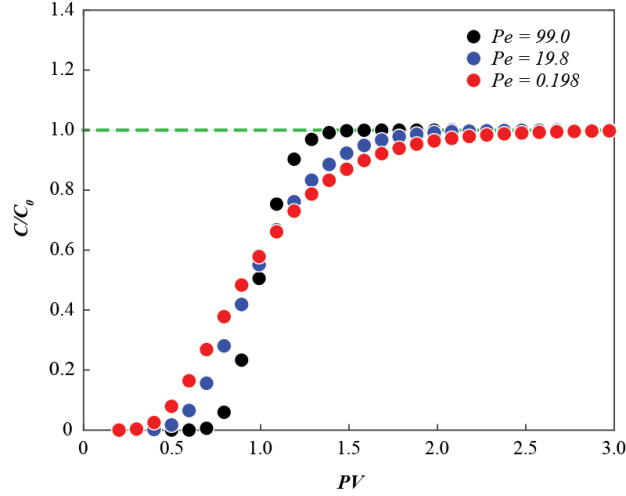
Figure 2-1: Breakthrough curves from the analytic solution of 1D-ADE (Eq. 2-19) under fully saturated porous media with unit step input concentration for a passive solute: longitudinal dispersion coefficients used are 99, 19.8, and 0.198.

The analytic solution under retardation is easily obtained,

$$C = \frac{1}{2}C_0\left[erfc\left(\frac{R_d x - Ut}{2\sqrt{D_L R_d t}}\right) + \exp\left(\frac{Ux}{D_L}\right)erfc\left(\frac{R_d x + Ut}{2\sqrt{D_L R_d t}}\right)\right] \tag{2-20}$$

Figure 2-2 illustrates a comparison between a breakthrough curve of a non-sorbing solute and that of a sorbing solute with the retardation factor of 5. The equilibrium partitioning process represented by retardation factor (R_d) in Eq. 2-20 scale down the advection and dispersion, resulting in retarded breakthrough curves.
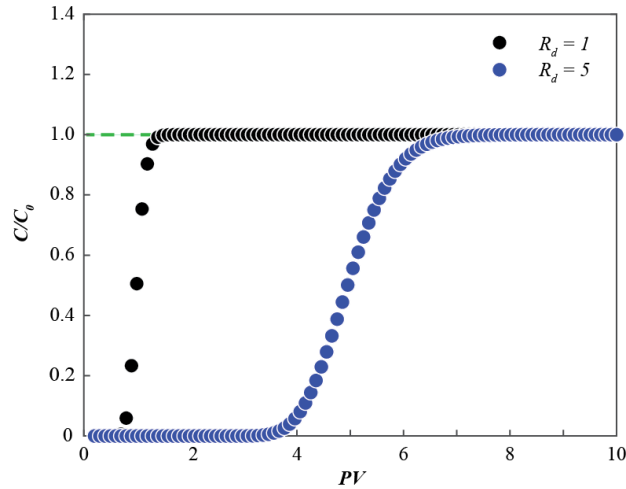
Figure 2-2: A comparison between a breakthrough curve of a passive solute and that of a sorbing solute: retardation factor is 5 at $Pe = 99$.

11

Traditionally, longitudinal dispersion coefficients of conservative tracers are obtained by fitting experimental data (column) with the solution of the 1D-ADE (Eq. 2-18 or Eq. 2-19). For adsorbing solutes, batch experiments are first conducted to evaluate partitioning coefficients. With the longitudinal dispersion coefficient and equilibrium partitioning coefficient obtained as such, the effluent concentration profile is then predicted using the analytic solution under retardation (Eq. 2-20).

To summarize this chapter, illustrative breakthrough curves predicted by classical 1D-ADEs are presented. They are used to show how the Péclet number and equilibrium partitioning and irreversible kinetic adsorption processes affect effluent concentration profiles (Molnar et al. 2015) (Figure 2-3). In this study, pore-scale simulations generated the breakthrough curves of a conservative solute (I^-), a radioactive solute that exhibits equilibrium partitioning (Cs^+), and a colloid with irreversible deposition. While direct comparison between simulation data and experiments is the main objective, analytical solutions presented in this chapter will also be used to check the quality of simulations.
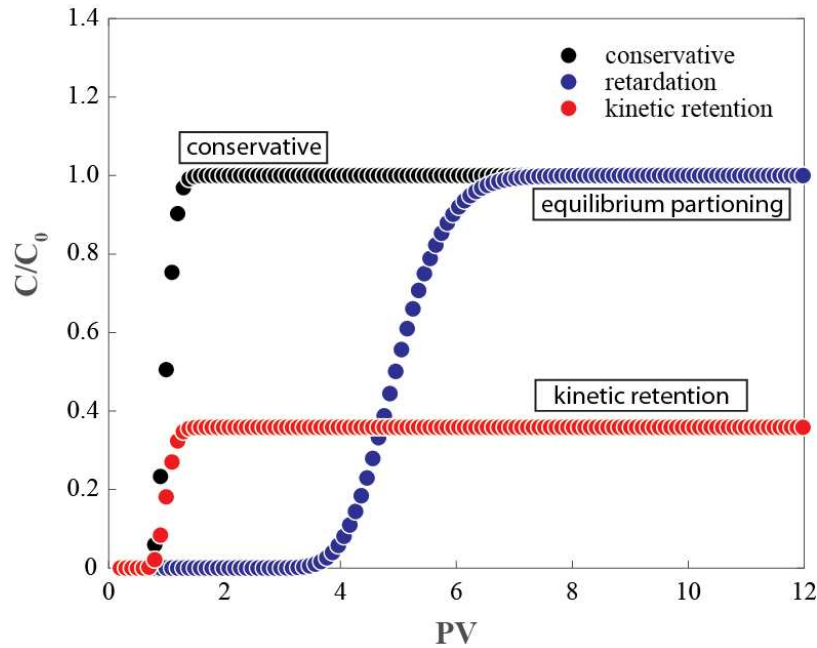
Figure 2-3: Illustrative breakthrough curves of particle transport under equilibrium partitioning (blue: Eq. 2-15) and kinetic adsorption (red: Eq. 2-16 and Eq. 2-17) processes relative to a conservative tracer (black: Eq. 2-8) (reproduced from Molnar et al. 2015).

CHAPTER 3

LATTICE BOLTZMANN METHOD

This chapter provides an introduction to the lattice Boltzmann method (LBM). A single phase parallelized LB code was validated using benchmark problems including Poiseuille flow (steady state) and Taylor-Green vortex (transient).

3.1 Overview of the lattice-Boltzmann method (LBM)

The lattice Boltzmann method does not rely on the continuum mechanics of fluids that traditional computational fluid dynamics (CFD) methods such as finite difference and finite element are based on. Instead, it is based on a simplified kinetic theory established to describe movements and collisions of clusters of molecules, dubbed as "particles", on a space-filling lattice. The particle distribution function describes the probability of finding a particle at a given location having a certain velocity (Succi 2001). Instead of using macro-scale physical quantities such as density, velocity and pressure, the kinetic theory traces the evolution of the particle distribution function in the space-velocity phase space. At equilibrium, the particle distribution function follows the Maxwell-Boltzmann distribution. When system is at non-equilibrium, i.e., with gradients in macroscopic velocity, the second-order moment of particle distribution (macroscopic stress) is adjusted to reflect the outcome of inter-particle collision, which is relaxation of local non-equilibrium. Finally, macroscopic properties of interest such as density and velocity are recovered from the zeroth- and first-order moments of the particle distribution function. It has been mathematically proven that the lattice-Boltzmann method recovers the solution of Navier-Stokes equation (Chen et al. 1992).

In the lattice Boltzmann method, the evolution of the particle distribution function follows a discretized version of the Boltzmann transport equation known as the lattice Boltzmann equation (LBE) (Eq. 3-1). In the lattice-Boltzmann equation, the discrete particle distribution function f_i is the primary variable. According to the LBE, each discretized particle distribution function moves in space with a lattice velocity that allows a particle to reach a neighboring lattice in the direction of the lattice velocity in a single time step. An example of a set of lattice velocity for two-dimensional flows with nine discrete velocities (D2Q9) is given in Eq. 3-2. After this movement or *propagation*, particles that arrive at a lattice node *collide* with each other, which is a

process to relax the non-equilibrium particle distribution, the deviation from the local equilibrium distribution f_i^{eq} (Eq. 3-3). The relaxation of non-equilibrium distributions occurs at a constant rate, the inverse of which is known as the relaxation time τ, according to the BGK (Bhatnagar-Gross-Krook) collision scheme given in Eq. 3-4 (Bhatnagar et al. 1954). The macroscopic properties such as density and velocity are recovered as the zeroth- and first-order moments of the discrete particle distribution function, respectively (Eq. 3-5 and Eq. 3-6).

$$f_i\left(\underline{x}+c_i\Delta t, t+\Delta t\right) - f_i(\underline{x},t) = \Omega_i \tag{3-1}$$

$$c_i = \begin{bmatrix} 0 & 1 & -1 & 0 & 0 & 1 & 1 & -1 & -1 \\ 0 & 0 & 0 & 1 & -1 & 1 & -1 & 1 & -1 \end{bmatrix} \tag{3-2}$$

$$f_i^{eq}(\boldsymbol{x},t) = w_i\rho\left[1 + \frac{\boldsymbol{c}_i \cdot \boldsymbol{u}}{c_s^2} + \frac{\boldsymbol{uu}:(\boldsymbol{c}_i\boldsymbol{c}_i - c_s^2\boldsymbol{I})}{2c_s^4}\right] \tag{3-3}$$

$$\Omega_i = -\frac{f_i(\underline{x},t) - f_i^{eq}(\underline{x},t)}{\tau}\Delta t \tag{3-4}$$

$$\rho(\underline{x},t) = \sum_i f_i(\underline{x},t) \tag{3-5}$$

$$\rho\boldsymbol{u}(\boldsymbol{x},t) = \sum_i c_i f_i(\boldsymbol{x},t) \tag{3-6}$$

The LBE (Eq. 3-1) with collision operator (Eq. 3-4) may be rearranged in a form to show that the overall procedure of solving the LBE can be viewed in two steps: collision (Eq. 3-7) and streaming (Eq. 3-8).

$$f^{coll}_i(\underline{x},t) = f_i(\underline{x},t)\left(1 - \frac{\Delta t}{\tau}\right) + f_i^{eq}(\underline{x},t)\frac{\Delta t}{\tau} \tag{3-7}$$

$$f_i\left(\underline{x}+c_i\Delta t, t+\Delta t\right) = f^{coll}_i(\underline{x},t) \tag{3-8}$$

The collision operator Ω_i can be formulated in many ways. In addition to the popular the Bhatnagar-Gross-Krook (BGK) scheme (Bhatnagar et al. 1954) presented in Eq. 3-4, another well used scheme is the multiple relaxation time (MRT) collision operator (d'Humieres et al. 2002). Owing to its extreme simplicity, the BGK scheme has been widely used for various hydrodynamics problems in spite of some limitations including stability issues in fluid flows with high Reynolds numbers (Aslan et al. 2014). The multiple relaxation time (MRT) lattice Boltzmann method or the generalized lattice Boltzmann method has advantages over BGK in that it is less susceptible to numerical instability in high Reynolds number hydrodynamics (d'Humieres 1994). It is well known that the stability and accuracy of BGK LB solution depend on the relaxation time. Using Poiseullie flows, it was shown that the numerical accuracy decreases with increasing relaxation time (Ginzbourg and Adler 1994). For high-Reynolds-number hydrodynamics problems, BGK LB exhibits numerical instability. To improve numerical accuracy and stability, multi-relaxation time (MRT) collision process was proposed by d'Humieres (1994). With higher degree of freedoms in relaxation rates, MRT generally yields improved numerical solutions than BGK.

The key difference of MRT from BGK is that the collision step is implemented in the moment space to allow different moments of lattice particle distribution to relax toward their respective equilibriums with different relaxation rates (Krüger et al. 2017). For D2Q9 MRT LB, the nine moments are defined in a vector $\boldsymbol{m}$ (Eq. 3-9).

$$\boldsymbol{m} = (\rho, e, \varepsilon, j_x, q_x, j_y, q_y, p_{xx}, p_{xy})^T \tag{3-9}$$

, where ρ is density as the zeroth order moment, e is kinetic energy as a second order moment, ε is energy squared as a fourth order moment, j_x and j_y are momenta in x and y directions as first order moments, q_x and q_y are heat fluxes in x and y directions as third-order moments, p_{xx} and p_{xy} are normal and shear stresses, respectively, as second-order moments. The transformation from particle distribution functions to moments can be written in Eq. 3-10.

$$\boldsymbol{m} = \boldsymbol{Mf} \tag{3-10}$$

BGK LB, recast into Eq. 3-11, where ω is the relaxation rate, the inverse of relaxation time τ, shows that it is a special case of MRT LB. Using the transformation (Eq. 3-10), the MRT LB

15

update (Eq. 3-12) includes a transformation matrix M (Eq. 3-13) and a relaxation matrix S (Eq. 3-14).

$$f\left(x+c\Delta t, t+\Delta t\right) - f(x,t) = -\omega\left[f(x,t) - f^{eq}(x,t)\right]\Delta t \tag{3-11}$$

$$f\left(x+c\Delta t, t+\Delta t\right) - f(x,t) = -M^{-1}S\left[m - m^{eq}\right]\Delta t \tag{3-12}$$

$$M = \begin{bmatrix} 1 & 1 & 1 & 1 & 1 & 1 & 1 & 1 & 1 \\ -4 & -1 & -1 & -1 & -1 & 2 & 2 & 2 & 2 \\ 4 & -2 & -2 & -2 & -2 & 1 & 1 & 1 & 1 \\ 0 & 1 & -1 & 0 & 0 & 1 & 1 & -1 & -1 \\ 0 & 1 & -1 & 0 & 0 & 1 & 1 & -1 & -1 \\ 0 & -2 & 2 & 0 & 0 & 1 & 1 & -1 & -1 \\ 0 & 0 & 0 & 1 & -1 & 1 & -1 & 1 & -1 \\ 0 & 1 & 1 & -1 & -1 & 0 & 0 & 0 & 0 \\ 0 & 0 & 0 & 0 & 0 & 1 & -1 & -1 & 1 \end{bmatrix} \tag{3-13}$$

$$S = diag(\omega_0, \omega_1, \omega_2, \cdots, \omega_8) = diag(0, s_8, s_3, 0, s_5, 0, s_5, s_8, s_8)$$
$$s_8 = \frac{1}{\tau}, s_5 = \frac{8(2-s_8)}{8-s_8} \tag{3-14}$$

In the relaxation matrix S (Eq. 3-14), the elements corresponding to conserved quantities (e.g., density and momentum) are set to zero since they are not affected by collision $\left(\omega_0 = \omega_3 = \omega_5 = 0\right)$. Moments of the same order have same relaxation parameters $\left(\omega_4 = \omega_6 \text{ and } \omega_7 = \omega_8\right)$ (Eq. 3-14). Other elements can be arbitrarily chosen. In our D2Q9 MRT LB, the relaxation matrix is defined as in Eq. 3-14. More detailed derivation of the transformation and relaxation matrices can be found in d'Humieres et al. (2002). Lastly, the relation between the shear viscosity of the fluid and the relaxation time is Eq. 3-15 (d'Humieres 1994).

$$\mu = \rho_0 c_s^2\left(\tau - \frac{1}{2}\right) = \frac{\rho_0}{3}\left(\tau - \frac{1}{2}\right) \tag{3-15}$$

3.2 Forcing scheme in the lattice-Boltzmann method

Subsurface flows through complex pore geometries are mostly driven by pressure gradients. When geometries of porous media are repeating or periodic, the pressure gradient can be replaced by an equivalent force density (Kim and Pitsch 2007). Flow of incompressible fluids in porous media driven by a constant pressure gradient therefore is often simulated using a constant body force in combination with periodic boundary conditions. This approach of replacing a pressure gradient with an equivalent body force is very attractive because LB suffers less compressibility errors (Krüger et al. 2017) when the flow is driven by a body force. The lattice Boltzmann equation (LBE) with a forcing term is as follows (Eq. 3-16):

$$f_i\left(x+c\Delta t, t+\Delta t\right)-f_i(x,t)=-\Omega_i\left[f_i(x,t)-f_i^{eq}(x,t)\right]+\Delta t F_i' \tag{3-16}$$

There has been a large number of discussions on the implementation of forcing schemes in the lattice-Boltzmann method. Different forcing schemes were proposed by researchers including Ladd and Verberg (2001), Guo et al. (2002), Shan and Chen (1993), He et al. (1998) and Kupershtokh (2004). When a body force term is introduced to the LBE, the momentum term must be redefined to accommodate the forcing term regardless of which forcing scheme is used (Krüger et al. 2017). As Eq. 3-17 shows, the momentum is shifted by half the forcing term. This treatment can be interpreted as the average momentum between two time steps when a force term is present (Ladd and Verberg 2001).

$$\rho\boldsymbol{u}=\boldsymbol{j}=\sum_i c_i f_i + \frac{\boldsymbol{F}}{2}\Delta t \tag{3-17}$$

It should be noted that there is no significant difference between the momentum defined in Eq. 3-6 and the shifted momentum based on Eq. 3-17 for Poiseullie flows. However, the more solid nodes are present in simulation domains, the more evident the difference becomes in the momentum / velocity field. In our study, the shifted momentum defined by Eq. 3-17 was used for flows through porous media driven by a constant body force.

3.3 Validations of lattice-Boltzmann simulations

In this section, time-invariant Poiseuille flow and time-dependent two-dimensional Taylor-Green vortex are used to verify the accuracy of our LB codes. Simulations of Poiseuille flows employed a three-dimensional and nineteen-velocity model (D3Q19) (Xiao and Yin 2016).

Simulations of Taylor-Green vortex used a two-dimensional and nine-velocity (D2Q9) lattice Boltzmann model (Newman and Yin 2013). Both D2Q9 and D3Q19 models can use either BGK or MRT collision operators

First, Poiseuille flow between two stationary walls driven by a constant pressure drop was simulated using the parallelized D3Q19 LB code. The computational domain size is 22×1×111 in x, y and z directions, respectively. A constant body force was applied in the mean flow direction and the simulation was run until flow achieved steady state. Periodic boundaries were used along y and z directions and solid nodes were placed at x = 0 and x = 22. Flow direction is z and the height of the flow channel is 20. A constant body force of 10^{-5} was applied along the z-direction.

Figure 3-1 shows the distribution of the z-velocity and Figure 3-2 shows the comparison between the numerical solution and the analytical solution, which is very good. The permeability of the channel calculated using the velocity from the numerical simulation was compared to the analytical solution. The relative error in the permeability is 0.126%.
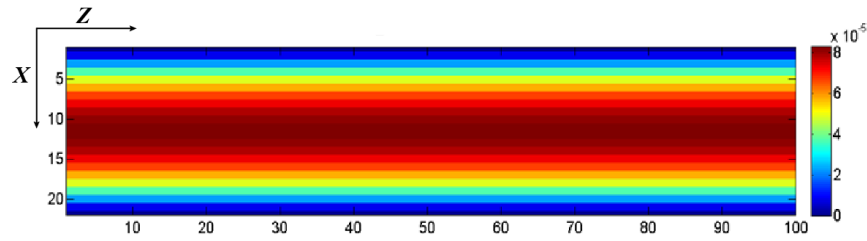
Figure 3-1: Distribution of z-velocity (flow direction) from LB simulation.
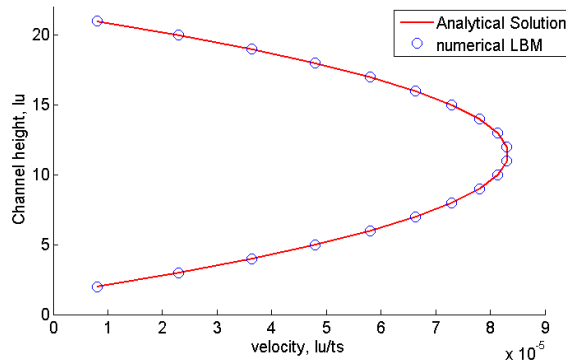
Figure 3-2: Comparison between the analytical and the numerical solutions for the Poiseuille flow.

Second, the two-dimensional Taylor Green vortex (Taylor and Green 1937) was used to test the D2Q9 model for a case of transient flows. The simulation domain, which is a periodic box of dimension $[0 \ 2\pi]$ in both x and y directions, was discretized using 100 lattices in each direction. An initial velocity field was applied using the analytical solution of the Taylor Green vortex (Eq. 3-18). In the absence of pressure and body force, the initial velocity field decays due to viscous dissipation. Figure 3-3 and Figure 3-4 show that the numerical solution is in good agreement with the analytical solution of the Taylor Green vortex, both in the pressure and the velocity field.

$$U(x,y,t) = -U_o \cos(kx)\sin(ky)e^{-2k^2vt},$$
$$V(x,y,t) = +U_o \sin(kx)\cos(ky)e^{-2k^2vt},$$
$$P(x,y,t) = P_o - \frac{\rho_o}{4}U_o^2\left\{\cos(2kx)+\cos(2ky)\right\}e^{-4k^2vt}$$

(3-18)

(a)   (b)
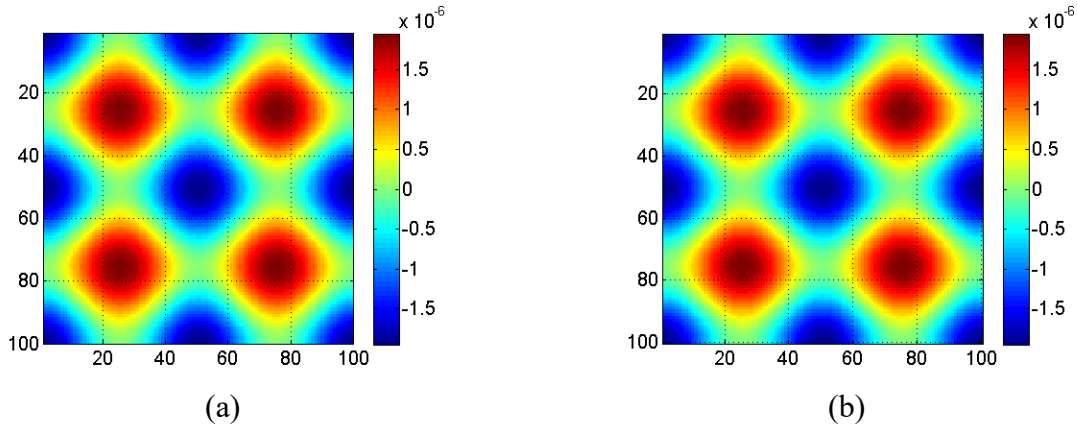
Figure 3-3: Pressure distribution based on the analytical solution (a) and that from the numerical simulation (b) at the same time t = 500.

(a)   (b)
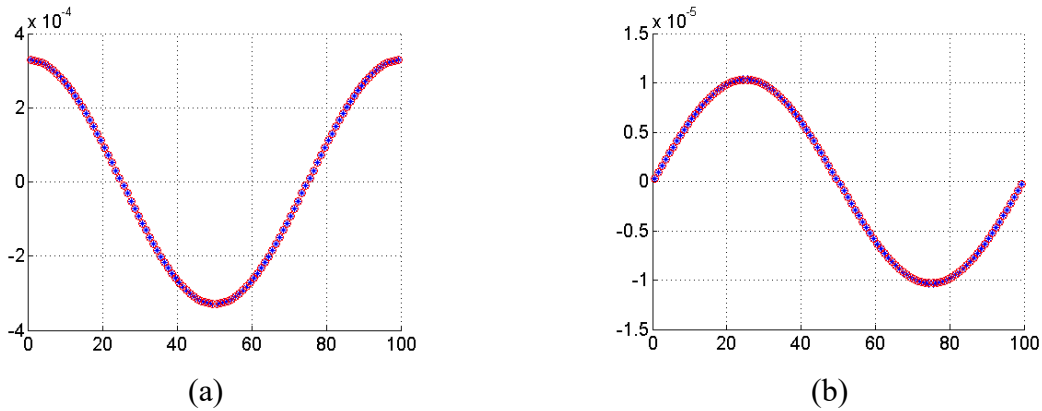
Figure 3-4: Comparison between the analytical and the numerical solutions: x-velocity (a) and y-velocity (b) along y = 25 at the time step of t = 500.

CHAPTER 4

RANDOM WALK PARTICLE TRACKING

Since the pioneering work of Albert Einstein (1905) revealed the physics of Brownian motion and the associated diffusive processes, random walk methods have been widely used to model diffusion in many branches of science and engineering including biology, economics, physics, mechanical, chemical, environmental engineering, material and medical sciences. The random walk particle tracking method employed in this study models biased random walk of a large population of particles on a high performance parallel computing platform to simulate advection-diffusion in the pore space.

4.1 Overview of random walk particle tracking (RWPT)

The primary motivation of random walk particle tracking method in hydrodynamics problems is that grid based Eulerian numerical approaches to advection-diffusion problems suffer numerical dispersion due to discretization in time and space (Park et al. 2008). Random walk methods have been considered as a good alternative to the Eulerian methods such as finite difference or finite element because they track particles explicitly in a Lagrangian framework, making it far less susceptible to numerical dispersion and instability. Although issues of numerical dispersion and instability in grid-based methods can be avoided or alleviated to a certain degree by increasing spatial and temporal discretization, these treatments inevitably lead to more time and resources spent in computation (Liu et al. 2004). Particularly for high-Péclet number problems in which advection prevails over diffusion, the spatial discretization required to fall within the stability criteria of the standard transport models may not be practically attainable. The Péclet number is defined as $Pe = ud / D$, where u is superficial velocity, d is characteristic length of the porous medium (the bead diameter unless specifically stated otherwise), D is the molecular diffusion coefficient. This leads to a great deal of difficulty in solving advection dominated problems with high spatial and temporal gradients in the velocity field (Park et al. 2008). Advection dominated transport problems with high spatial gradients in the velocity are often observed in fluid flows in porous media. Hence, using random walk particle tracking to simulate advection-diffusion in porous media is a good choice. In addition, RWPT is computationally more

efficient both in serial and parallel implementations since it solves a simple algebraic equation instead of a system of linear equations.

The classical advection-dispersion equation (ADE) (Eq. 2-6) has long been used to describe transport of solutes in fluids flowing through porous media. It should be noted that the solution for velocity V in Eq. 2-6 is the Darcy-scale interstitial velocity governed by Darcy's law. Traditional approaches to modeling solute transport solve this partial differential equation analytically or numerically. The coefficients in the advection-dispersion equation reflect averaged properties of a complex transport process (Icardi et al. 2014). On the scale of the advection-dispersion equation, the effects of small scale heterogeneities and molecular diffusion through porous media are scaled up (Rhodes et al. 2009). In traditional approaches, the dispersion tensor in the ADE is evaluated by comparing breakthrough curves of column experiments with analytic or numerical solutions of the advection-dispersion equation.

In this study, RWPT solves the advection-diffusion equation at the pore scale (Eq. 4-1).

$$\frac{\partial c}{\partial t} + \boldsymbol{v} \cdot \nabla c = \nabla \cdot \left(\boldsymbol{D}_0 \nabla c \right) \tag{4-1}$$

The solution for $\boldsymbol{v}$, the pore-scale velocity, comes from lattice Boltzmann simulations. $\boldsymbol{D_o}$ is molecular diffusion coefficient (Eq. 4-2).

$$\boldsymbol{D}_0 = \begin{bmatrix} D_0 & 0 & 0 \\ 0 & D_0 & 0 \\ 0 & 0 & D_0 \end{bmatrix} \tag{4-2}$$

A solute or a colloid whose size is much smaller than pore throats is modeled as a volume-less point tracer in RWPT. It is also assumed that the motion of a tracer has no influence on the fluid flow. The movement of a tracer in a biased random walk, where the bias comes from deterministic advection, is computed using Eq. 4-3.

$$d\boldsymbol{x}(t) = \boldsymbol{v}(\boldsymbol{x}(t))dt + \boldsymbol{B} \cdot d\boldsymbol{W}(t) \tag{4-3}$$

x is the displacement vector, **v** is the velocity vector, **B** represents the magnitude of diffusive movement, and **W** is a Gaussian random process of the Brownian motion (Tompson and Gelhar 1990).

The above stochastic differential equation was marched explicitly in time using an Euler approximation (Eq. 4-4) (Maier et al. 2000). Those authors established that the time step (Δt) for tracer movement should be limited such that the maximum movement of a tracer in one time step is less than half the grid size (h) of the fluid flow simulation from which the local maximum velocity (u_{max}) is obtained (Maier et al. 2000). This feature was implemented in our RWPT code to control the size of time step (Eq. 4-5).

$$\boldsymbol{x}(t+\Delta t) = \boldsymbol{x}(t) + \boldsymbol{v}(\boldsymbol{x}(t))\Delta t + \sqrt{2D_0\Delta t}\,\boldsymbol{\xi} \qquad (4\text{-}4)$$

$$\left\| u_{max}\Delta t + \sqrt{6D_0\Delta t} \right\| \leq h/2 \qquad (4\text{-}5)$$

Computing the dispersion tensor on the REV level from RWPT is straightforward following the relation between the dispersion tensor and the covariance tensor of squared displacement Eq. 4-6 and Eq. 4-7. If averaged transport cannot be well described by a single dispersion tensor, it will be reflected through the time dependence of the covariance tensor.

$$\boldsymbol{D}(t) = \frac{1}{2}\frac{d\boldsymbol{\sigma}^2}{dt}(t) \qquad (4\text{-}6)$$

$$\sigma_{ij}^2 = \left\langle \left[x_i(t) - \langle x_i(t)\rangle \right]\left[x_j(t) - \langle x_j(t)\rangle \right] \right\rangle \qquad (4\text{-}7)$$

4.2 Boundary conditions of random walk particle tracking

Tracers in RWPT are allowed to move only in the pore space (fluid) and they are not allowed to enter the solid phase. Therefore, if a tracer moves into the solid phase as a result of advection and diffusion, such movement needs to be properly handled to ensure that the physics of solute-solid interaction is respected. In this section, we present methods to recover the no-flux boundary condition imposed on the interface between the solid and the fluid for solutes that do not interact with solids.

Different methods of implementing no-flux boundary condition in RWPT have been proposed and they are summarized as follows (Khirevich 2011): 1) rejection, 2) multiple rejections, 3) time step division, 4) interruption, 5) specular reflection. In the rejection scheme, a tracer's

movement into the solid phase is rejected and the tracer stays at its previous position. In the method of multiple rejections, if a tracer enters the solid phase, such a movement is negated and the tracer is moved only by diffusion until it finds its position in fluid. In the method of time step division, if a tracer hits the solid phase, the tracer is returned to its original position, and the time step is divided into smaller fractions to move the tracer in multiple time steps without hitting the solid, until the sum of divided time steps reaches the full time step. In the method of interruption, the time step of a tracer crossing the interface is divided into two: before collision and after collision. This tracer is placed at the contact point on the interface after the first part of the time step elapses. The velocity component normal to the surface is then reversed to calculate the displacement during the remaining time step. In the specular reflection scheme, if a tracer enters a solid node, the "trajectory" of the tracer is secularly reflected on the interface that the tracer first hits. When multiple interfaces exist, reflection may be repeated until the reflected tracer falls into a fluid node.

Szymczak and Ladd (2003) investigated different methods to achieve no-flux boundary in random walk particle tracking. They showed that the specular reflection method satisfies mass conservation. Khirevich (2011) also suggested that the specular reflection scheme, though computationally heavy, is the most accurate. Our RWPT code uses the specular reflection method to simulate the no-flux boundary condition, as illustrated in Figure 4-1, which specifically shows a scenario where two reflections are needed to return a tracer into the fluid phase. A tracer in the fluid phase is first advected by the local velocity and diffused in random motion. The position after advection and diffusion is in the solid phase, which lead to the first specular reflection on the interface between the solid and liquid phase. The new position after the first specular reflection is in the solid phase. This leads to the second specular reflection. Finally, the position falls into the liquid phase after two consecutive specular reflections.

Robust reflection algorithm is a crucial element in large-scale particle tracking simulations due to a very large number of grid blocks and tracers needed to suppress statistical uncertainties in obtained macroscopic transport properties. The specular reflection scheme implemented in our parallel RWPT code is very robust compared with the previous implementation. For instance, not a single error was found in a large-scale test conducted in a computational domain with 49,467,652 nodes (solid and fluid nodes) using 10,117,521 tracers that was run for 10^9 time steps using 256 processors.
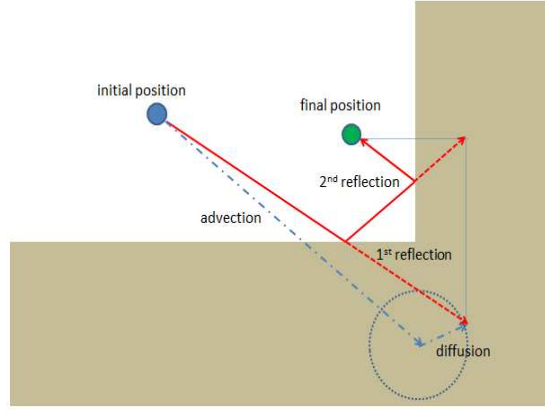
Figure 4-1: Specular reflection method to achieve no flux boundary at the interface of the solid node and fluid node.

4.3 Generating breakthrough curves (BTCs) from random walk particle tracking

Tracer concentration at the "outlet" of the computational domain, or the effluent concentration, is obtained by counting the number of tracers crossing the designated exiting boundary per unit volume of fluid that passes the same boundary during a pre-specified sampling time. This sampling volume and its ratio to the net pore volume are proportional to the average advection velocity from the lattice-Boltzmann simulation. The effluent concentration, scaled by the inlet concentration and presented as a function of pore volume, which equals the sum of all sampling volumes collected and normalized by the net pore volume, generates a breakthrough curve that is directly comparable to those from column experiments.

Implementation of the above method in our RWPT code, however, is complicated as our RWPT code adopts a periodic boundary condition to maintain load balance for parallel computing. At the beginning of a simulation, tracers are distributed uniformly in the entire computational domain. Tracers that have passed through the computational domain are moved to the other side. Assume that mean flow is in the z-direction and tracers are located at r_i $(i = 1, 2, \cdots, N), 0 < r_{zi} < L$. For any tracer that moved past L the following rule was applied (Eq. 4-8):

$$r_{zi}' = r_{zi} - L, \quad r_{zi} > L. \tag{4-8}$$

This treatment ensures that each process in the parallel program, which handles calculations within a subdomain of the porous medium, has similar number of tracers. Clearly, by this initialization strategy and the periodic boundary condition, breakthrough curves for tracers that do not have any

interactions with the solid will simply be unity at any time. To generate breakthrough curves that are directly comparable with experiments, we let these tracers carry pseudo-positions r_i^*. Initially, pseudo-positions $r_i^* = r_i - [0, 0, L]$. According to the pseudo-positions, all initialized tracers are in the periodic image of the computational domain along the z-direction (Figure 4-2a). Pseudo-positons r_i^* can therefore be considered as the locations of tracers that are about to enter the computational domain. When r_i is updated, r_i^* is also updated by the same amount. When $r_i^* > L$, a breakthrough event is recorded. This tracer r_i^* is then updated by the periodic rule (Eq. 4-8) as it "flows" out of the domain $0 < r_{zi} < L$. Based on the periodic rule, as a tracer leaves the domain at $z = L$, it is returned to the side $z = 0$ so that the total number of tracers in the domain remains as a constant. Figure 4-2 illustrates how the pseudo-locations of tracers evolve from initialization to the point when all the tracers have been counted for breakthrough curves.

(a)   (b)

(c)   (d)
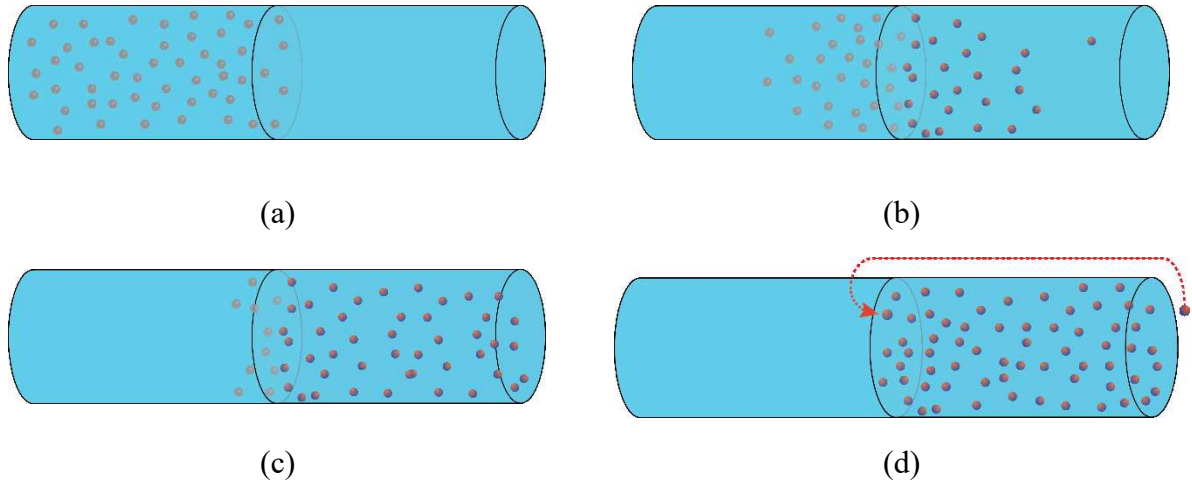
Figure 4-2: Evolution in pseudo-positions of tracers over time (a) Initial pseudo-location of tracers, (b) a portion of tracers entering the porous medium, (c) most tracers in the porous medium, (d) all tracers that have left the domain returned using the periodic boundary condition.

A two-dimensional RWPT code was used to see if the method presented above for domains with periodic boundaries for tracers generates breakthrough curves equivalent to that from the constant–inlet-concentration boundary condition. In simulations with the constant-inlet boundary-condition, tracers are initialized at a constant frequency proportional to the local prescribed flux at the inlet side of the flow channel. These tracers are carried to the outlet by fluid flow. When they

leave the channel, they are counted into the breakthrough curve and eliminated from the total tracer count, unlike the periodic boundary condition. This comparison was made using a plug flow with uniform velocity. The breakthrough curve generated by the method of pseudo-positions with the periodic boundary condition and that from the constant-inlet-boundary condition are practically identical (Figure 4-3), proving that breakthrough curves can indeed be generated from RWPT simulations with periodic boundaries.
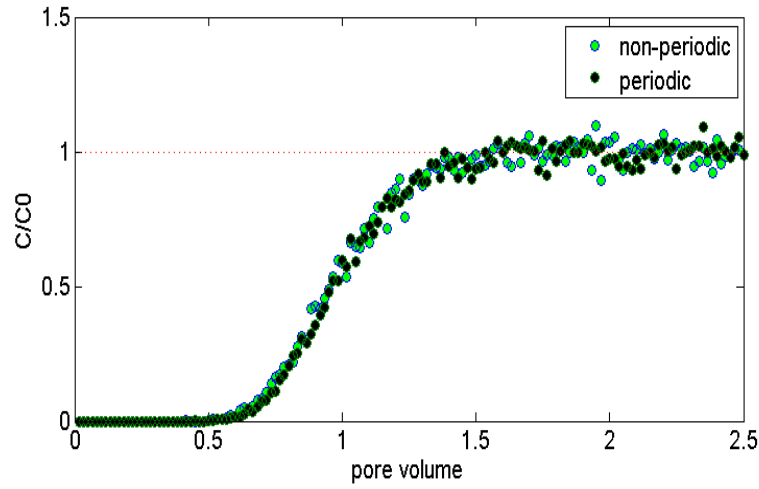
Figure 4-3: Comparison between BTC form constant inlet boundary condition (green) and periodic boundary condition (black) and BTC.

CHAPTER 5

PORE-SCALE SIMULATION OF A BEAD PACKED COLUMN EXPERIMENT

This chapter presents pore-scale simulations of transport of non-adsorbing and adsorbing solutes in bead-packed columns. Rod et al. (2018) conducted a set of column experiments to investigate the effect of chemical and physical heterogeneities on colloid-facilitated radionuclide transport. We simulated transport of a conservative and adsorbing solutes (iodide and cesium) through a column packed with homogeneous beads. CT-scanned images of columns that were packed with glass beads were processed to digitally reconstruct the computational domains for LB and RWPT simulations. The velocity fields resolved by LB simulations were passed to RWPT to generate simulated breakthrough curves and these curves are comparable to those from the experiments. For adsorbing solutes, the equilibrium partition between solvent and solid surface was incorporated into RWPT by a probabilistic approach to reproduce the retardation seen in experiments.

5.1 Digitalization of a bead-packed column for simulation of column experiments

The first step in the workflow of pore-scale modeling is to create a three-dimensional geometry model of a porous medium (Wu et al. 2006; Lin et al. 2016). Recent advances in three-dimensional rock imaging techniques enabled us to capture microscopic details of porous media at high resolutions. X-ray microtomography (XMT) or micro-CT scanners are the most widely used imaging tools in the studies of geologic material and the typical resolution is a few microns (Wildenschild et al. 2002; Arns et al. 2007; Iassonov et al. 2009). Other imaging methods include Scanning Electron Microscopy (SEM), Focused Ion Beams/Scanning Electron Microscopy (FIB/SEM). Once the images are obtained, they are segmented into phase types, i.e., pores and grains. This process is known as image segmentation (Lindquist et al. 1996). There are various approaches to 3D image segmentation. A binary segmentation is the simplest method by which pores (fluid phase) and grains (solid phase) are differentiated to assign digital values (i.e., zero for pores and one for grains) to each voxel of the image. A threshold value or multiple values are applied based on the light intensities of the image. Then the segmented images are recombined to reproduce a three dimensional voxel-based computational replica of porous media.

A computer code to process CT-scanned images (2000 images, 298 KB and 525 × 582 pixels each) of bead-packed columns used in the column experiments was developed. A binary segmentation was implemented to differentiate glass beads and void spaces inside the column and generated the computational domain for LB and RWPT simulations. The images were visually inspected to determine the top and bottom sections of the column. Considering the quality of images, the top was chosen at image # 0161 and the bottom was at image # 1881 (Figure 5-1). The original image files were then cropped to the size of 169 × 169 pixels to remove much of the solid area outside the column. Otsu's algorithm was applied to each cropped image to find appropriate threshold values based on the histogram of the light intensity values (Otsu 1979). These images, as shown in Figure 5-1, show cross-sections of the column. A problem with the images is that the inner surface of the column could not be clearly identified. To determine the location of the inner surface of the column, an ellipse with adjustable major and minor axes and orientation was used to fit the contour of the beads. After the inner surface was determined, pixels inside the column were converted to binary (0: fluid; 1: solid) using different threshold values till the porosity of images matches the porosity of the column in the experiment. The porosity of the digital column was calculated by counting the number of fluid pixels and the total number of pixels inside column (Eq. 5-1).

$$\text{porosity } \phi = \frac{\sum \text{fluid pixels}}{\sum \text{pixels inside column}} = 0.32 \tag{5-1}$$

The real column used in the experiment was constructed by packing large 500-600 µm beads and has a length of 10.26 cm and a diameter of 0.75 cm. The resolution of the images is 51.3 µm per pixel and the distance between consecutive images is also 51.3 µm. A 500~600 µm bead was resolved by 10 to 12 voxels. Figure 5-2 shows one example of the original CT-scanned image and the binary image processed by the established threshold, where white denotes the pore space (image #1590). After thresholding, fluid and solid voxels are represented by zeros and ones, respectively, in a Cartesian lattice system (Figure 5-2). The total 1,722 images were processed and stacked to form the three-dimensional digitalized column for flow and transport simulations (Figure 5-3).
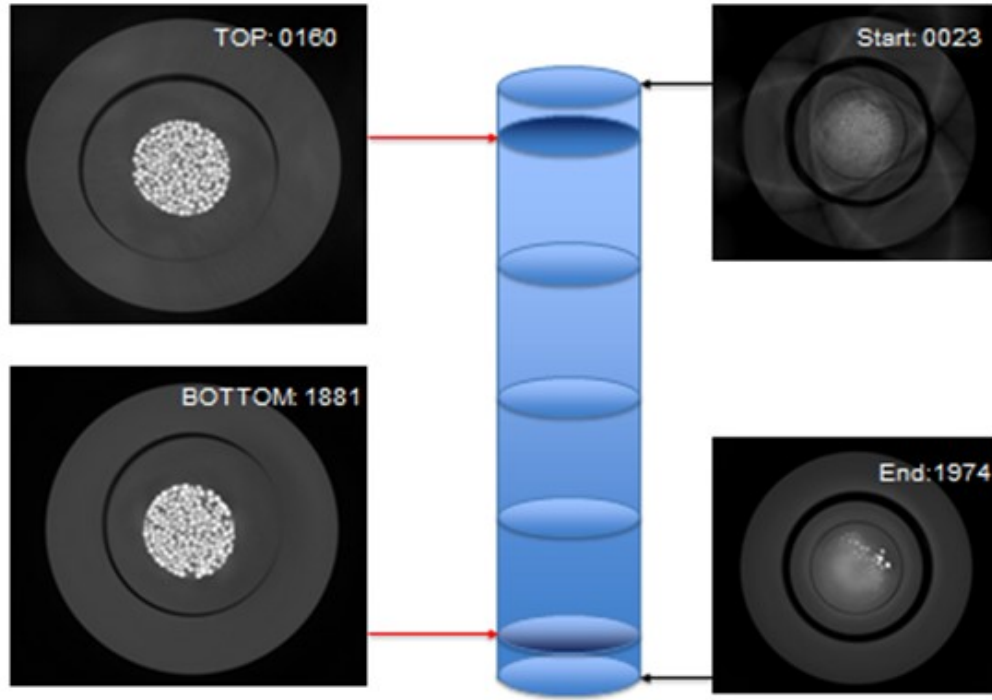
Figure 5-1: The top and bottom images of the bead-packed column.

| (a) | (b) |
| (c) | (d) |
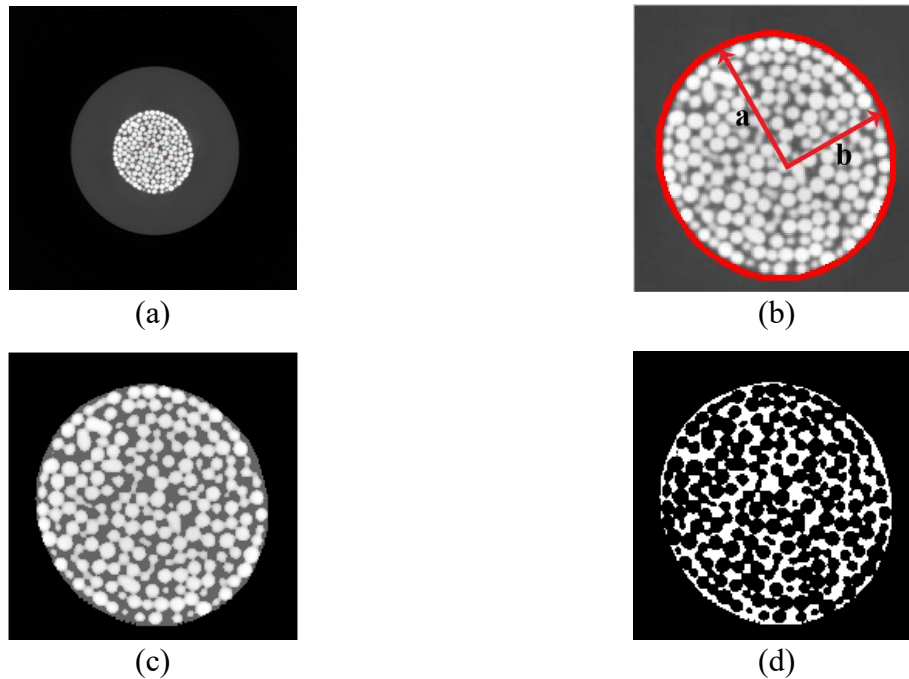
Figure 5-2: Procedure of image processing of CT-scanned column images to generate digitized bead-packed column images (#1590): (a) original CT-scanned image, (b) cross-section of column established by an ellipse, (c) cropped cross-section and (d) binary image of cropped cross-section with pores (white) and grains (black).
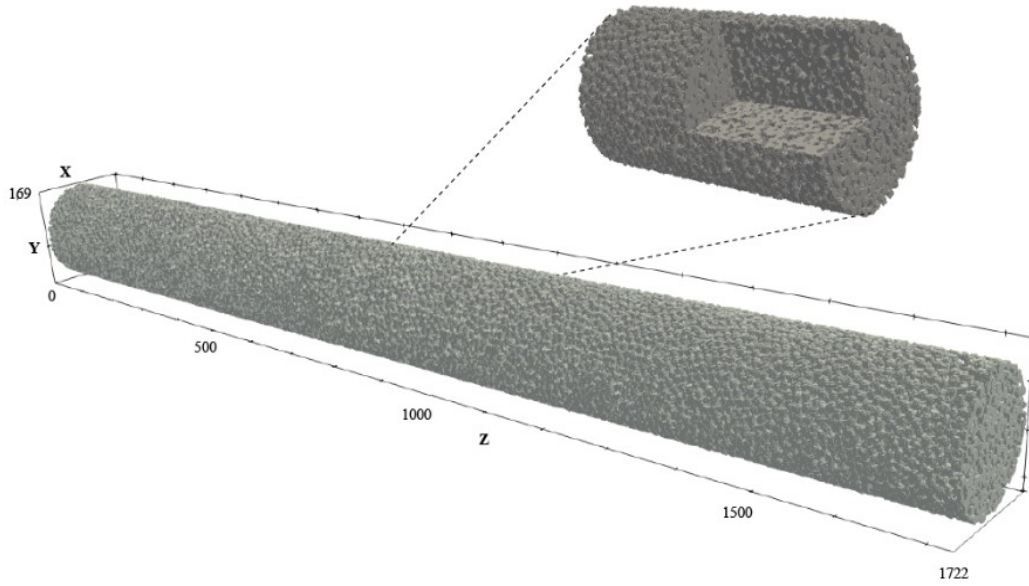
Figure 5-3: Processed images of a bead-packed column are stacked to form a 3D digitalized column for LB and RWPT simulations (only the surfaces of glass beads are visualized). The size of the domain is 169×169×1722 in each direction. A three-quarter section view in the mid-section of the column (from 700 to 1000) is also presented.

5.2 Comparison between solutions of 1D-ADE and experiments

Before presenting our pore-scale simulations, traditional approaches that use solutions of 1D-ADE to analyze laboratory column flow-through experiments are discussed to facilitate comparative discussions with our pore-scale simulations later in this chapter.

Perkins and Johnston (1963) compiled experimental data from unconsolidated sand- or bead-packed column experiments and presented an empirical correlation to estimate longitudinal dispersion coefficients (Eq. 5-2 and Figure 5-4). The parameters in the correlation include flow rate, column diameter, bead diameter, and porosity. The values of these parameters in the column experiments are given in Table 5-1. The molecular diffusion coefficient of iodide (I^-) was taken from literature (Friedman and Kennedy 1955).

$$\frac{D_L}{D_0} = \frac{D_e}{D_0} + 1.75\frac{Ud}{D_0} = \frac{D_e}{D_0} + 1.75Pe$$

$$Pe = \frac{Ud}{D_0}$$

(5-2)

Table 5-1: Experimental details of the bead-packed column experiment

Parameter	Value	Unit
Flow rate	14	cc/day
Column diameter	0.75	cm
Bead diameter	0.05 ~ 0.06	cm
Porosity	0.32	-
Diffusion coefficient of iodide[1]	1.693	cm^2/day

[1]from the work of Friedman and Kennedy 1955

Taking the average grain size as the characteristic length ($d = 0.055$ cm), the Péclet number of the bead-packed column experiment of iodide (I^-) is 3.2 (Eq. 5-3) and it is in the transition zone between the diffusion dominated and the advection (convective dispersion) dominated regimes (Figure 5-4).

$$U = \frac{Q}{A \times \phi} = \frac{14 \text{ cm}^3/\text{day}}{\pi (0.75 \text{ cm})^2 / 4 / 0.32} = 99 \text{ cm}/\text{day}$$

$$Pe = \frac{Ud}{D_0(I^-)} = \frac{(99 \text{ cm}^3/\text{day})(0.055 \text{ cm})}{1.693 \text{ cm}^2/\text{day}} = 3.2$$

(5-3)
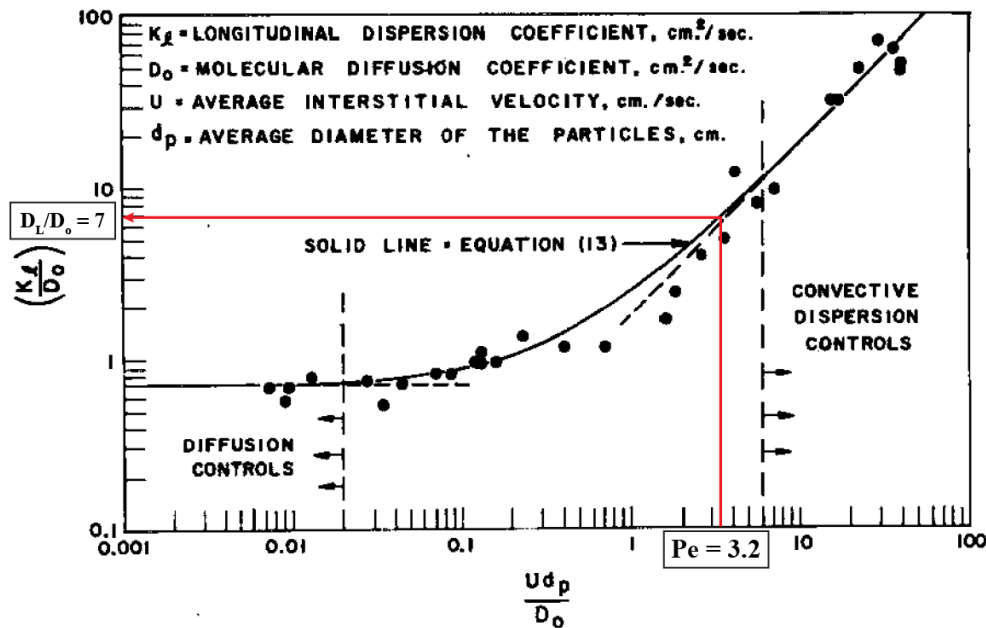
Figure 5-4: Longitudinal dispersion coefficients for unconsolidated, random packs of uniformly sized sands or beads (adapted from Perkins and Johnston 1963): the dimensionless longitudinal coefficient of the iodide column experiment is obtained as $D_L/D_0 = 7$ at $Pe = 3.2$.

The dimensionless longitudinal dispersion coefficient at $Pe = 3.2$ is seven ($D_L/D_o = 7$) from Figure 5-4. The longitudinal dispersion coefficient (D_L) is therefore seven times the molecular diffusion coefficient of iodide ($D_L = 7 \times D_o = 1.3713 \times 10^{-4}$ cm^2/s = 11.85 cm^2/day). Now let us use the analytical solution of 1D-ADE (Eq. 2-19) to construct a breakthrough curve for iodide (I^-). Figure 5-5 shows the comparison between the solution of 1D-ADE and the column experiment. There are a few notable differences. First, for the initial point of breakthrough, 1D-ADE predicts that iodide should be detected at about 0.7 pore volume (PV) whereas in the experiment iodide was detected at 0.5 PV. Second, the only experimental data point measured in the build-up portion of the experimental breakthrough curve seems more retarded than the 1D-ADE prediction. Overall, the solution of 1D-ADE (Eq. 2-19) using the empirical correlation (Eq. 5-2) for longitudinal dispersion does not quite accurately predict the effluent profile of the bead-packed column experiment. This discrepancy could be attributed to many sources, for instance, the limitations in the traditional 1D-ADE, the applicability of the empirical correlation to the column experiments, and uncertainties in the experimental setup and measurements such as packing and pore volume, etc. In the next section, we will add the results of pore-scale simulations into this comparison.
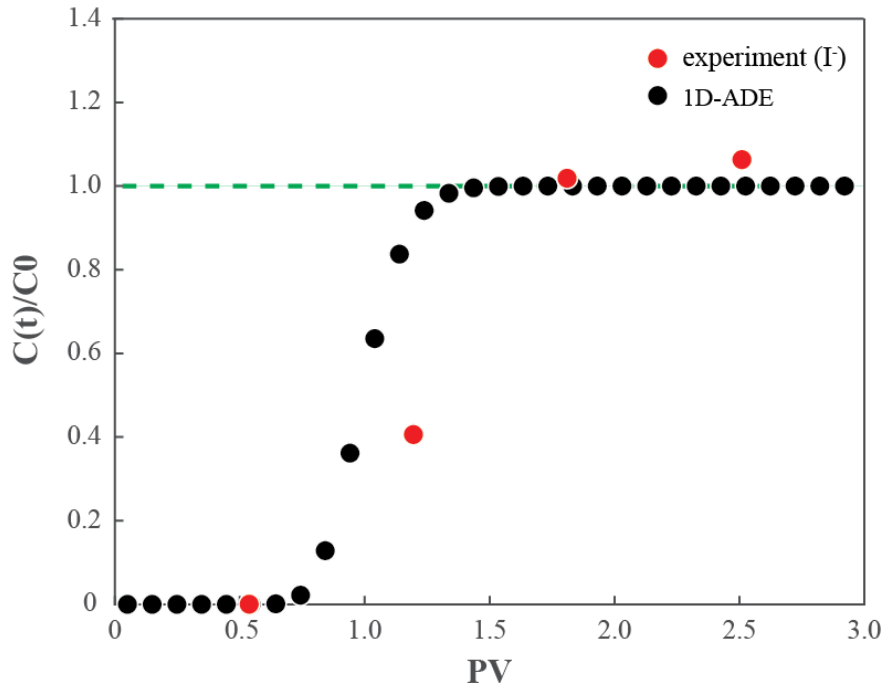
Figure 5-5: A comparison between the breakthrough curve from the analytical solution of 1D-ADE and that from column experiments.

5.3 LB simulation of fluid flow in packed-column

The D3Q19 LB code was used to obtain the velocity field within the digitalized bead-packed column. The simulation was run to 20,000 LB time steps, at which fluid flow in the column reached the steady state. The computational domain size was 169 × 169 × 1732 including additional five fluid layers on both ends of the column in the z-direction to maintain periodicity of the computational domain. A constant body force was applied in the z-direction to drive the fluid flow. The velocity in the direction of fluid flow is visualized in Figure 5-6. A three-quarter section view (from 700 to 1000) as well as plane views in each direction are also presented.

(a)

(b)

(c)

(d)

(e)
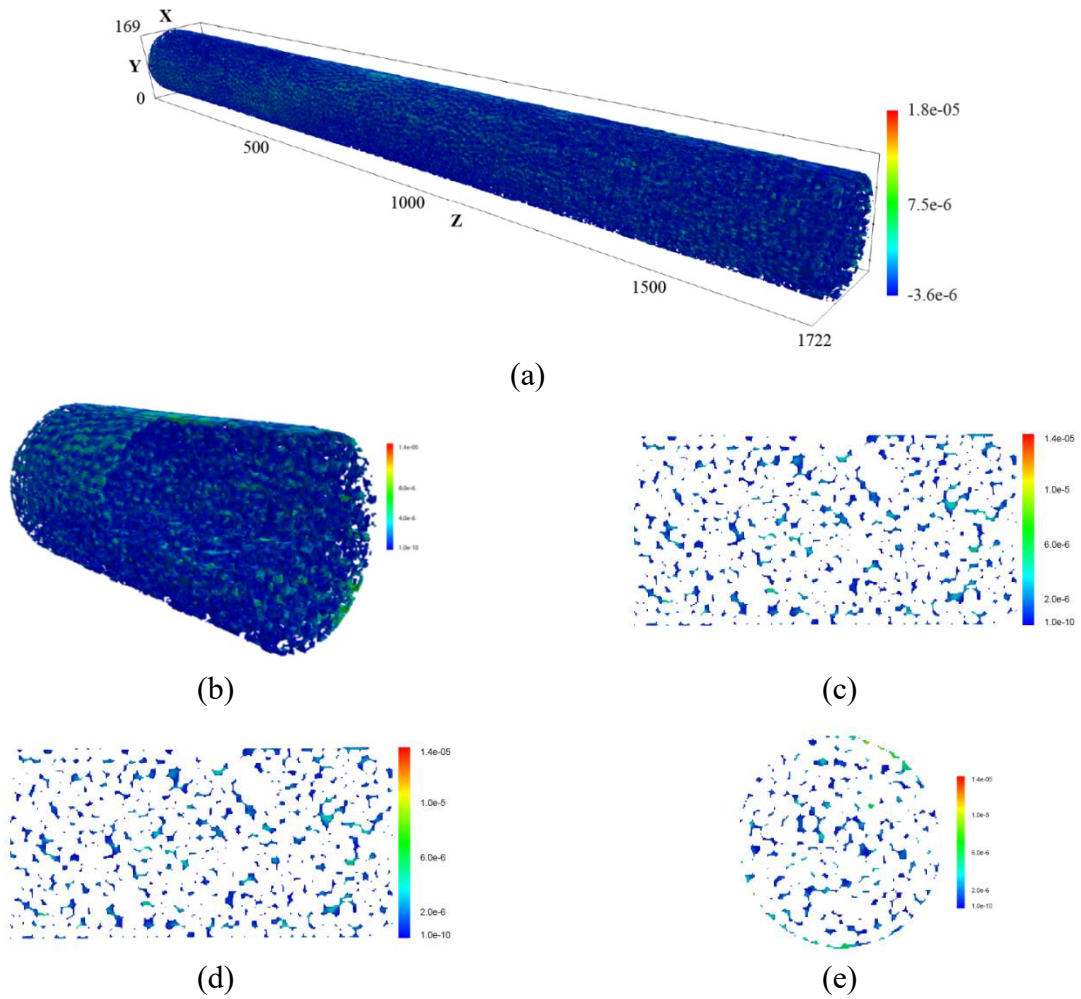
Figure 5-6: Visualization of z-velocity obtained from LB simulation: (a) z-velocity in the entire column, (b) z-velocity from a three-quarter section view from image number 700 to 1000, (c) z-velocity on a zx-plane, (d) z-velocity on a yz-plane, (e) z-velocity on a xy-plane. All three planes cut through the center of the column (84, 84, 850).

33

The permeability of the column was calculated at 156 darcy. This permeability is close to the range of permeability estimated using the Kozeny-Carman equation (Eq. 5-4): $k_{K\text{-}C}= 99 \sim 144$ darcy. The parameters of LB simulation are summarized in Table 5-2

$$k_{K-C} = \frac{d^2}{180} \frac{\phi^3}{(1-\phi)^2} = \frac{(500 \sim 600 \text{ μm})^2}{180} \frac{0.32^3}{(1-0.32)^2} = 99 \sim 144 \text{ darcy} \qquad (5\text{-}4)$$

Table 5-2: Parameters of LB simulation of the column experiment

Parameter	Value
Grid type	Cartesian
Domain size	169 × 169 × 1732
Total number of grids	49,467,652
Total number of fluid nodes	10,117,521
Body force	[0 0 10^{-6}]
Collision operator	MRT
Relaxation time	1.0
Boundary condition	Periodic
Simulation time step	20,000
# of CPUs	128

5.4 RWPT simulation of iodide

In the column experiment, iodide (I^-) was used as a non-adsorbing solute since it does not adsorb to glass beads. The velocity field obtained from LB simulation was passed to RWPT. The diffusion coefficient and time step size of RWPT were chosen to match the experimental Péclet number so that tracers in RWPT travel with the same advection-diffusion dynamics as the experiment. The definition of the Péclet number is the same as that in Eq. 5-2 except that pore velocity is used.

Here, we note the sources of the diffusion coefficient, also termed the "free-solution" diffusion coefficient, of ionic species in aqueous solution including iodide (I^-) and cesium (^+Cs) in the literature. Robinson and Stokes (2002) calculated diffusion coefficients of ions using the Nernst-Einstein equations. (Aslan et al. 2014). Yuan-Hui and Gregory (1974), Lerman (1979), and Quigley et al. (1987) also presented diffusion coefficients of ions in soils. Friedman and Kennedy (1955) measured diffusion coefficients of radioactive ions in aqueous solutions using the open-ended capillary method. Sato et al. (1996) measured ionic diffusion coefficients of radioactive

elements in free water and their values are comparable to those reported prior to their study. In this study, the molecular diffusion coefficients of iodide (I^-) and cesium (Cs^+) at the condition most comparable to the column experiment were taken from the work of Friedman and Kennedy (1955) (Table 5-3). Parameters of the RWPT simulation for iodide (I^-) transport are summarized in Table 5-4.

Table 5-3: Molecular diffusion coefficients of iodide and cesium in 11.36% solution at $25 \pm 0.0005°$ (reproduced from Friedman and Kennedy 1955)

Type of solute	Value	Unit
Iodide (I^-)	$1.959 \pm 0.020 \times 10^{-9}$	m^2/s
Cesium (Cs^+)	$2.047 \pm 0.011 \times 10^{-9}$	m^2/s

Table 5-4: Parameters of RWPT simulation of iodide transport

Parameter	Value
Grid type	Cartesian
Domain size	$169 \times 169 \times 1732$
Grid resolution	51.3 μm / pixel
Total number of grids	49,467,652
Total number of fluid nodes	10,117,521
Number of tracers initialized per grid	1
Superficial velocity from LBM	2.06616×10^{-7}
Péclet number	1.03
Dimensionless diffusion coefficient	3.66×10^{-6}
RWPT time step size	6.59064×10^{3}
Duration of simulation	1.45211×10^{6} (5 PV)
Number of cores used	128

RWPT simulations were run with the above parameters to generate a breakthrough curve for iodide. This breakthrough curve is compared to that from the column experiment in Figure 5-7. Statistical noise in the simulated breakthrough curve was smoothed by integrating the number of tracers over a longer sampling time interval. The breakthrough curve generated directly from the RWPT simulation shows the typical trend of a conservative solute with low to moderate Péclet number. The simulated breakthrough curve is comparable to the experimental data on both the initial breakthrough at 0.5 PV and the late-time behavior. The experimental data point in the build-up part, just like the comparison with the solution of the 1D-ADE, arrives later than the simulation. Due to limited experimental data, it is not easy to tell what factors contributed to this difference.

When the solution of the 1D-ADE is added to the comparison, it may be seen that the agreement between the solution of 1D-ADE and the result of RWPT is better than the agreement between RWPT and experiments (Figure 5-8). In the experiments, the calculation of pore volume is usually not very accurate. The difference between experimental breakthrough curve and those from 1D-ADE and RWPT simulation is therefore likely due to uncertainties in the experiment.
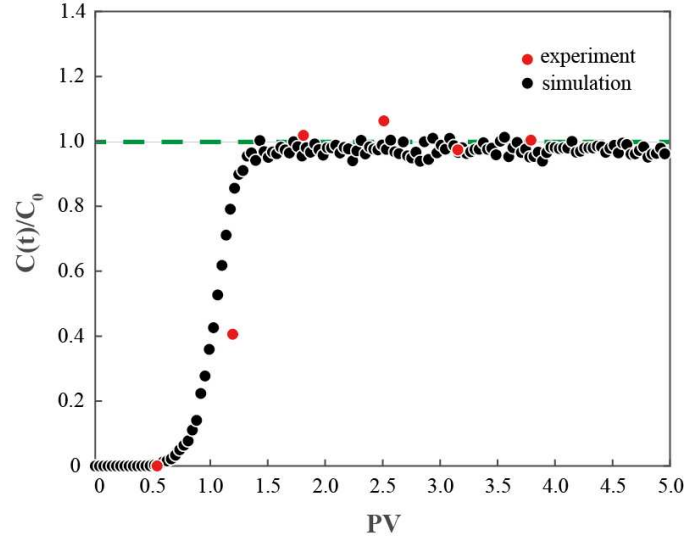
Figure 5-7: Comparison between the breakthrough curve from RWPT simulation (black) and that from the experiment (red).
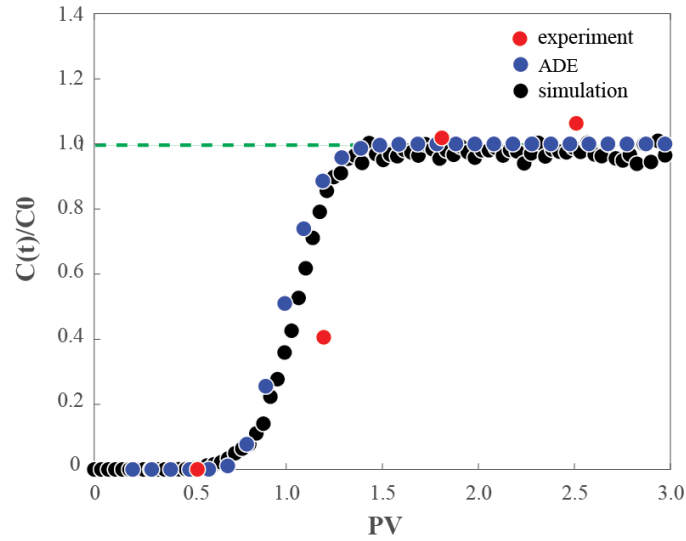
Figure 5-8: Comparison among the solution of 1D-ADE (blue), breakthrough curve from RWPT (black), and that from experiment (red).

5.5 Tortuosity and longitudinal dispersion coefficient from RWPT

Tortuosity is one of the key parameters that characterizes advection-dispersion in porous media. As reviewed by Bear (1972), it is the measure of the effect of tortuous paths in a porous medium on diffusive transport. Tortuosity is normally defined as the square of the ratio of the averaged effective length of transport pathways to the end-to-end length of the porous medium. There have been scores of attempts to determine tortuosity of the porous medium, theoretically, empirically and experimentally. Experimental approaches including electrical ultrasonic method, resistivity measurements and diffusion coefficient measurements, estimate tortuosity quite successfully but very time consuming (Boudreau 1996).

The tortuosity of porous media can be numerically obtained using RWPT by simulating pure diffusion of tracers. The tortuosity of the bead-packed column, studied in this chapter, was obtained as the ratio of molecular diffusion coefficient to effective diffusion coefficient (Eq. 5-5). The latter was obtained from the mean square displacement (MSD) of tracers in pure diffusion

$$\tau = \left(\frac{L_{eff}}{L} \right)^2 = \frac{D_o}{D_e} \tag{5-5}$$

A RWPT simulation of pure diffusion was performed. Tracers were uniformly initialized in each fluid voxel to achieve fast convergence of the time-dependent dispersion tensor (Eq. 4-6) (Maier et al. 2000). The position of every tracer was tracked and the squared displacements in the flow direction were averaged and plotted as a function of time steps, as exemplified in Figure 5-9.
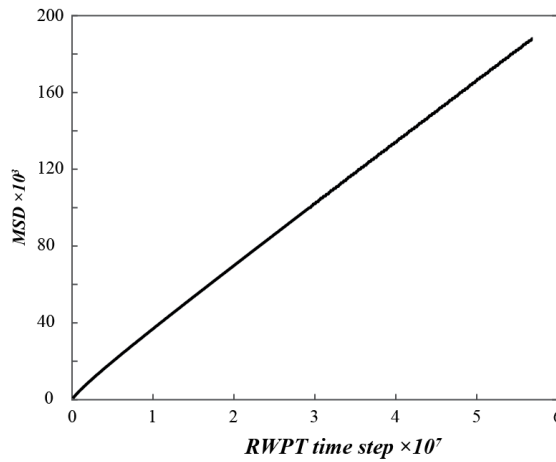
Figure 5-9: The mean square displacement (MSD) of tracers under pure diffusive process to estimate the tortuosity of the column (in RWPT simulation unit).

The effective diffusion coefficient (D_e) in the flow direction is obtained as half of the slope of the plot (MSD = $2Dt$). The tortuosity of the bead-packed column is calculated at 2.214. This value of the tortuosity obtained from our pore-scale simulations agrees well with tortuosity-porosity correlations for spherical particles cited in literature (Bear 1972; Dullien 1975; Comiti and Renaud 1989; Mauret and Renaud 1997; Koponen et al. 1996) (Table 5-5).

Table 5-5: Tortuosity-porosity correlations for spherical particles in literature

Literature	Correlation	Tortuosity
Bear (1972), Dullien (1975)	$\dfrac{L_{eff}}{L} = \dfrac{1}{\phi^{0.33}}$	2.120
Comiti and Renaud (1989)	$\dfrac{L_{eff}}{L} = 1 - 0.41\ln\phi$	2.152
Mauret and Renaud (1997)	$\dfrac{L_{eff}}{L} = 1 - 0.49\ln\phi$	2.427
Koponen et al. (1996)	$\dfrac{L_{eff}}{L} = 1 - 0.8(1-\phi)$	2.384

The asymptotic longitudinal dispersion coefficient in the flow direction was obtained from RWPT simulation. The mean square displacement and time-dependent dispersion coefficient normalized by the molecular diffusion coefficient (D_L/D_o) in the flow direction is shown in Figure 5-10. The asymptotic dimensionless dispersion coefficient was 5.74, and the steady-state dispersion coefficient was 9.72 cm^2/day.

(a) (b)
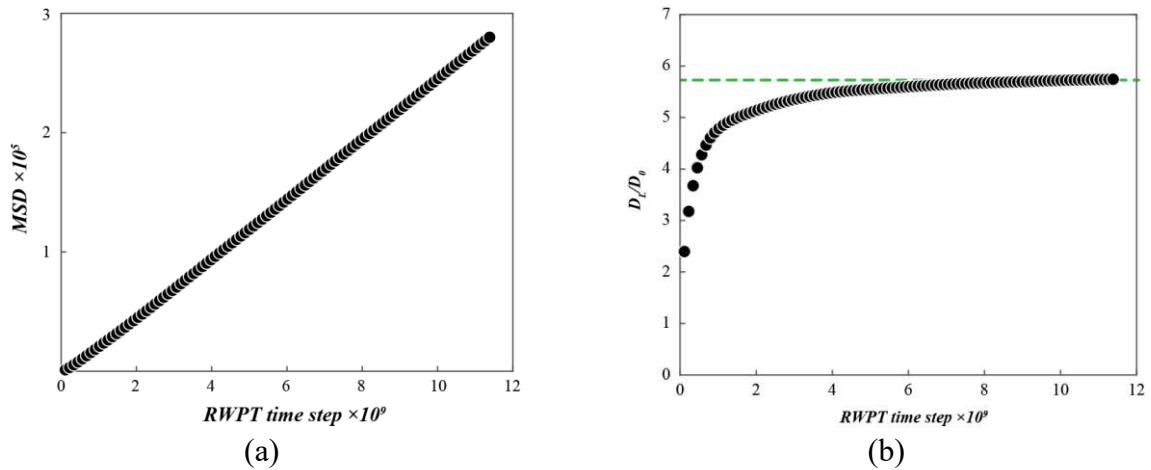
Figure 5-10: The mean square displacement (a) and normalized longitudinal dispersion coefficient (b).

Now macroscopic properties including permeability, tortuosity, and longitudinal dispersion coefficient were obtained from our pore-scale direct numerical simulations, and they are compared with empirical correlations (Table 5-6).

Table 5-6: A summary of permeability, tortuosity, and longitudinal dispersion coefficient obtained from LB and RWPT simulations and those estimated using empirical correlations

Properties	Simulated	Correlation	Unit
Permeability (k)	156	99~144	darcy
Tortuosity (τ)	2.214	$2.120 \sim 2.427$	-
Dispersion coefficient (D_L)	9.72	11.85	cm^2/day

5.6 Implementation of adsorption-desorption processes in RWPT

Sorption refers to a collection of processes through which solutes are transferred or removed from the solution to the solid phase (Fetter 2008). Sorption results from interactions between solutes and solid surfaces. Mechanisms behind sorption processes can be adsorption, electrostatic interaction, chemisorption, and absorption. Adsorption or physisorption is a process in which a solute molecule is attached to a solid surface by van der Waals force. For electrostatic interaction, cations (anions) in the solution are attracted to solid surfaces that are negatively (positively) charged. Chemisorption involves formation of chemical bonds that incorporates solutes onto the structure of the solid surface. Lastly, solutes may diffuse into the interior of the solid (Wood et al. 1990) and this process is called absorption. Most times, these processes are collectively called "sorption" since they cannot be easily differentiated especially in natural subsurface systems. Sorption processes can be considered from two perspectives: equilibrium and kinetics. Equilibrium sorption refers to situations where the solute concentration in solution is in equilibrium with the solute sorbed on adsorbents (i.e., solid phase). Kinetic sorption, on the other hand, studies the dynamics of sorption processes that drive the evolution from non-equilibrium toward equilibrium.

Adsorption processes make some solutes move slower than the motion of bulk fluid. If adsorption-desorption processes are reversible in equilibrium, they lead to equilibrium retardation as in Figure 2-2. This equilibrium retardation was also observed in the column experiment of cesium (Rod et al. 2018). The RWPT code was modified to simulate solutes with adsorption-desorption equilibrium. The equilibrium adsorption model was implemented by introducing a

39

probability of adsorption (P_a) and another probability of desorption (P_d) to determine whether a tracer adsorbs on or leaves the surfaces of the solid phase. A random probability (P_{rand}) is generated when a tracer is intercepted by an interface between the liquid and solid phases. If this random number is smaller than the prescribed probability of adsorption ($P_a > P_{rand}$), the tracer is adsorbed on the surface. If not ($P_a < P_{rand}$), a specular reflection is carried out to keep the tracer in solution. For tracers that are already adsorbed, random numbers are generated to decide whether they should be sent back to solution. An adsorbed tracer would leave solid surface if a random number, generated specifically for this tracer, is smaller than the prescribed probability of desorption ($P_d > P_{rand}$). Otherwise, it would stay on the surface during this time step, waiting for the random number for the next time step. To simulate adsorption-desorption equilibrium under periodic boundary condition, two types of tracers were used in RWPT (Figure 5-11).
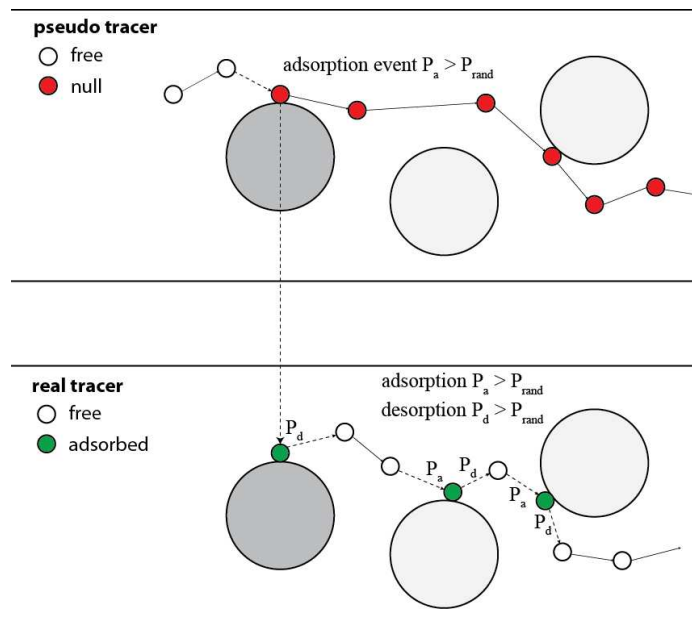
Figure 5-11: Illustration of "pseudo tracer" and "real tracer" implemented in RWPT to simulate the equilibrium adsorption-desorption.

"Pseudo tracers" are initialized at pseudo positions at the beginning of simulation. When a pseudo tracer become active and hit the solid phase, a random probability is compared with a prescribed probability of adsorption. If a random probability is smaller than a probability of adsorption, the adsorption condition is met, and then a "real tracer" is copied and allocated to a variably designated memory for real tracers. At this moment, the pseudo tracer is nullified with

the adsorption event recorded. This pseudo tracer keeps moving to the exit without being adsorbed to satisfy periodic boundary condition. The copied real tracer stays on the interface between the liquid and solid phases until desorption condition is met. Contrary to pseudo tracers, real tracers undergo adsorption-desorption every time adsorption or desorption condition is met. When they cross the exit, they are counted in the construction of breakthrough curves, and then removed from computational domains. The memories for real-tracers are dynamically allocated to improve memory efficient. We implemented dynamic memory allocation for real-tracers.

5.7 Simulation of adsorption-desorption equilibrium

The governing differential equation for continuum-scale solute transport with adsorption-desorption was presented in Eq. 2-13. The partitioning coefficient (K_d) is the measure of equilibrium solute partition between the solid and liquid phases due to reversible adsorption and desorption. Under this equilibrium, the tendency for solute in solution to adsorb to the solid phase is balanced by the tendency for adsorbed solute to return to solution. K_d is usually measured from American Society of Testing and Materials (ASTM) batch experiments (ASTM 2010; Kaiser and Guggenberger 2000) in which a mass of solid, i.e., rock or soil, is immersed in a known volume of solution for enough time so that the solute achieves equilibrium between the solid and liquid phases (Batu 2005). Results from such experiments are generally presented in the form of an isotherm, i.e., concentration of the solute in the solid phase (S) (µg/kg) plotted as a function of the solute concentration in solution (L) (µg/L). For linear sorption isotherms, the slope of the isotherm is K_d (L/kg or mL/g).

K_d for cesium (Cs^+) was measured in laboratory batch experiments. The K_d for Cs^+ with specific area, particle density, bulk density and porosity of the column are presented in Table 5-7 from the column experiment (Rod et al. 2018).

Table 5-7: Sorption partitioning coefficient (K_d) of cesium, specific surface area, and particle density for glass beads (reproduced from Rod et al. 2018)

Parameter	Value	Unit
Partitioning coefficient	1.00	mL/g
Surface area	0.0094 ± 0.0001	m^2/g
Bead density	2.47	g/cm^3
Bulk density	1.41	g/cm^3

In RWPT, probability of adsorption and that of desorption were determined from simulations of the batch experiments. Assuming that a single tracer corresponds to certain mass of solute, K_d defined as the ratio of solute mass per solid mass (µg/kg) to solute mass per solvent volume (µg/L) may be rewritten using the number of tracers on the surface of solid to the number of tracers in the liquid phase (Eq. 5-6).

$$K_d = \frac{C_S}{C_L} = \frac{\text{number of tracers on solid } (N_S)}{\text{number of traers in liquid } (N_L)} \times \frac{\text{volume of liquid}(V_L)}{\text{surface area}(A_S)} \tag{5-6}$$

With the help of Eq. (5-6), K_d = 1 mL/g for Cs^+ can be converted to the ratio of surface concentration of tracers to volume concentration of tracers. RWPT simulations were carried out to determine P_a and P_d that would reproduce this ratio. In these simulations, packings of glass beads on which solutes are adsorbed and desorbed in the batch experiments were modeled as a body-centered cubic (BCC) array periodic in all three directions. The BCC domain with the size of 13 × 13 × 13 was set to match the porosity of the column of the experiment. Tracers that are initially put in the liquid phase move with pure diffusive motion and are allowed to adsorb on the surfaces of spheres in the BCC array based on the prescribed P_a. Tracers adsorbed on the wall can be released back to the liquid phase based on the prescribed P_d. Now K_d can be expressed in terms of the ratio of the number of tracers on the surface of beads (N_s) to the number of tracers in the fluid (N_L) and the ratio of mass of the solid (M_s) and the volume of solution (V_L) (Eq. 5-7).

$$M_s = \rho_s \frac{4}{3}\pi r^3$$
$$A_s = 4\pi r^2 = 4\pi \left(\sqrt[3]{\frac{3M_s}{4\pi\rho_s}} \right)^2 \tag{5-7}$$
$$K_d = \frac{V_L}{M_S} \times \frac{N_S}{N_L}$$

Figure 5-12 shows K_d achieved by three different combinations of P_a and P_d. For the combinations (P_a = 5.0 × 10^{-4}; P_d = 6.8 × 10^{-5}) and (P_a = 5.0 × 10^{-4}; P_d = 2.7 × 10^{-5}), the simulated values of K_d are about 0.5 and 1.5, respectively. The simulated K_d matches the experimental K_d when P_a and P_d are 5.0 × 10^{-4} and 1.35 × 10^{-5}, respectively (P_a / P_d = 37.04). Therefore, this combination is one set of probabilities that would reproduce K_d of Cs^+ in the column experiments.
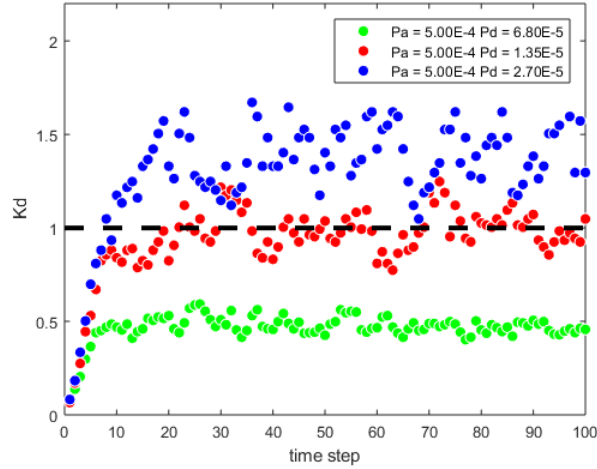
Figure 5-12: Simulated adsorption-desorption equilibriums at three different combinations of P_a and P_d.

Note that the above solution is one of the many sets of P_a and P_d that can produce the same K_d. Figure 5-13 shows that, as long as $P_a / P_d = 37.04$ K_d = 1 mL/g can always be reproduced. However, the transient behavior is different. This finding suggests that K_d as a parameter describing equilibrium is only a function of P_a / P_d. The specific values of probabilities under the condition that P_a / P_d is held constant control the rate toward equilibrium. As Rod et al. (2018) did not give any rate information of the batch experiments, the probability of adsorption was arbitrarily chosen, then a probability of desorption was determined from P_a / P_d that matches the experimental K_d.
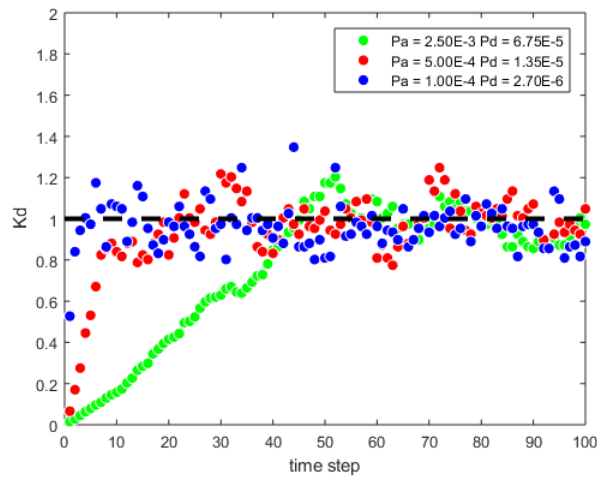
Figure 5-13: The partitioning coefficient from numerical batch experiments using the same ratio of a probability of adsorption and desorption ($P_a / P_d = 37.04$).

A time-lapse sequence of tracer distribution in the BCC array, from the simulation with $P_a = 5.0 \times 10^{-4}$ and $P_d = 1.35 \times 10^{-5}$ is given in Figure 5-14. With $P_a / P_d = 37.04$, it is clear to see that more and more tracers became adsorbed as simulation progressed.
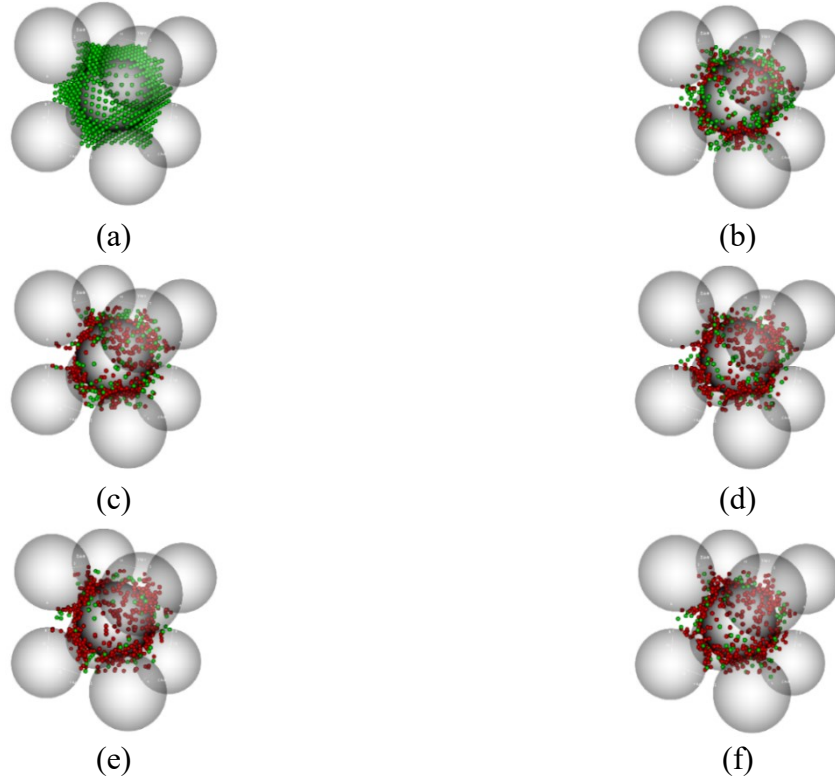
Figure 5-14: Time-lapse sequence of simulation with $P_a = 5.0 \times 10^{-4}$ and $P_d = 1.35 \times 10^{-5}$: (a) time step = 0 and $K_d = 0$, (b) time step = 3 and $K_d = 0.231$, (c) time step = 6 and $K_d = 0.509$ (d) time step = 10 and $K_d = 0.907$ (e) time step = 20 and $K_d = 0.963$, (f) time step = 25 and $K_d = 0.925$ (red denotes adsorbed tracers and green denotes tracers in solution).

In an attempt to see the effect of probabilities of adsorption and desorption on the level of breakthrough curves, different values of P_a and P_d having the same ratio were tested and the results are presented in Figure 5-15. It shows that, although the retardations in the five curves are similar, the build-up part of the breakthrough curve becomes steeper as the probability of adsorption increases. This feature clearly shows that the traditional method based on a single value of partitioning coefficient from laboratory batch experiment is limited in predicting transient behavior of effluent concentration. Hence, this degree of uncertainty may be avoided if one considers, in addition to the partitioning coefficient, knowledge on the kinetics of adsorption and desorption

processes. If experimental data on how K_d changes over time are available, unique values of P_a and P_d can be determined by simulating laboratory batch experiments.
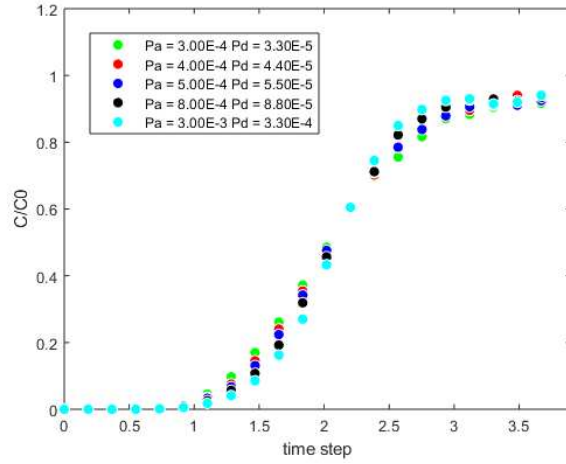
Figure 5-15: BTCs for various ratios of P_a and P_d

5.8 RWPT simulation of cesium ion transport

Using probabilities of adsorption and desorption determined from the previous section ($P_a = 5.0 \times 10^{-4}$ and $P_d = 1.35 \times 10^{-5}$), RWPT simulation was performed to simulate Cs^+ transport in the same column as that used in the iodide simulation. Parameters of this simulation are summarized in Table 5-8.

Table 5-8: Parameters of RWPT simulation of cesium transport

Parameter	Value
Grid type	Cartesian
Domain size	$169 \times 169 \times 1732$
Total number of grids	49,467,652
Total number of fluid nodes	10,117,521
Total number of tracers	1,012,551
Boundary condition	Periodic
Acceleration applied in z direction	1×10^{-6}
Superficial velocity from LBM	2.06616×10^{-7}
Péclet number	0.99
Maximum velocity	1.76595×10^{-5}
Dimensionless diffusion coefficient	3.823688×10^{-6}
Probability of adsorption/desorption	$5.0 \times 10^{-4} / 1.35 \times 10^{-5}$
Time step size	6.4788×10^{3}
Simulation time step (5PV)	1.45211375×10^{6}
Number of cores used	128

45

The breakthrough curves from our RWPT simulation is presented in Figure 5-16. The breakthrough curves of the experiment and 1D-ADE with the Perkins and Johnston correlation are also presented for comparison. As shown in Figure 5-16, RWPT successfully generated a breakthrough curve for Cs^+ that compares well with the experimental data. Admittedly, as there are only three experimental data points, this comparison cannot be considered as highly quantitative. However, some conclusions can still be drawn. The dispersion coefficient of Cs^+ was obtained using the Perkins and Johnston correlation (Figure 5-4), and the solution of equilibrium retardation with $K_d = 1$ is presented. The initial breakthrough time predicted by our pore-scale simulation (about 1 to 2 PV) is earlier than that of the 1D-ADE solution (4 PV). Our pore-scale simulation therefore appears to be more dispersive than the solution of 1D-ADE. The retardation factor estimated graphically based on the value of $C/C_0 = 0.5$ is 5.16 ($R_d = 5.16$), which agrees well with the retardation factor ($R_d = 5.4$) calculated using Eq. 2.14 with the data of the laboratory batch experiment (Table 5-7). Clearly, when compared to that of iodide (I^-), the breakthrough curve of cesium (Cs^+) was significantly retarded due to adsorption-desorption in the column (Figure 5-17).
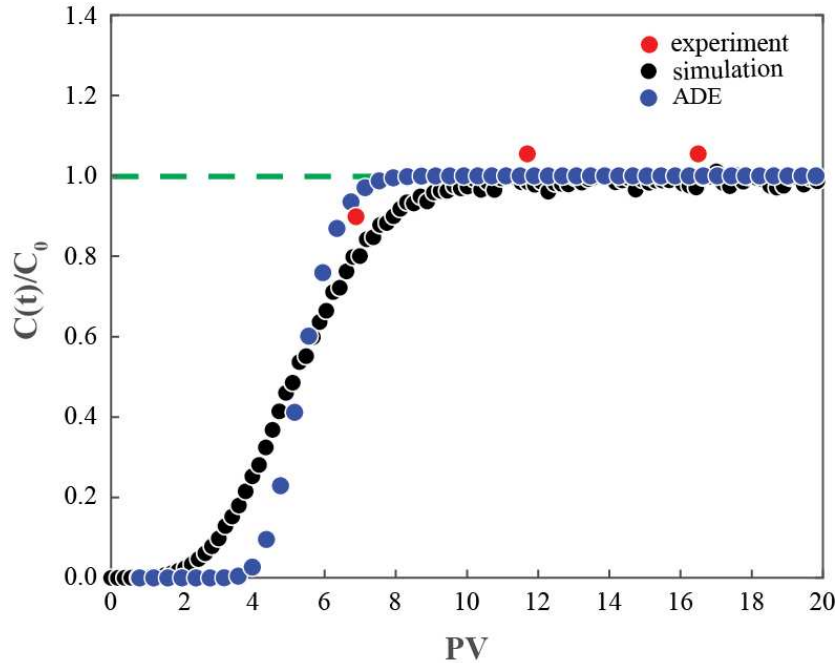
Figure 5-16: Simulated BTC (black) for cesium under equilibrium sorption-desorption relative to the analytic 1D-ADE ($D_L = 12.38$ cm^2/day and $R_d = 5.4$) and the experimental data (red) of the column experiment.
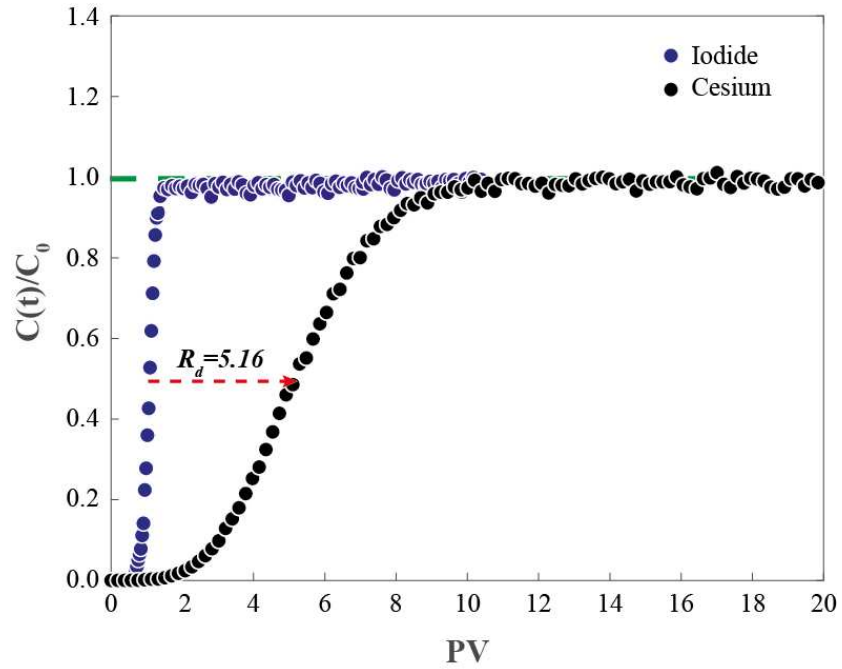
Figure 5-17: Simulated BTC for cesium under equilibrium sorption-desorption in the column experiment with the retardation factor (R_d = 5.16).

CHAPTER 6

PORE-SCALE SIMULATION OF MICROFLUIDICS EXPERIMENTS

This chapter presents the results of pore-scale simulations for a bead-based microfluidics experiment in which colloids propagate through electrostatically homogeneous and heterogeneous porous media analogues (PMAs). Voxel-based computational domains were generated based on the center coordinates and radius of the beads. The range of electrostatic attraction between positively charged beads and negatively charged colloids was estimated and implemented in RWPT to simulate the irreversible deposition of colloids under this favorable condition. In addition, the effect of blocking was incorporated by decreasing a probability of deposition of a colloid on a positively charged bead as more colloids are deposited on the surface of the bead.

6.1 A bead-based microfluidics experiments

Guo et al. (2016) used a bead-based microfluidic platform of porous media analogue (PMA) to investigate colloid transport through electrostatically heterogeneous porous media. The PMA was constructed by injecting amine-functionalized beads one-by-one into a microfluidic device with a stepping change in the height. Beads are caught at the location where the height of the device is suddenly reduced. Gradually, stopped beads fill the space upstream of the location of height change and form a porous medium. Most beads have their vertical positions either against the top wall (red) or against the bottom wall (green) of the device (Figure 6-1). Colloidal particles injected into PMA have diameter approximately 0.5 μm. They were made of polystyrene (PS) with fluorescent coating exhibiting net negatively charged surfaces. These engineered colloids were injected into PMA from the same side through which the beads were injected, at a constant volumetric flow rate of 1 nL/s. The number of colloids that had passed through the beads was counted using epifluorescence microscopy to construct breakthrough curves. Various ratios of positively charged to negatively charged beads were used to investigate the impact of surface charge heterogeneities. The portion of positively charged beads in the packing ranged from 0% to 50%. The dimensions of the PMA are summarized in Table 6-1 and the schematics of the bead-based micromodel experiment are given in Figure 6-1. Guo et al. (2016) presented more details on the precedure of fabricating PMAs with charge heterogeneity.

Table 6-1: Dimensions of PMA domain

Parameter	Dimension	Unit
Domain size	$600 \times 15 \times 1981$	-
Grid resolution	1	μm/pixel
Total number of grids	20,375,894	-
T-junction height	8	μm
Diameter of beads (negative / positive)	9.9 / 10.2	μm
Diameter of pillar	24	μm
Flow rate	1.0	nL/s
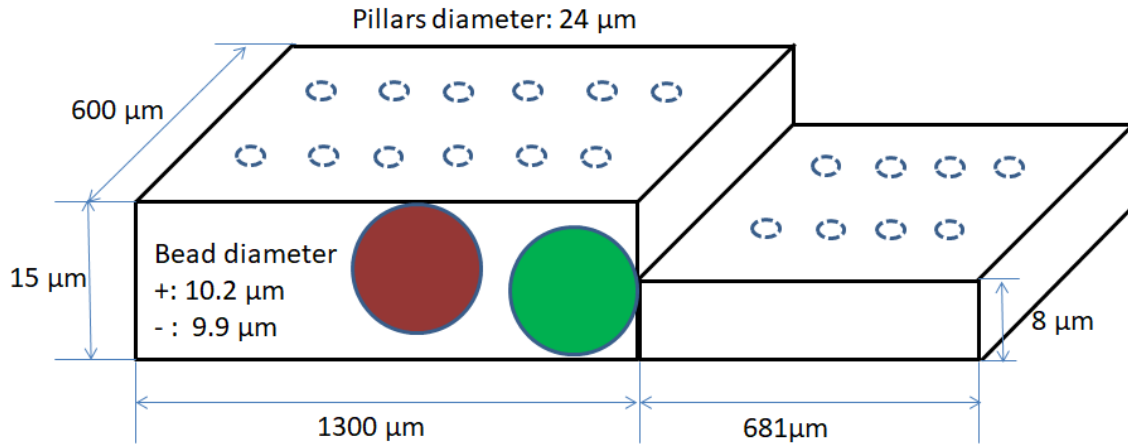
Figure 6-1: Schematics of bead-based microfluidic porous media analogue: positively charged bead (red), negatively charged bead (green), and pillars (dotted). This schematics is not to scale.

6.2 Reconstruction of microfluidic porous media analogues

A customized code was written to generate voxel-based computational domains for LB and RWPT simulations of colloid transport in microfluidic PMAs. The location of the center of each bead in a transparent PMA, including the information on whether the bead is adjacent to the top or the bottom wall of the PMA, was captured through confocal imaging. Different from simulations carried out for bead-packed columns that directly used images from CT scan, here the coordinates of centers of beads were used to reconstruct the digitalized PMAs. The diameter of negatively charged beads and positively charged beads was set to 10 μm. The pillars in PMAs were also incorporated into the computational domains so that they are realistic. Figure 6-2 shows the computational domain constructed for the electrostatically homogeneous PMA with no positively charged beads. The pillars and the walls of the chamber of PMA are not visualized.
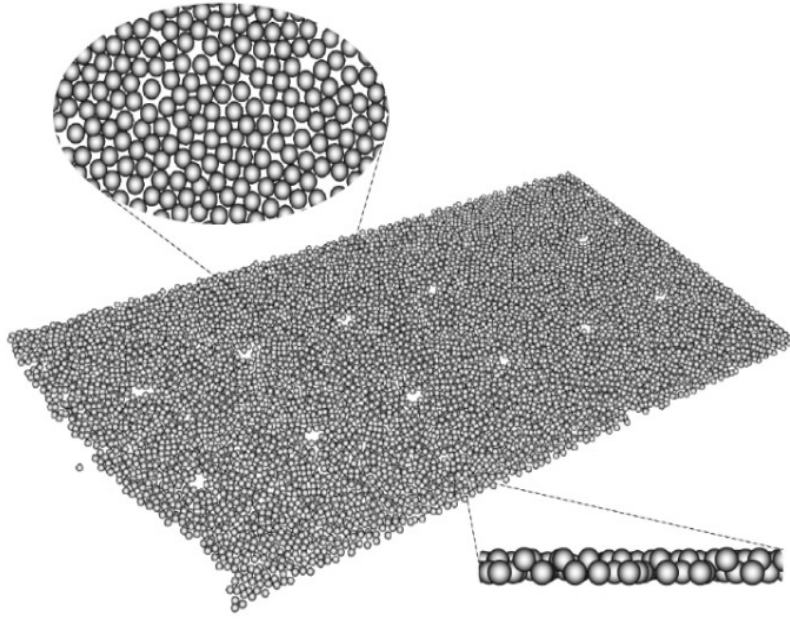
Figure 6-2: Computational domain for the electrostatically homogeneous PMA with 0% positively charged beads: grey (negatively charged beads).

Electrostatically heterogeneous PMAs consist of negatively charged beads and positively charged beads. The percentages of positively charged beads are 4%, 9%, 13%, 17%, 25% and 50%. To distinguish voxels that belong to positively charged surfaces from those that belong to negatively charged surfaces, in the computational domains one was assigned to voxels in negatively charged beads, walls and pillars, and two was assigned to those in positively charged beads. Values of zero were assigned to voxels in pores. Detailed information on each PMA is presented in Table 6-2. The computational domains are visualized in Figure 6-3. Beads in grey and red colors denote negatively charged beads and positively charged beads, respectively.

Table 6-2: Number of positively charged beads (p-bead) and negatively charged beads (n-bead) on the top and bottom walls, and porosity of PMAs

Parameter	0%	4%	9%	13%	17%	25%	50%
Total # of bead	7,245	6,310	6,566	6,966	6,815	7,575	7,018
# of p-bead	0	240	557	957	1,168	1,788	3,364
# of n-bead	7,245	6,070	6,009	6,009	5,646	5,787	3,652
# of top-bead	3,736	2,923	3066	3,210	3,183	3,520	3,361
# of bottom-bead	3,509	3,387	3,502	3,756	3,631	4,058	3,650
Porosity[1]	54.5 %	55 %	54 %	54.3 %	55.1 %	55.9 %	56.8 %

[1]Porosity is the average porosity in the region where beads are located.
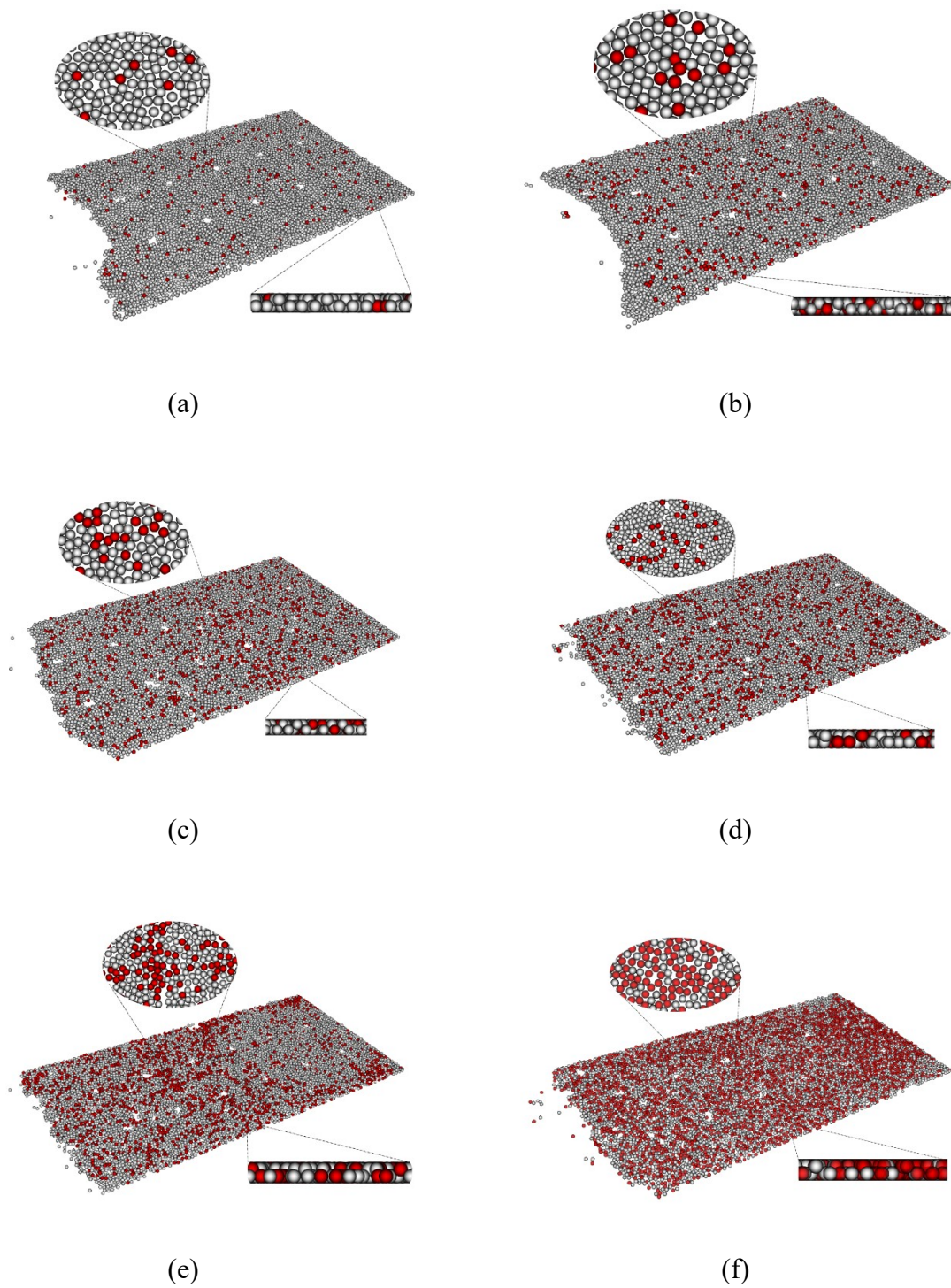
Figure 6-3: Electrostatically heterogeneous PMAs with positively charged beads: (a) 4%, (b) 9%, (c) 13%, (d) 17%, (e) 25%, and (f) 50%. Grey represents negatively charged beads and red represents positively charged beads.

6.3 Lattice Boltzmann simulation of fluid flow through bead-based microfluidic PMAs

The single-phase parallelized LB code used in the last chapter to obtain steady-state velocity fields was also applied here to simulate flows through digitalized PMAs. We assume that flow fields are not affected by surface charge heterogeneities (i.e. no electro kinetic flows). A constant body force was applied to drive the flow with periodic boundary condition along the flow direction. The LB simulation parameters are listed in Table 6-3 and velocity fields are visualized in Figure 6-4 (homogenous PMA) and Figure 6-5 (heterogeneous PMAs). These visualizations also include divisions of computational domains into high-velocity (above 300% of the average velocity) and low-velocity regions (lower 50% of the average velocity) to highlight potential preferential flow paths and stagnant zones in the PMAs.

Table 6-3: Parameters of LB simulations of the microfluidics experiments

Parameter	0%	4%	9%
Grid type	Cartesian	Cartesian	Cartesian
Grid size	$602 \times 17 \times 1981$	$602 \times 17 \times 1981$	$602 \times 17 \times 1981$
Total number of voxels	20,273,554	20,273,554	20,273,554
Total number of fluid voxels	11,048,552	114,022,55	11,402,255
Body force	$[0\ 0\ 10^{-6}]$	$[0\ 0\ 10^{-6}]$	$[0\ 0\ 10^{-6}]$
Collision operator	MRT	MRT	MRT
Relaxation time	1.0	1.0	1.0
Boundary condition	Periodic	Periodic	Periodic
Total time step	10,000	10,000	10,000
Number of cores used	128	128	128

Continued from Table 6-3

13%	17%	25%	50%
Cartesian	Cartesian	Cartesian	Cartesian
$602 \times 17 \times 1981$	$602 \times 17 \times 1981$	$602 \times 17 \times 1981$	$602 \times 17 \times 1981$
20,273,554	20,273,554	20,273,554	20,273,554
11,192,910	11,048,552	11,402,255	11,402,255
MRT	MRT	MRT	MRT
1.0	1.0	1.0	1.0
$[0\ 0\ 10^{-6}]$	$[0\ 0\ 10^{-6}]$	$[0\ 0\ 10^{-6}]$	$[0\ 0\ 10^{-6}]$
Periodic	Periodic	Periodic	Periodic
10,000	10,000	10,000	10,000
128	128	128	128
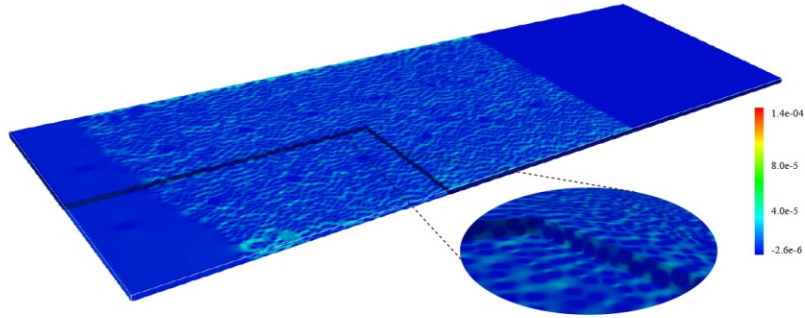
(a)
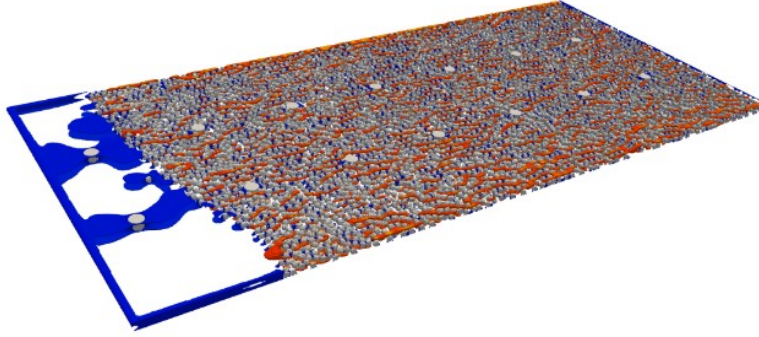
(b)
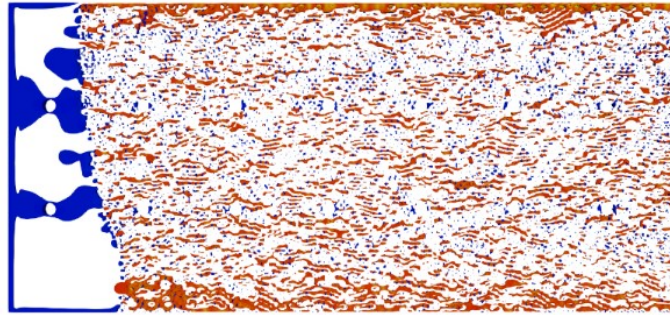
(c)

Figure 6-4: Velocity field from LB simulation (on slice $y = 11$). Domain is that of the electrostatically homogeneous PMA: (a) Distribution of velocity component in the mean-flow direction over the entire PMA; (b) 3D view of high-velocity region (above 300% of the average velocity: orange) and low-velocity region (below 50% of the average velocity: blue) with beads (grey); (c) 2D top view of (b) with no beads visualized.
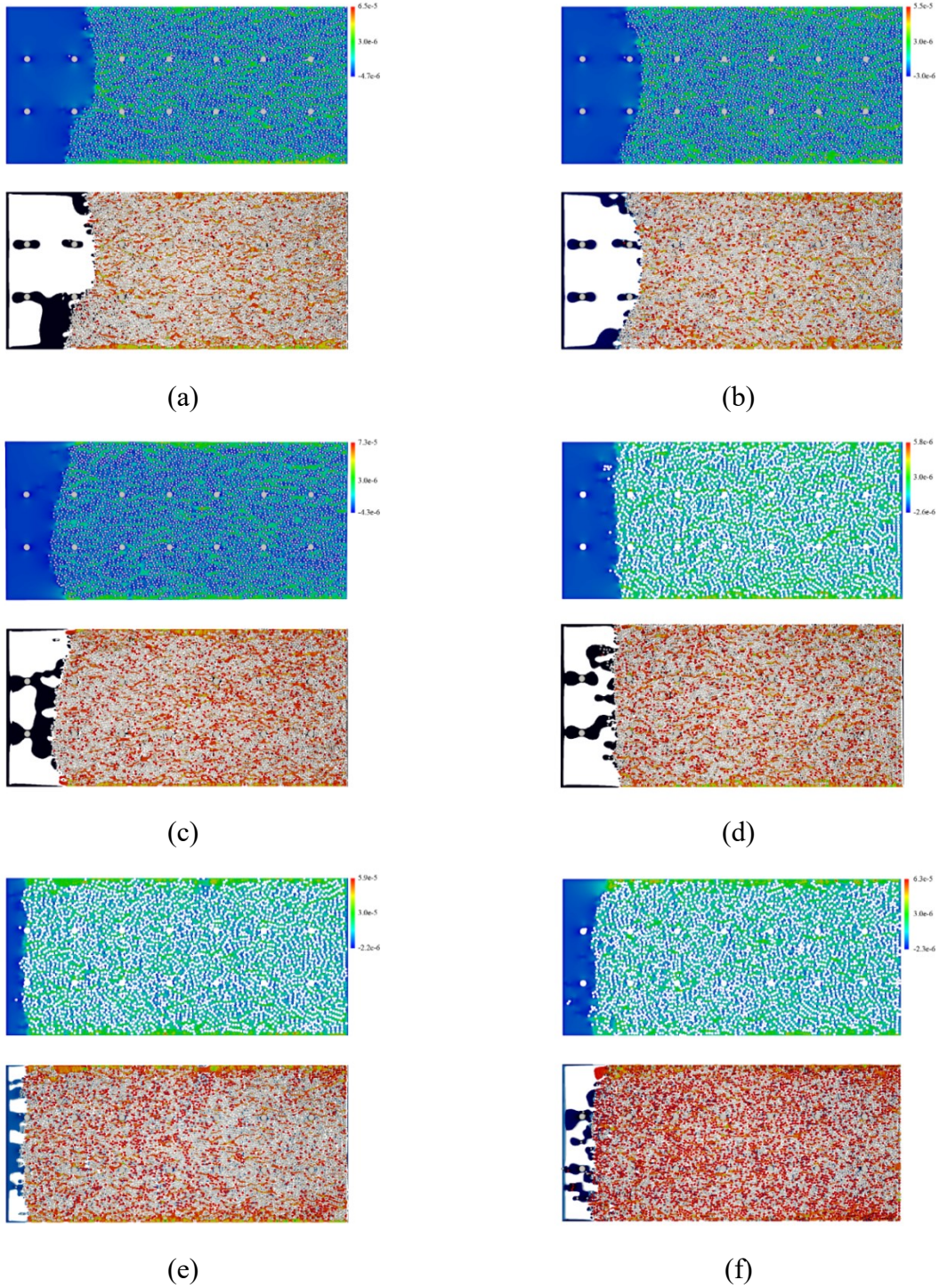
Figure 6-5: Velocity field from LB simulation (on slice $y = 11$). Domain is that of the electrostatically heterogeneous PMA: distribution of velocity component in the mean-flow direction over the entire PMA and 2D top view of high-velocity region (above 300% of the average velocity: orange) and low-velocity region (below 50% of the average velocity: blue) with beads (grey) for (a) 4%, (b) 9%, (c) 13%, (d) 17%, (e) 25%, and (f) 50%.

6.4 RWPT simulation of colloid transport in electrostatically homogeneous PMA

The random walk particle tracking (RWPT) code presented in the last chapter for solute transport was used to solve advection-diffusion of colloids through the PMAs. In RWPT, the steady-state velocity fields obtained from LB simulations were used to determine the advective displacements of colloids. Diffusive displacements by random motions were added to locate the final positions of colloidal particles (Eq. 4-4). The random motions in RWPT are isotropic. No flux boundary condition was implemented in RWPT using the specular reflection method. Colloids were modeled as non-aggregative volumeless point tracers with no tracer-to-tracer interactions considered.

The electrostatically homogeneous experiment free of colloid deposition was first investigated. The molecular diffusion coefficient of colloid used in the experiment is $D_m = 8.58 \times 10^{-13}$ m^2/s. The dimensionless molecular diffusion coefficient of RWPT was chosen to match the Péclet number of the experiment. To faithfully simulate microfluidic experiments, the first step is to ensure that colloid concentration measured at the inlet is reproduced in the simulation. Due to variations in the injection condition, the concentration of colloids at the inlet was not a constant in the experiment (Figure 6-6). The injection concentration rapidly built up in about three pore volumes (PV) and leveled off at approximately 8-10 PV. At 38 PV, injection of colloids stopped and the concentration of colloids declined from 38 to 48 PV. To account for this experimental detail, RWPT code was modified so that it can use the actual inlet concentration profiles from the experiments.

(a)   (b)
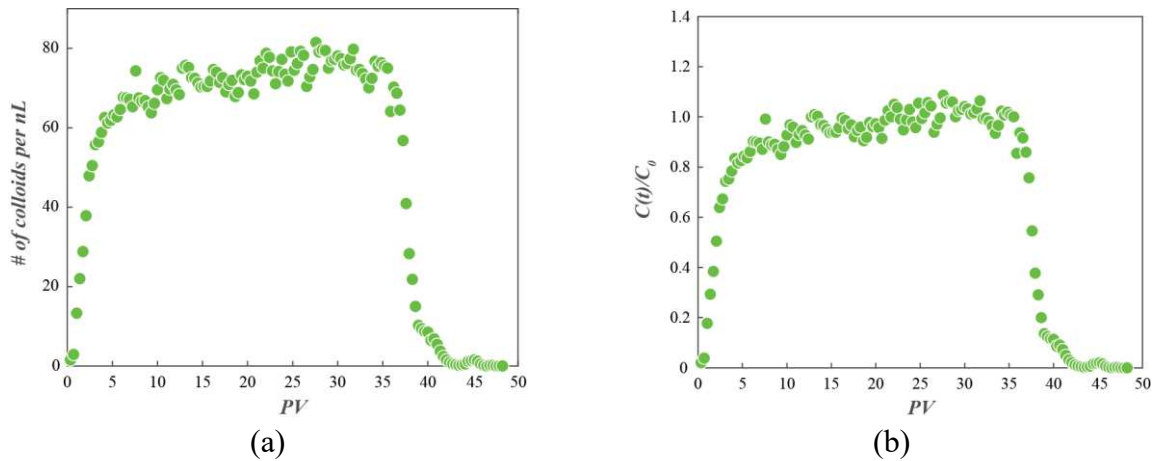
Figure 6-6: (a) Variation in the inlet concentration of colloids with time; (b) Inlet concentration normalized by the average steady-state concentration.

Logistics growth curves were used to fit the actual inlet concentration profile. Constants in Eq. 6-1 were determined so that the logistic curves matches the early time build-up (a_1, b_1, c_1, d_1 and e_1) and late time elution (a_2, b_2, c_2, d_2 and e_2) of the actual inlet concentration profile (Table 6-4). In RWPT, a random number is generated when a tracer's pseudo-position enters the inlet region (0 to 100 in z direction) at a given pore volume (t_R). This random number is compared with probability P in Eq. 6-1. If the random number is greater than P, this tracer is tagged so that it will not be counted in the construction of breakthrough curves.

$$P(t_R) = \frac{c_1}{1 + a_1 e^{-b_1(t_R - e_1)}} - d_1$$

$$P(t_R) = \frac{c_2}{1 + a_2 e^{-b_2(t_R - e_2)}} - d_2$$

(6-1)

Table 6-4: Constants in logistics growth curves to match the inlet concentration profile

Constants	0%	4%	9%	13%	17%	25%	50%
a_1	2.40	12.00	2.60	12.00	2.60	2.60	2.60
b_1	0.75	0.85	0.60	1.22	0.60	0.85	1.10
c_1	1.44	1.11	1.56	1.16	1.50	1.50	1.50
d_1	0.48	0.11	0.52	0.13	0.50	0.50	0.50
e_1	0.00	0.00	0.00	0.00	0.00	0.00	0.00
a_2	7.00	12.00	8.00	13.00	1.10	1.00	0.80
b_2	1.30	0.80	1.00	1.10	1.00	2.50	1.60
c_2	1.44	1.11	1.04	1.16	1.00	1.00	1.50
d_2	0.33	0.11	0.00	0.13	0.00	0.00	0.00
e_2	40.00	44.50	44.00	41.50	38.50	34.00	34.40

Figure 6-7a shows the comparison between the mathematical model and the actual normalized inlet concentration profile for the electrostatically homogeneous PMA. Figure 6-7b shows the comparison between the simulated inlet concentration profile and the actual normalized inlet concentration profile. Both the mathematical model and the simulated inlet concentration profile are in good agreement with the actual profile.
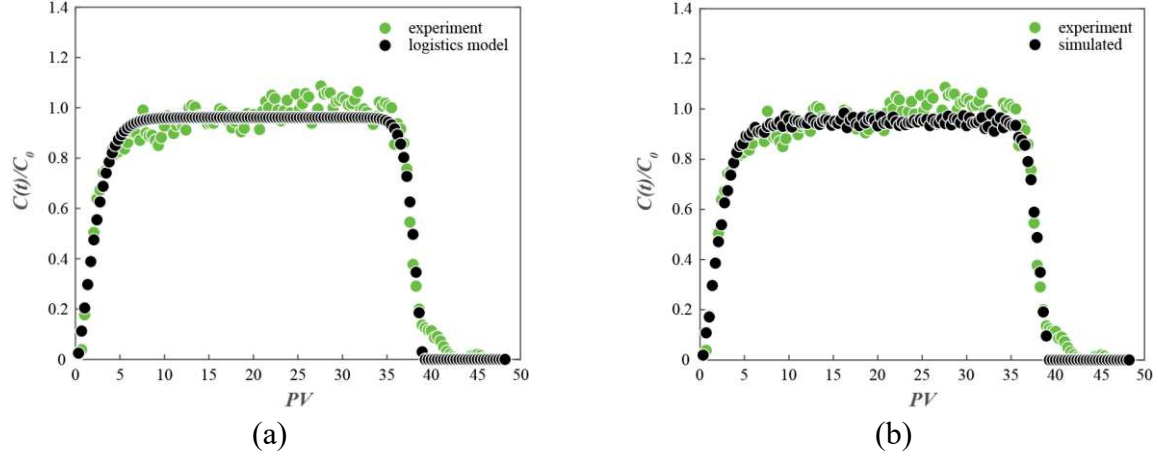
Figure 6-7: The inlet concentration of logistics model (a) and simulated inlet concentration (b).

With controlled inlet concentration profile, RWPT successfully generated a breakthrough curve that is in good agreement with that of the electrostatically homogeneous experiment (Figure 6-8a). The simulated breakthrough curve with no inlet control is also presented for comparison (Figure 6-8b). As previously discussed, this comparison at the level of breakthrough curves, confirms that our pore-scale simulations of advection-diffusion of colloids under the given Péclet number successfully reproduced macroscopic advection-dispersion. This comparison additionally confirms that the appeared retardation in the experimental breakthrough curve stemmed mainly from the relaxed inlet concentration of the experiment rather than equilibrium partitioning as discussed in Chapter 2.
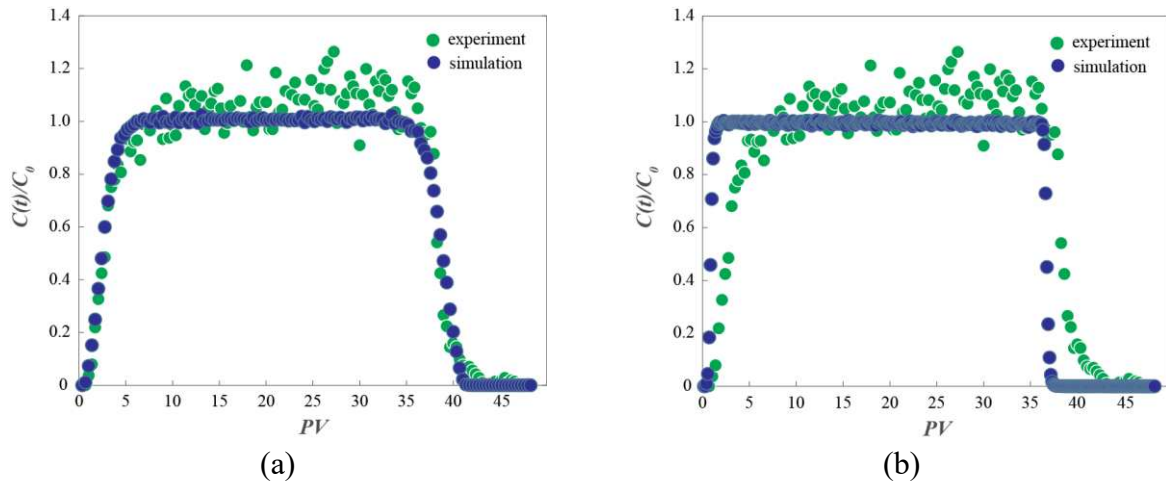
Figure 6-8: Comparison of the BTCs between the experiment and simulations. (a) With controlled inlet concentration; (b) with a constant inlet concentration.

6.5 Random walk particle tracking (RWPT) simulation of the micro-colloidal flow in chemically heterogeneous bead-based microfluidic sediment analogues

Transport and deposition of colloids through electrostatically heterogeneous microfluidic PMAs were then investigated. The heterogeneous PMAs contained a certain percentage of positively charged beads and therefore can retain colloids by electrostatic attraction force. Electrostatic adsorption of colloids is typically irreversible while that of solutes is reversible (Johnson et al. 1996). Observations from microfluidics experiments supported that adsorption occurred in an irreversible manner that led to irreversible deposition of colloids on the surface of positively charged beads, or collector beads.

Irreversible deposition due to electrostatic attraction between colloids and positively charged surfaces was modeled in RWPT by letting tracers attach permanently to solid voxels of positively charged beads when the distance between tracers and solid voxels becomes less than a prescribed "interaction length". When adsorption takes place, the location of adsorption is recorded. Like in solute transport simulations, upon an adsorption event a pseudo tracer is released to ensure that at the boundary of the periodic domain the flux of tracers is maintained (Figure 6-9).
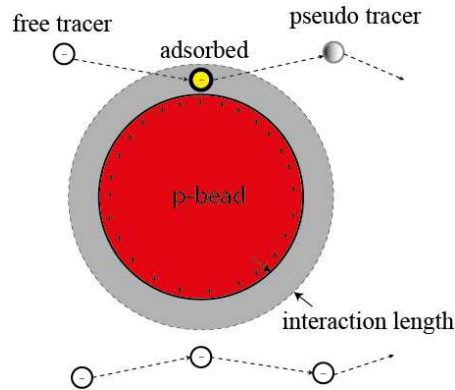
Figure 6-9: Illustration of a tracer falling into the interaction length (grey) of a positively charged bead (p-bead). Adsorption is recorded, and a pseudo tracer keeps moving to the exit.

Pseudo tracers are not intercepted by positively charged beads and they are not counted in breakthrough curves. Once a pseudo tracer passes through the exit of the periodic domain, the probability of turning it back into a real tracer is determined by Eq. 6-1 to meet the need to reproduce realistic inlet concentration profile. We assumed that the repulsive electrostatic

interaction between negatively charged beads and colloids led to negligible adsorption of colloids on negatively charged beads based on observations made in the experiments. Collisions between tracers and negatively charged surfaces therefore were modeled by the specular reflection.

The electrostatic interaction length was evaluated by comparing the attractive potential energy between a colloidal particle and the surface of a bead and the thermal energy of the colloid particle. It was assumed that a colloidal particle is retained on the surface of a bead if the attractive potential energy is ten times of the thermal energy. Through personal communication with collaborator who conducted the experiment, the electrostatic interaction range of 500 nm was used and its calculation procedure is given as follows,

First, the Debye length for low potentials is given (Israelachvili 2011),

$$\kappa^{-1} = \left(\frac{\varepsilon_0 \varepsilon k_B T}{\sum \rho_i e^2 z_i^2} \right)^{1/2} \tag{6-2}$$

In the experiments, H_2CO_3 was formed by the dissolved carbon dioxide (CO_2), the pH measurement of DI water gave the concentration of H^+. If we assume that H_2CO_3 was completely dissociated, then we obtained the following parameters for Debye length calculation (Table 6-5). Then the Debye length was calculated at 63 nm.

Table 6-5: Values for calculating the Debye length

Parameter	Value	Unit
Vacuum permittivity	8.85×10^{-12}	Fm^{-1}
Relative permittivity of water at 20 °C	0.75	-
Boltzmann constant	1.38×10^{-23}	JK^{-1}
Room temperature	298	K
pH	5.8	-
Concentration of H+	1.58×10^{-5}	mole/L
Concentration of CO_3^{2-}	7.90×10^{-6}	mole/L

Sader et al. (1995) derived an analytic solution for the double layer interaction between two dissimilar spheres (Eq. 6-3).

$$V = \frac{\varepsilon}{4} \left(\frac{k_B T}{e} \right)^2 \frac{a_1 a_2}{R_c} \left[(y_1 + y_2)^2 \ln\left(1 + e^{-\kappa h}\right) + (y_1 - y_2)^2 \ln\left(1 - e^{-\kappa h}\right) \right] \tag{6-3}$$

V is the interaction free energy between dissimilar spheres, *e* is the proton charge, R_c is the center distance between two spheres, *h* is the surface distance between two spheres, *a* and *y* are the radius and the reduced surface potential of each sphere, respectively. The reduced surface potentials were approximated by using the measured zeta potentials. We assumed that irreversible adsorption occurs when the interaction free energy is greater than ten times the thermal energy ($V > 10k_BT$), and then the surface-to-surface separation length was calculated at 273 nm. The radius of a colloidal particle was considered, and the interaction range then became 520 nm.

We note that exact kinetics of adsorption is an area of active research because interactions of various time and length scales are involved. Detailed mechanistic models should include hydrodynamic and Brownian forces, gravity, and complete DLVO (Derjaguin, Landau, Verwey, and Overbeek) forces (Deraguin and Landau 1941; Verwey and Overbeek 1948). In our calculations, we only focused on electrostatic attraction. It has a longer range compared to the van der Waals force, and therefore is the first attractive force that a colloid sees when it approaches the surface of a positively charged bead.

The dynamics pertaining to colloid deposition also involves variable kinetics that can be attributed to blocking of surfaces. At the early stage when most of the reactive surfaces are not occupied, the rate of adsorption is at its maximum. As retained colloids gradually cover the reactive surfaces, the rate of deposition generally decreases. However, under certain conditions the rate may increase if the layer of retained colloids on the surface interacts favorably with free colloids approaching the surface and speed up the rate of deposition (Johnson and Elimelech 1995). In the literature, this effect has been named as "surface coverage effect" or "blocking effect" (Johnson and Elimelech 1995). This effect of surface blocking is usually modeled by introducing either a linear or a non-linear dynamic blocking function (Privman et al. 1991; Song and Elimelech 1992). A linear Langmurian dynamic blocking function assumes a linear dependence between rates and available surfaces while a non-linear dynamic blocking function uses a power law function.

The surface coverage or blocking effect was also observed in our experiments. In order to account for this effect in RWPT simulations, the maximum number of colloids that can attach to a single positively charged bead was determined by continuously flowing colloid suspensions through the PMAs. The average number of colloids collected per bead was counted to be 82 (N_{bead}). The ratio of the number of tracers in RWPT to the number of colloidal particles was determined

by comparing the number of colloids injected in the experiments with the number of tracers released in our RWPT simulations. The ratio is approximately 150, which means 150 tracers in RWPT are statistically equivalent to one colloidal particle in the experiment. Therefore, the capacity of a single voxel on the surface of a positively charged bead can be estimated by dividing the number of colloids that is equivalent to 82 colloids by the surface area of the bead (Eq. 6-4).

$$n_{node} = N_{bead} \times \frac{\text{colloid-to-tracer ratio}}{\text{surface area of bead}} = 40 \tag{6-4}$$

After establishing the capacity of a single voxel on the surface of a positively charged bead (n_{node}), in RWPT we let the probability of adsorption decrease linearly or nonlinearly from one to zero with increasing number of retained tracers, following the linear and nonlinear Langmuir adsorption models described below.

The linear Langmuir adsorption model follows,

$$B(\theta) = 1 - \beta\theta \tag{6-5}$$

, where $B(\theta)$ is the surface blocking parameter, θ is the surface coverage, and $\beta = 1/\theta_{max}$ is the excluded area parameter. Using the average maximum number of colloids collected in the experiment ($N_{bead} = 82$) per bead, the excluded area parameter is,

$$\theta_{max} = 82 \times \frac{\pi a}{4\pi R^2} = 0.051 \tag{6-6}$$

R and a are the radii of a collector bead and a colloidal particle, respectively, in micrometer.

Then, the linear Langmuir adsorption model yields,

$$B(\theta) = 1 - 19.5 \times \theta \tag{6-7}$$

To implement this into RWPT, the Langmuir adsorption model is recast in terms of the maximum number of tracers allowed on a single voxel on the surface of a positively charged bead ($n_{node} = 40$). The probability of adsorption (P) of a single voxel on the surface of a positively charged beads is thus expressed as a function of the number of tracers that the node has collected (n). The probability of adsorption (P) becomes zero when a voxel has collected its maximum number of tracers (n_{node}).

$$P(n) = 1 - 1/40 \times n \qquad (6\text{-}8)$$

Similarly, the non-linear random sequence adsorption (RSA) model was obtained through the following procedure.

Adamczyk and Belouschek (1991) presented the RSA model with the inclusion of an effective particle radius that were give,

$$a^* = 1 + H^*$$
$$H^* = h^* / a \qquad (6\text{-}9)$$

where H^* is a dimensionless length that characterizes the electrostatic repulsion of particles deposited on the surfaces.

The surface blocking parameter was expressed as a function of surface coverage θ (Eq. 6-10).

$$B(\theta) = 1 - c_1\theta + c_2\theta^2 + c_3\theta^3 \qquad (6\text{-}10)$$

The coefficients are obtained using Eq. 6-11.

$$c_1 = 4\left(\frac{1+H^*}{1+A}\right)^2, \; c_2 = \frac{6\sqrt{3}}{\pi}\left(\frac{1+H^*}{1+A}\right)^4, \; c_3 = 1.407\left(\frac{1+H^*}{1+A}\right)^6$$
$$H^* = h^* / a = \frac{1}{\kappa a}\ln\zeta - \frac{1}{\kappa a}\ln\left(1 + \frac{1}{2\kappa a}\ln\zeta\right) \qquad (6\text{-}11)$$
$$\zeta = 8\gamma\frac{k_B Ta}{10e^2}\tanh\left(\frac{e\psi_p}{4k_B T}\right)$$

A is the ratio of the radius of a colloidal particle to the radius of a collector bead, ψ_p is the surface potential of the particle, and γ is a constant that accounts for lateral particle interaction. Typical values of γ ranges from 0.25 to 0.5. For this calculation, γ (0.25) and θ_{max} (0.051), and H^* (2.2) was used to obtain the following RSA model,

$$B(\theta) = 1 - 37.2\theta + 285.5\theta^2 + 1127.3\theta^3 \qquad (6\text{-}12)$$

In the same way, the voxel-based probability of adsorption is,

$$P(n) = 1 - 4.65 \times 10^{-2} n + 4.460938 \times 10^{-4} n^2 + 2.201758 \times 10^{-4} n^3 \qquad (6\text{-}13)$$

The shapes of the linear Langmuir adsorption model and the non-linear RSA model as well as those of the corresponding voxel-based probability models for RWPT are presented in Figure 6-10.
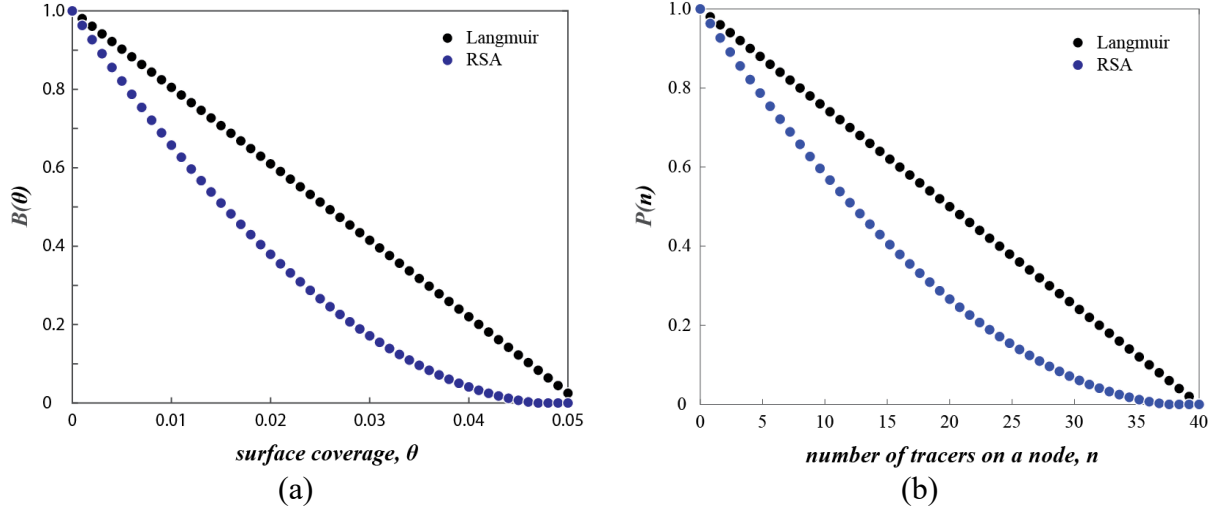
Figure 6-10: (a) Linear Langmuir adsorption and non-linear RSA models; (b) the corresponding probability models.

6.6 Breakthrough curves of electrostatically heterogeneous PMAs

Using controlled inlet concentration profiles of experiments and incorporating the interaction length and the surface coverage effect, RWPT simulations were performed for all heterogeneous PMAs. The parameters of RWPT simulations are summarized in Table 6-6.

Table 6-6: Parameters of RWPT simulations of the microfluidics experiments

Parameter	0%	4%	9%
Grid type	Cartesian	Cartesian	Cartesian
Domain size	$602 \times 17 \times 1981$	$602 \times 17 \times 1981$	$602 \times 17 \times 1981$
Total number of grids	20,273,554	20,273,554	20,273,554
Total number of fluid nodes	11,048,552	114,022,55	11,402,255
Total number of tracers	54,997	58,210	54,997
Average velocity	4.46456×10^{-6}	5.19594×10^{-6}	4.71715×10^{-6}
Maximum velocity	1.40242×10^{-4}	6.53804×10^{-5}	5.68874×10^{-5}
Diffusion coefficient	3.92023×10^{-8}	4.56244×10^{-8}	4.142026×10^{-8}
Time step size	3.36466×10^{3}	6.67901×10^{3}	8.005230×10^{3}
Total time step	140×24782	140×11773	140×11261
Number of cores used	128	128	128

Table 6-6 Continued

13%	17%	25%	50%
Cartesian	Cartesian	Cartesian	Cartesian
602 × 17 × 1981	602 × 17 × 1981	602 × 17 × 1981	602 × 17 × 1981
20,273,554	20,273,554	20,273,554	20,273,554
11,192,910	11,048,552	114,022,55	11,402,255
55,717	56,346	54,493	55,871
4.834690×10^{-6}	4.93270×10^{-6}	4.65152×10^{-6}	5.28837×10^{-6}
7.266740×10^{-5}	6.00841×10^{-5}	5.94276×10^{-5}	6.38512×10^{-5}
4.245235×10^{-8}	4.33130×10^{-8}	4.08440×10^{-8}	4.64360×10^{-8}
6.338310×10^{3}	7.58285×10^{3}	7.68342×10^{3}	7.13255×10^{3}
140 × 12543	140 × 10375	140 × 9263	140 × 9082
128	128	128	128

The simulated breakthrough curves relative to those of the experiments are presented in Figure 6-11. Breakthrough curves from RWPT simulations are in very good agreement with those from experiments. Taking the PMA that contains 4% positively charged beads for example, the normalized effluent concentration builds up till about seven pore volumes (PV), and then the rate of increase in the effluent concentration slows down, showing a distinctively lower slope from 7 PV on. The initial build-up is typical of advection-dispersion in porous media with irreversible adsorption. Colloids traveling near the positively charged beads are removed / filtered (Eq. 2-16 and Eq. 2-17). The effluent concentration stabilizes at about 40% at 7 PV. Past 7 PV, the concentration increases at a slower rate because the surfaces of positively charged beads are gradually covered by retained colloids. As the surfaces available for adsorption slowly deplete, more colloids can reach the exit, leading to increased effluent concentration. Note that there is only a subtle difference between the linear Langmurian blocking function and the non-linear RSA model. This indicates that the specific form of surface blocking tested in this study does not have a significant impact under the given flow and transport conditions. At 38 PV, the concentration drops as the injection of colloids is stopped.

Figure 6-11 shows that our RWPT simulations implemented with 1) inlet concentration variation, 2) interaction length for electrostatic adsorption, and 3) blocking functions for surface coverage effect, have successfully predicted the early-time build-up (0 to 7 PV), the slow rise in the effluent concentration due to surface blocking (7 PV to 38 PV), and the final elusion (38 PV to 52 PV). These comparisons successfully validated our modeling approaches. They also confirm on the level of breakthrough curves that the dominant mechanisms that controlled advection-

dispersion and electrostatic adsorption of colloids in heterogeneous PMAs are irreversible kinetic adsorption combined with surface blocking.
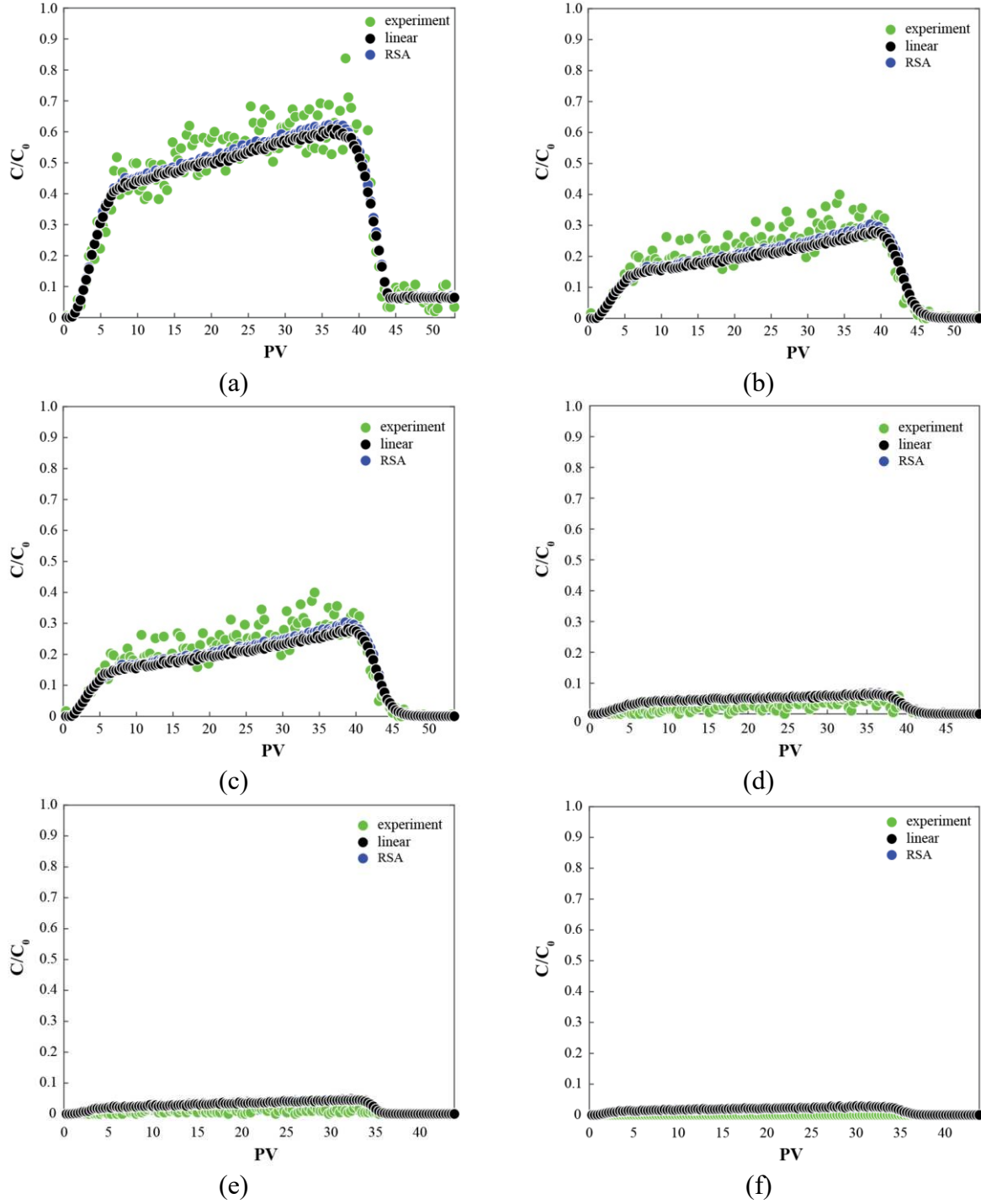
Figure 6-11: The breakthrough curves of electrostatically heterogeneous PMAs with 4% (a), 9% (b), 13% (c), 17% (d) 25% (e), and 50% (f) of positively charged bead: the interaction length = 0.5 and the nodal adsorption capacity n = 40.

For PMAs with high percentages of positively charged beads (17, 25, and 50%), the effluent concentration profiles predicted by RWPT simulations were slightly higher than those of the experiments. There may be several reasons: 1) it was observed in the experiments that some colloids were trapped near negatively charged beads, probably due to finite size of colloid particles as some pore spaces were not large enough due to geometric configurations and some colloidal particles could be trapped. Since colloidal particles are modeled as volumeless point particles in our RWPT, retention due to finite size cannot be captured. 2) The accuracy of image processing tends to become less accurate along the edges of the PMAs. If the space along the upper and lower edges of the PMAs were overestimated in the simulations, preferential flow paths that are not present in the experiments would develop in the simulations. Then, tracers would pass through those spaces easily without encountering positively charged beads, leading to higher effluent concentrations.

In sum, our RWPT simulations successfully reproduced breakthrough curves of colloids in both electrostatically homogeneous and electrostatically heterogeneous microfluidics PMAs. The case of electrostatically homogeneous PMA confirms that our pore-scale modeling approach is applicable to colloid transport, which has a much higher Péclet number than solute transport studied in Chapter 5. Cases of electrostatically heterogeneous PMAs show that our pore-scale modeling approaches have correctly captured the interactions between colloids and surfaces including irreversible kinetic adsorption and surface blocking / exclusion. These validations should pave way for many potential applications.

CHAPTER 7

ANISOTROPIC RANDOM WALK

As a solute or colloidal particle approaches the surface of the solid phase, its diffusive movement is hindered by the hydrodynamic force exerted by the fluid between them, i.e., lubrication effect. As a result, the movement of colloids under the effect of the lubrication interaction is hindered in the normal and tangential direction. In this study, we focus on the effect of hindered diffusion due to lubrication effect on breakthrough curves.

7.1 Microscale interactions between a spherical colloidal particle and a flat surface

Although the above probability model, in principle, can simulate the equilibrium between the sorbed solutes / colloids and those in solution, the kinetics of sorption depends on the detail of colloid-surface interactions such as electrostatic, van der Waals, and lubrication, and thus, they need to be considered. As a small colloidal particle approaches the surface, the diffusive movement of colloids is significantly affected by such surface induced interactions, and therefore, the diffusion tensor (D_o) in Eq. (4-2) needs to be modified to incorporate the consequences of such interactions.

A small sphere carried by advection in unbound fluid is subject to hydrodynamic drag. The hydrodynamic force balances the internal forces as inertia is negligible at the micro-scale (Kim and Karilla 2013). The motion of a small spherical particle immersed in a Newtonian viscous liquid follows Stokes' law (Eq. 7-1).

$$m\frac{du}{dt} = -3\pi\mu du = -6\pi\mu au \tag{7-1}$$

, where m is mass of a sphere, u is velocity of the sphere, μ is viscosity of the fluid, d and a are diameter and radius of the sphere, respectively. Eq. 7-1 can be rearranged to estimate the relaxation time τ.

$$m = \rho V = \frac{4}{3}\pi\rho r^3 = \frac{1}{6}\pi\rho d^3$$
$$\frac{du}{dt} = -\frac{18\mu}{\rho d^2}u \tag{7-2}$$

67

If the relaxation time τ is smaller than the time interval of flow simulation, there is no need to consider the equation of motion for colloids and then the motion of colloids can be treated as purely diffusive. Under this diffusive condition, using Stokes-Einstein equation, relaxation time (τ), Brownian diffusivity (D_B), Brownian velocity (u_B) and Brownian force (F_B) of colloid in water at 20 °C are estimated using typical values for colloids in water (Eq. 7-3).

$$\tau = \frac{\rho d^2}{18\mu} = \frac{(2.5 \times 10^3 \text{kg/m}^3)(10^{-6}\text{m})^2}{18(10^{-3}\text{kg/m}\cdot\text{s})} = 1.4 \times 10^{-7}\text{s}$$

$$D = \frac{k_B T}{3\pi\mu d} = \frac{(1.38 \times 10^{-23}\text{J/°K})(293°\text{K})}{3\pi(10^{-3}\text{kg/m}\cdot\text{s})(10^{-6}\text{m})} = 4.3 \times 10^{-13}\text{m}^2/\text{s} \qquad (7\text{-}3)$$

$$u_B = \sqrt{\frac{2k_B T}{m}} = \sqrt{\frac{2k_B T}{\frac{1}{6}\rho\pi d^3}} = 2.48 \times 10^{-3}\text{m}^2/\text{s}$$

$$F_B = 3\pi\mu d u_B = 2.40 \times 10^{-11}\text{kg}\cdot\text{m/s}^2$$

The estimated magnitude of the Brownian force can be used to evaluate the influence of colloid-surface forces on the motion of colloids. The range of interaction of a specific colloid-surface force can be estimated as the distance where the magnitude of this force becomes comparable to that of the Brownian force. The lubrication force F_{Lub} (Eq. 7-4) on a sphere that approaches a flat and homogeneous surface with velocity u_B is governed by Eq. 7-3. When this force is balanced by the Brownian force F_B, the separation distance h is given by (Eq. 7-5) (Figure 7-1).

$$F_{Lub} = 6\pi\mu a \frac{a}{h} u_B \qquad (7\text{-}4)$$

$$h = \frac{6\pi\mu a^2 u_B}{6\pi\mu a u_B} = a = \frac{d}{2} \qquad (7\text{-}5)$$
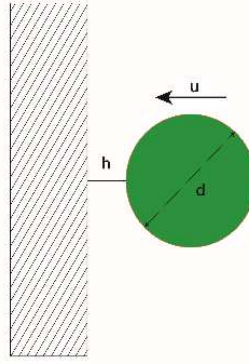
Figure 7-1: Illustration of a colloidal particle under the effect of lubrication interaction.

Therefore, lubrication force begins to hinder the motion of a colloid normal and tangential to the solid surface, as the colloid approaches the solid surface within half of its diameter ($h = d/2$). Because the magnitude of lubrication force acting along the normal and tangential to the surface is not identical, an important consequence of the lubrication force near solid surface is that the diffusive movement of colloids is no longer isotropic. In this region, it turns from isotropic to anisotropic random walk due to the tangential and lateral hindrance. Depending on colloid size and fluid viscosity, lubrication causes a colloid particle that diffuses in an isotropic fashion in every direction (i.e., isotropic random walk) to turn to an anisotropic random walk as it enters the region that lubrication interactions prevail. The governing stochastic equation of RWPT should be modified to implement anisotropic random walk within the range of lubrication interaction.

7.2 Analytic solutions for a particle nearing a wall in a viscous liquid

Stokes' law has been widely used to estimate the resistance of a sphere traveling through a viscous liquid (Brenner 1961). However, the Stokes' law was originally derived on the premise that there is no bounding walls around in the fluid. Most engineering problems involve a sphere moving in fluid bounded by walls. As such, the movement of a particle bounded by a flat wall vertically or laterally was first studied theoretically (Brenner 1961; Goldman et al. 1967; Kim and Karilla 2013) and verified experimentally (Banerjee and Kihm 2005) and now the theory on near-wall hindered Brownian motion has been established. Now it is well known that hindered diffusion substantially deviates from the original Stokes' law (De Corato al. 2015).

Brenner (1961) derived an exact solution of mobility for sphere moving through a viscous fluid perpendicular to a flat solid plane. The original Stokes' law (Eq. 7-1) was modified by a

correction factor λ in Eq. 7-6 to account for normal hindrance. Brenner (1961) presented an infinite sum of a function of the radius of sphere, a, and the separation distance or surface-to-surface distance between a sphere and a solid surface, h (Eq. 7-7). Bevan and Prieve (2000) simplified the infinite sum based on regression and presented a simple algebraic from (Eq. 7-8). Following this line of work, (Goldman et al. 1967) derived a correction term for mobility parallel to a surface (Eq. 7-9). The mobility correction terms, normal to a surface as well as tangential to a surface, are a function of the radius of a sphere (a) and the surface-to-surface distance between a sphere and a solid surface (h).

$$F = 6\pi\mu a U \lambda \tag{7-6}$$

$$\lambda_{\perp} = \frac{4}{3}\sinh\alpha \sum_{n=1}^{\infty} \frac{n(n+1)}{(2n-1)(2n+3)}\left[\frac{2\sinh(2n+1)\alpha+(2n+1)\sinh 2\alpha}{4\sinh^2(n+0.5)\alpha-(2n+1)^2\sinh^2 2\alpha}-1\right]$$

$$\alpha = \cosh^{-1}\left(\frac{h}{a}\right) = \ln\left\{\frac{h}{a}+\sqrt{\left(\frac{h}{a}\right)^2-1}\right\} \tag{7-7}$$

$$\lambda_{\perp} = \frac{6h^2+2ah}{6h^2+9ah+2a^2} \tag{7-8}$$

$$\lambda_{\parallel} = \left[1-\frac{9}{16}\left(\frac{a}{a+h}\right)+\frac{1}{8}\left(\frac{a}{a+h}\right)^3-\frac{45}{256}\left(\frac{a}{a+h}\right)^4-\frac{1}{16}\left(\frac{a}{a+h}\right)^5\right] \tag{7-9}$$

The Brownian diffusivity tensor of the original Stokes' law is replaced by the near-wall hindered diffusion tensor ($\mathbf{D}^H$) (Choi et al. 2007)(Eq. 7-10).

$$\mathbf{D}^H = \frac{kT}{6\pi\mu a}\mathbf{M}^H = \frac{kT}{6\pi\mu a}\begin{bmatrix} M_{\perp} & 0 & 0 \\ 0 & M_{\parallel} & 0 \\ 0 & 0 & M_{\parallel} \end{bmatrix} = \frac{kT}{6\pi\mu a}\begin{bmatrix} \lambda_{\perp}^{-1} & 0 & 0 \\ 0 & \lambda_{\parallel}^{-1} & 0 \\ 0 & 0 & \lambda_{\parallel}^{-1} \end{bmatrix} \tag{7-10}$$

The inverse of the normal and tangential correction terms for a particle with 0.5 µm diameter are plotted as a function of separation distance (h) (Figure 7-2).
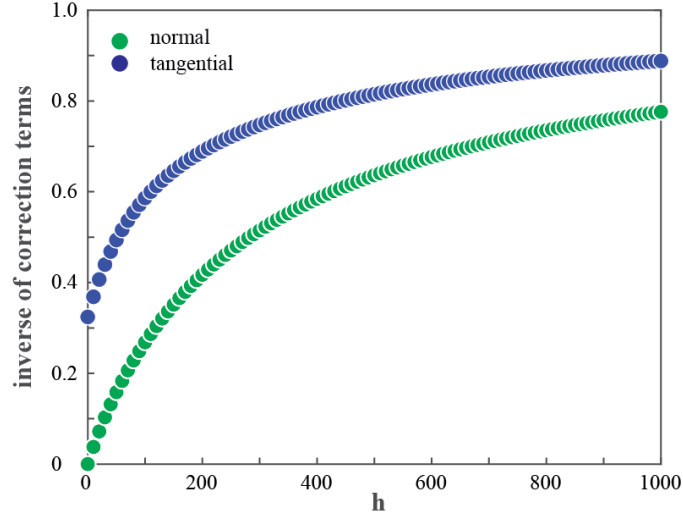
Figure 7-2: Correction factors for normal and tangential hindrance.

7.3 Numerical study of anisotropic random walk

In this study, we focus on the influence of hydrodynamic lubrication effect. The diameter of a colloidal particle and the grid resolution are assumed to be 0.5 μm and 1 μm /pixel, respectively. Then the separation length of lubrication interaction (h) is 250 nm. A colloid moving isotopically enters the region ($h < 250$ nm), undergoes normal and lateral hindrance and turns to anisotropic random walk. Moving closer to the surface, a colloidal particle is either attached to the surface or reflected against the surface, depending on each depositional scenario, i.e., favorable or unfavorable condition. The separation distance of hydrodynamics lubrication for 0.5 μm particle illustrated in Figure 7-3.
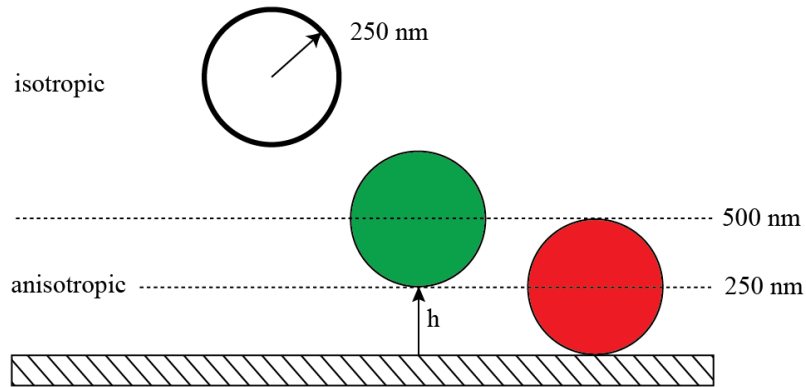
Figure 7-3: Illustration of separation distances of lubrication interaction for 0.5 μm particle.

The normal and lateral hindrance of lubrication effect restrain the diffusive movement resulting in anisotropic random walk (Figure 7-4).
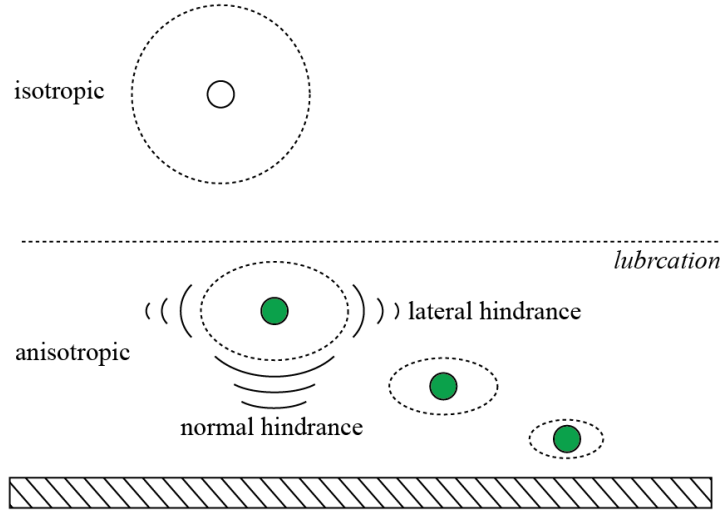
Figure 7-4: Illustration of hindered diffusive movement near a homogeneous flat wall by normal and lateral hindrance (the dotted line represents the magnitude of diffusive motion).

In our RWPT, a sub-routine checks if the current position of a trace is in the range of the lubrication interaction, and then, the isotropic diffusivity tensor (D_o) in the isotropic random walk (Eq. 4-4) is replaced by the hindered Brownian diffusivity tensor D^H (Eq. 7-10) to account for normal and lateral hindrance, respectively (Eq. 7-11). If we assume that a colloidal particle approaching a wall normal to x-direction, Eq. 7-11 is expressed in a scalar form (Eq. 7-12). When a tracer in RWPT is located within half of the radius of a particle ($h < 0$), each minimum correction factors in normal and tangential direction is applied.

$$\boldsymbol{x}(t+\Delta t) = \boldsymbol{x}(t) + \boldsymbol{v}(\boldsymbol{x}(t))\Delta t + \sqrt{2\boldsymbol{D}^H \Delta t}\,\boldsymbol{\xi} \tag{7-11}$$

$$x(t+\Delta t) = x(t) + v_x(x(t))\Delta t + \sqrt{2D_{\perp}^H \Delta t}\,\xi$$
$$y(t+\Delta t) = y(t) + v_y(y(t))\Delta t + \sqrt{2D_{\parallel}^H \Delta t}\,\xi \tag{7-12}$$
$$z(t+\Delta t) = z(t) + v_z(z(t))\Delta t + \sqrt{2D_{\parallel}^H \Delta t}\,\xi$$

A three dimensional body-centered cubic (BCC) porous medium was generated to see the microscopic effect of lubrication on breakthrough curves. The voxels of the sphere located at the center were assigned to two for adsorption, and other were one for reflection. This configuration can be interpreted that tracers propagate under repulsive interaction with negatively charged spheres and attractive interaction with a positively charged sphere. As previously discussed, the simulation time step must be small enough so that the motion of a colloidal particle under the lubrication effect should be purely diffusive. In addition, the maximum displacement in RWPT (Eq. 4-5) was adjusted to be small enough to resolve the separation length of the lubrication effect, and the maximum displacement in RWPT was set to one tenth of the separation length. A Dirac-delta type input was used by initializing 500 tracers per node at the first layer of the domain. The tracers that have passed the left side of the domain were removed. Total 4,050 tracers were initialized to suppress statistical nose in breakthrough curves. In an attempt to quantify the effect of hindered diffusion on breakthrough curves, four different simulations were performed, CASE 1: isotropic random walk using a non-adsorbing tracer, CASE 2: anisotropic random walk using a non-adsorbing tracer, CASE 3: isotropic random walk using an adsorbing tracer, and CASE 4: anisotropic random walk using an adsorbing tracer. In CASE 1 and CASE 2, tracers move being reflected on the wall. In CASE 3 and CASE 4, tracers are removed from the domain when adsorbed by the collector sphere at the center. The simulation parameters of each case are summarized in Table 7-1. The LB velocity field is given in Figure 7-5.

Table 7-1: Parameters of RWPT simulations for hindered diffusion

Parameter	CASE 1	CASE 2	CASE 3	CASE 4
Domain size	$15 \times 15 \times 65$	$15 \times 15 \times 65$	$15 \times 15 \times 65$	$15 \times 15 \times 65$
Total number of grids	14,625	14,625	14,625	14,625
Total number of fluid nodes	3930	3930	3930	3930
Total number of tracers	40,500	40,500	40,500	40,500
Tracer interaction	non-adsorbing	non-adsorbing	adsorbing	adsorbing
Near wall diffusion	isotropic	anisotropic	isotropic	anisotropic
Number of BT tracers	40,498	40,444	14,753	22,883
Average velocity	2.4292×10^{-7}	2.4292×10^{-7}	2.4292×10^{-7}	2.4292×10^{-7}
Maximum velocity	2.1247×10^{-6}	2.1247×10^{-6}	2.1247×10^{-6}	2.1247×10^{-6}
Diffusion coefficient	6.0×10^{-8}	6.0×10^{-9}	6.0×10^{-9}	6.0×10^{-9}
RWPT time step size	4.53×10^{3}	4.53×10^{3}	4.53×10^{3}	4.53×10^{3}
Total time step (3PV)	6.0×10^{4}	6.0×10^{4}	6.0×10^{4}	6.0×10^{4}
# of CPUs	16	16	16	16
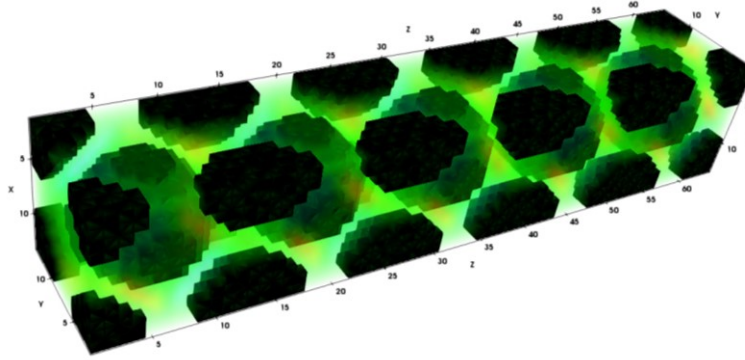
Figure 7-5: LB velocity field in the BCC domain.

Figure 7-6 shows the breakthrough curves using an impulse input for all the cases. For a non-adsorbing tracer, tracers are advected and diffused either in an isotropic or in an anisotropic fashion when they are within the prescribed range of lubrication interaction around a positively charged sphere. The breakthrough curves of isotropic and anisotropic random walk are compared in Figure 7-6b. This comparison shows that isotropic random walk exhibits a higher peak value in the relative concentration curve than anisotropic random walk. The anisotropic random walk also shows slightly more retardation in the build-up portion of the breakthrough curve and a longer tailing than the isotropic random walk. The comparison indicates that the hydrodynamic lubrication effect under a repulsion-dominant depositional scenario may result in retardation. This is because the lubrication layer near the surface of spheres acted like a stagnant pocket, making harder and longer for tracers escape the region with hindered diffusion. As opposed to this, anisotropic random walk in the presence of attractive collectors can facilitate transport. Figure 7-6c shows the comparison in breakthrough curves between isotropic and anisotropic random walk for an adsorbing tracer. The anisotropic random walk showed a higher peak than the isotropic random walk in relative concentration, and so were the total numbers of tracers recovered: 14,753 for isotropic random walk (CASE 3) and 22,883 for anisotropic random walk (CASE 4). It is clear that anisotropic random walk hindered the deposition of tracers on the surface of the collector sphere, making more tracers achieve breakthrough events at the exit. This indicates that anisotropic random walk under favorable condition can facilitate earlier breakthrough. Therefore, it is clear that hindered diffusion near the surface of solid phase can have an impact on breakthrough curves.

This set of numerical tests suggest that the lubrication effect can either retard or facilitate transport depending on depositional conditions.
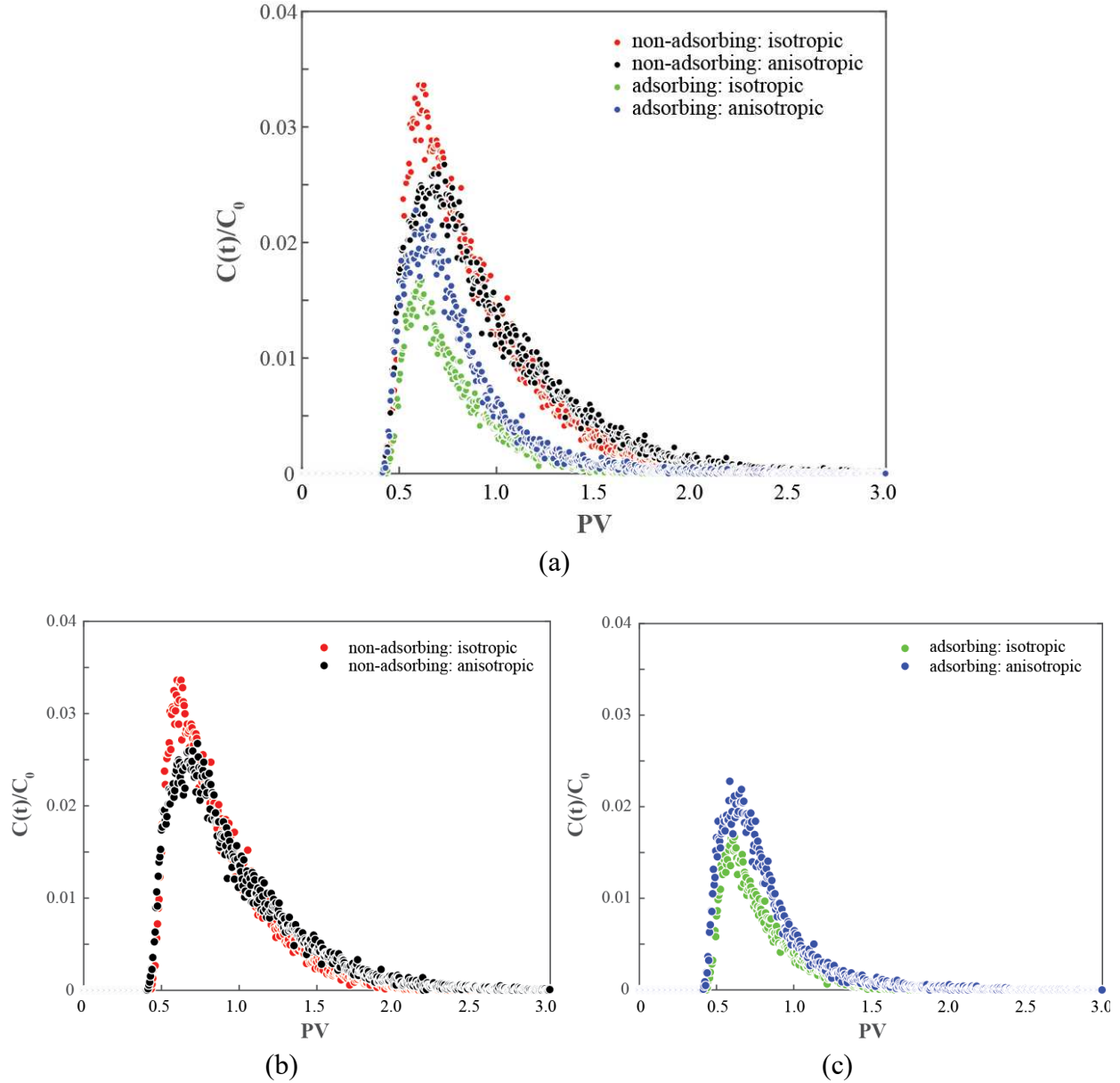
Figure 7-6: Breakthrough curves of non-adsorbing and adsorbing tracers with isotropic and anisotropic random walk (a). The breakthrough curves are separately presented for (b) a non-adsorbing tracer with isotropic (red) and anisotropic (black) random walk, and for (c) an adsorbing tracer with isotropic (green) and anisotropic (blue) random walk.

CHAPTER 8

CONCLUSIONS AND RECOMMENDATIONS FOR FUTURE WORK

Many research efforts have been made to capture fundamental aspects of flow and transport in porous media. Pore-scale numerical simulations are one of the research areas that have contributed greatly to our ability to investigate and understand complex flow and transport phenomena in porous media. In line with those works, in this study we developed pore-scale numerical models as an integral part of a comprehensive study encompassing column-scale and micro-scale experiments. We applied our models to solute transport in a bead-packed column and colloid transport in a bead-based microfluidics porous media analogue. Using pore-scale simulations enabled by parallel computing, the effects of pore-scale mechanisms on a macroscale observable quantity, the breakthrough curves, were successfully characterized. The predictions of our models were validated by direct comparisons with the experiments. The benefit of using a breakthrough-level comparison is that, unlike specific up-scaled properties such as permeability and dispersion coefficients that often rely on assumptions that may or may not be valid on the level of a representative element volume, breakthrough curve is the manifestation of all different levels of transport mechanisms in a phenomenologically observable form. Even though generating breakthrough curves using a large collection of particles over a laboratory scale porous medium replica is computationally expensive, we have successfully achieved this with efficient parallel computing strategies and robust reflection algorithms. Recalling the primary objectives of this dissertation, we directly simulated flow and convective transport of conservative and non-conservative solutes and colloids, and the predictions of our pore-scale simulations agreed well with experimental data, which confirms our predictive modeling approaches were successfully validated.

Summarized discussions on selected tasks and recommendations for future work are presented in the following sections before closing this dissertation.

8.1 Reconstruction of porous media replica for pore-scale simulations

In this dissertation, computational domains of a bead-packed column experiment and a microfluidics porous media analogue experiment were generated. For the column experiment, customized routines were developed to process CT-scanned images of glass beads in the column.

Totally, 2,000 images were processed. To reduce uncertainty, images were processed iteratively to match the bulk porosity of the actual column. For a bead-packed column with a length of 10.26 cm and a diameter of 0.75 cm, 50 million grids with 10 million fluid voxels were reconstructed and the resolution was 51.3 μm/pixel. One glass bead (500~600 μm) was therefore resolved by about 11 voxels.

For microfluidics experiments, a customized code reconstructed the computational domains of microfluidics experiments based on the center coordinates and radius of beads to differentiate the solid and liquid phases. The physical size of the PMA is $600 \times 15 \times 1891$ in micrometers. The PMAs were digitally reconstructed at the resolution of 1 μm/pixel, resulting in 20 million grids with 11 million fluid voxels. As such a bead with a diameter of 10 μm was resolved by 10 voxels. To simulate heterogeneities in the charge possessed by surfaces, solid voxels were tagged with values of one, two, or three depending on whether they belong to negatively charged beads, positively charged beads, or walls and pillars of the PMA, respectively. One was assigned to negatively charged beads (repulsive – specular reflection), two to positively charged beads (attractive – irreversible adsorption), and three to the wall and pillars (repulsive – specular reflection; different from one for visualization purpose). Totally, seven digitalized PMAs were reconstructed including one homogeneous and six heterogeneous cases.

8.2 Improvements in efficiency and robustness of algorithms to generate breakthrough curves

Generating breakthrough curves directly from RWPT requires significant computational times. To complete simulation tasks within a reasonable amount of time, message passing interface (MPI) was used to parallelize LB and RWPT codes. In addition, a more robust algorithm of specular reflection for no-flux boundary condition at solid- liquid interface was implemented in RWPT. The new algorithm correctly accounts for all cases of reflections. The updated RWPT code can be stably run to the time steps required for completion of our simulation tasks.

8.3 Pore-scale simulations of a conservative solute and colloid

Our pore-scale framework using LB and RWPT was applied to two experimental systems for solute and colloid transport, respectively. For both systems, agreements with experiments were achieved without using any fitting parameters.

For a non-adsorbing solute (I^-) in the column experiment, our pore-scale simulations recovered breakthrough curves comparable to the experiment. The experimental data showed some delay (retardation) in the build-up part. With the limited data from the experiment (only one point available in this region), it is not easy to identify what factors contributed to this. Our data, however, are in better agreement with the analytical solution of 1D advection-dispersion equation (ADE) than with the experimental data. The solution of 1D-ADE used longitudinal dispersion coefficients from the empirical correlation of Perkins and Johnston (1963). When examined closely, our simulation data exhibited a little more dispersion than the 1D-ADE solution and a little less dispersion than the experimental data. Additionally, tortuosity, and longitudinal dispersion coefficient obtained from pore-scale simulations were good agreement with those from empirical correlations.

For the simulation of colloid transport in electrostatically homogeneous microfluidics experiment with repulsive interactions between colloids and beads, initial simulations using a step function as the inlet concentration profile did not achieve good agreement with the experiment, because the inlet concentration profile in the experiment was not an ideal step function. RWPT was coded to implement the actual inlet concentration profile, and then the simulated breakthrough curve was in good agreement with the experimental data.

8.4 Equilibrium partitioning, irreversible kinetic deposition, and surface coverage effect

For transport of solutes with equilibrium partitioning and that of colloids with irreversible deposition kinetics and surface coverage effects, these pore-scale physio-chemical mechanisms were implemented into our RWPT.

For simulations of column experiments, equilibrium adsorption-desorption process was implemented using a probability of adsorption and a probability of desorption. We simulated the laboratory batch experiment used to establish equilibrium partition of solute between the fluid and the solid surface, and obtained probabilities of adsorption and desorption that reproduced the partitioning coefficient of Cs^+ measured in laboratory batch experiments. Note that in the absence of kinetic (rate) data, there are many pairs of probabilities that can recover the same partitioning coefficient, provided that they have the same ratio of probability of adsorption to that of desorption. Different sets of probabilities of adsorption and desorption that have the same ratio were tested and they produced different shape of breakthrough curves. This indicates that the 1D-ADE

78

breakthrough curves that depend on a single value of the partitioning coefficient from batch experiment is limited. Using these probability values in RWPT generated a breakthrough curve for the adsorbing solute (Cs^+) that is in reasonable agreement with that from the column experiment. With limited number of experimental data points available, it is not easy to make more rigorous comparisons. Nevertheless, a comparison with the solution of 1D-ADE was also made. RWPT simulation predicted a more dispersive breakthrough curve than 1D-ADE in that the initial breakthrough time from RWPT simulation was earlier.

For simulations of microfluidics experiments, kinetic deposition processes and surface coverage effects were implemented. The interaction length between a colloidal particle and a positively charged surface was calculated using an analytic solution and 500 nm was used. To model the surface coverage effect both linear and non-linear dynamic blocking functions were applied. RWPT simulations with the inclusion of these effects successfully recovered the breakthrough curves of the experiments. This comparison at the level of breakthrough curves confirms that the pore-scale mechanisms that control the characteristics of observable transport in the experiments were the irreversible deposition of colloids combined with finite adsorptive capacity of collectors, the positively charged beads.

8.5 Effect of hydrodynamic interaction with surfaces on advection-diffusion of colloids

The diffusive movement of a colloidal particle is hindered due to lubrication effect as it nears the surface of solid phase. The hindered diffusion due to lubrication interaction, different in the directions normal to and tangential to the surface, can have an impact on breakthrough and retention. We simulated the effect of anisotropic random walk of colloids near surfaces under the influence of hydrodynamic lubrication interaction on the breakthrough curve in a small-scale porous medium model. Two analytic solutions that address the lateral hindrance and the tangential hindrance were used to model anisotropic random walk within a prescribed separation distance in which the effect of hydrodynamic lubrication interaction begins to affect the isotropy of Brownian motion. Considering the length and time scales of such interactions, a small domain with 10 beads arranged in an in-line, body-centered cubic configuration, with a single collector sphere at its center was used with a pulse-type input. Our simulations generated breakthrough curves of 1) a non-adsorbing tracer with isotropic random walk, 2) a non-adsorbing tracer with anisotropic random walk, 3) an adsorbing tracer with isotropic random walk, and 4) an adsorbing tracer with

anisotropic random walk. The results show that anisotropic random walk can either facilitate, or surprisingly, hinder transport of tracers depending on depositional conditions. For a non-adsorbing tracer, anisotropic random walk due to the lubrication interaction hindered transport because tracers migrate into zones of low Brownian diffusivity near solid surfaces where they are practically stagnant. For an adsorbing tracer, anisotropic random walk facilitates transport because it lowered the rate at which tracers approach the adsorbing surface. These results suggest that near-wall hindered diffusion can play a significant role in breakthrough and deposition.

8.6 Recommendations for future work

The framework of pore-scale numerical simulations using LB and RWPT has advanced to the level that not only REV-scale macroscopic properties such as permeability, tortuosity, and dispersion tensor, but also breakthrough curves of entire (small-scale) experiments can be directly obtained. With opportunities to insert fundamental physics, pore-scale simulations provide us not only theoretically more profound understating of flow and transport in porous medium but also practical tools to connect the pore-scale mechanisms to macroscopic scale observable traits of transport. Based on my experience in this area of research, I would recommend, in this regard, the following directions for future research efforts,

- Develop advanced image processing algorithms to extend the work flow proposed in this dissertation to more complex natural systems of porous media such as natural rocks including shale.
- Develop efficient parallelized visualization environments that can be used for digital reconstruction of large-sized computational domains and visualization of trajectories of a large collection of particles over such domains. They would provide a great deal of insights on understating of complex phenomena as visualization is not just a fancy representation of simulations.
- Develop a more efficient parallelized RWPT that can implement both periodic and constant injection boundary conditions. For a pulse type injection, Open Multi-Processing (OpenMP) can be combined efficiently with MPI.
- Incorporate a finite-sized particle model in RWPT. Even though the finite size effect is somewhat implicitly considered in Brownian diffusivity term in RWPT, an explicit

modeling of a finite-sized tracer would help us to understand the size exclusion effect for large-size colloids that should have a considerable impact on breakthrough and deposition.

- Develop a new modeling approach incorporating the complete DLVO interactions in RWPT. Currently, simulations incorporating the effect of lubrication interactions are forced to run with very small time steps to meet the requirement to resolve the thin lubrication range (250 nm). The ranges of DLVO interactions are even smaller, and hence the requirement on time step size would be more demanding. If DLVO interactions can be implemented such that simulations tasks can be performed in a practically reasonable amount of time, it could pave a way to solving many unanswered problems on transport of macromolecules, colloids, bacteria and virus, as well as colloid-facilitated transport of radionuclides.

REFERENCES CITED

Abu-Ashour, J., Joy, D.M., Lee, H., Whiteley, H.R. and Zelin, S. 1994. Transport of microorganisms through soil. *Water, Air, and Soil Pollution* **75**(1-2): 141-158. https://doi.org/10.1007/BF01100406.

Ackerer, P. 1988. Random-walk method to simulate pollutant transport in alluvial aquifers or fractured rocks. In *Groundwater flow and quality modelling,* ed. Custodio E., Gurgui A. and Ferreira J.P.L. 475-486. Dordrecht: Springer. https://doi.org/10.1007/978-94-009-2889-3_27.

Adamczyk, Z. and Belouschek, P. 1991. Localized adsorption of particles on spherical and cylindrical interfaces. *Journal of Colloid and Interface Science* **146**(1): 123-136. https://doi.org/10.1016/0021-9797(91)90010-6.

Arns, J.Y., Sheppard, A.P., Arns, C.H., Knackstedt, M.A., Yelkhovsky, A. and Pinczewski, W.V. 2007. Pore-level validation of representative pore networks obtained from micro-ct images. *Proc.,* International Symposium of the Society of Core Analysts*,* Calgary, Canada, 10-12 September 2007, 1-12.

Aslan, E., Taymaz, I. and Benim, A.C. 2014. Investigation of the lattice Boltzmann SRT and MRT stability for lid driven cavity flow. *International Journal of Materials, Mechanics and Manufacturing* **2**(4): 317-324. https://doi.org/10.7763/IJMMM.2014.V2.149.

ASTM C1733-10, *Standard Test Method for Distribution Coefficients of Inorganic Species by the Batch Method*. 2010. West Conshohken, PA: ASTM International.

Banerjee, A. and Kihm, K.D. 2005. Experimental verification of near-wall hindered diffusion for the Brownian motion of nanoparticles using evanescent wave microscopy. *Physical Review E* **72**(4): 042101. https://doi.org/10.1103/PhysRevE.72.042101.

Batu, V. 2005. *Applied flow and solute transport modeling in aquifers: fundamental principles and analytical and numerical methods*. Boca Raton, Florida: CRC Press.

Bear, J. 1961. On the tensor form of dispersion in porous media. *Journal of Geophysical Research* **66**(4): 1185-1197. https://doi.org/10.1029/JZ066i004p01185.

Bear, J. 1972. *Dynamics of fluids in porous media*. New York: American Elsevier Publishing Company.

Bear, J. and Cheng, A.H.D. 2010. *Modeling groundwater flow and contaminant transport,* 2010 edition*.* Dordrecht: Springer. https://doi.org/10.1007/978-1-4020-6682-5.

Bevan, M.A. and Prieve, D.C. 2000. Hindered diffusion of colloidal particles very near to a wall: Revisited. *The Journal of Chemical Physics* **113**(3): 1228-1236.

https://doi.org/10.1063/1.481900.

Bhatnagar, P.L., Gross, E.P. and Krook, M. 1954. A model for collision processes in gases. I. Small amplitude processes in charged and neutral one-component systems. *Physical Review* **94**(3): 511. https://doi.org/10.1103/PhysRev.94.511.

Boek, E.S. and Venturoli, M. 2010. Lattice-Boltzmann studies of fluid flow in porous media with realistic rock geometries. *Computers and Mathematics with Applications* **59**(7): 2305-2314. http://dx.doi.org/10.1016/j.camwa.2009.08.063.

Boudreau, B.P. 1996. The diffusive tortuosity of fine-grained unlithified sediments. *Geochimica et Cosmochimica Acta* **60**(16): 3139-3142. https://doi.org/10.1016/0016-7037(96)00158-5.

Brenner, H. 1961. The slow motion of a sphere through a viscous fluid towards a plane surface. *Chemical Engineering Science* **16**(3-4): 242-251. https://doi.org/10.1016/0009-2509(61)80035-3.

Cameron, D.R. and Klute, A. 1977. Convective-dispersive solute transport with a combined equilibrium and kinetic adsorption model. *Water Resources Research* **13**(1): 183-188. https://doi.org/10.1029/WR013i001p00183.

Chen, S., Wang, Z., Shan, X. and Doolen, G.D. 1992. Lattice Boltzmann computational fluid dynamics in three dimensions. *Journal of Statistical Physics* **68**(3-4): 379-400. https://doi.org/10.1007/BF01341754.

Choi, C.K., Margraves, C.H. and Kihm, K.D. 2007. Examination of near-wall hindered Brownian diffusion of nanoparticles: Experimental comparison to theories by Brenner (1961) and Goldman et al. (1967). *Physics of Fluids* **19**(10): 103305. https://doi.org/10.1063/1.2798811.

Comiti, J. and Renaud, M. 1989. A new model for determining mean structure parameters of fixed beds from pressure drop measurements: application to beds packed with parallelepipedal particles. *Chemical Engineering Science* **44**(7): 1539-1545. https://doi.org/10.1016/0009-2509(89)80031-4

De Corato, M., Greco, F., D'Avino, G. and Maffettone, P.L. 2015. Hydrodynamics and Brownian motions of a spheroid near a rigid wall. *The Journal of Chemical Physics* **142**(19): 194901. https://doi.org/10.1063/1.4920981.

Deraguin, B.V. and Landau, L. 1941. Theory of the stability of strongly charged lyophobic sols and of the adhesion of strongly charged particles in solution of electrolytes. *Acta Physicochim* **14**: 633-662.

d'Humieres, D. 1994. Generalized lattice-Boltzmann equations. *Progress in Astronautics and Aeromatics* **159**: 450-458. https://doi.org/10.2514/5.9781600866319.0450.0458.

d'Humieres, D., Ginzburg, I., Krafczyk, M., Lallemand, P. and Luo, L.S. 2002. Multiple-Relaxation-Time Lattice Boltzmann Models in 3D. *Philosopical Transactions of the Royal Society of London. Series A: Mathematical, Physical and Engineering Sciences* **360**(1792): 437–451.

Dullien, F.A.L. 1975. Prediction of "tortuosity factors" from pore structure data. *AIChE Journal* **21**(4): 820-822. https://doi.org/10.1002/aic.690210431.

Einstein, A. 1905. Über die von der molekularkinetischen Theorie der Wärme geforderte Bewegung von in ruhenden Flüssigkeiten suspendierten Teilchen. *Annalen der Physik* **322**(8): 549-560. https://doi.org/10.1002/andp.19053220806.

Fetter, C. W. 2008. *Contaminant Hydrogeology*, second edition. Long Grove, IL: Waveland Press.

Flury, M., Mathison, J.B. and Harsh, J.B. 2002. In situ mobilization of colloids and transport of cesium in Hanford sediments. *Environmental Science and Technology* **36**(24): 5335-5341. https://doi.org/10.1021/es025638k.

Friedman, A.M. and Kennedy, J.W. 1955. The Self-Diffusion Coefficients of Potassium, Cesium, Iodide and Chloride Ions in Aqueous Solutions. *Journal of the American Chemical Society* **77**(17): 4499-4501. https://doi.org/10.1021/ja01622a016.

Gillham, R.W. and Cherry, J.A. 1983. Predictability of solute transport in diffusion-controlled hydrogeologic regimes. *Proc*., Symposium on Low Level Waste Disposal: Facility Design, Construction and Operating Practices, Nuclear Regulatory Commission, Washington, D.C., 29-30 September 1982, 379-410.

Ginzbourg, I. and Adler, P.M. 1994. Boundary flow condition analysis for the three-dimensional lattice Boltzmann model. *Journal de Physique II* **4**(2): 191-214. https://doi.org/https://doi.org/10.1051/jp2:1994123.

Goldman, A.J., Cox, R.G. and Brenner, H. 1967. Slow viscous motion of a sphere parallel to a plane wall—I Motion through a quiescent fluid. *Chemical Engineering Science* **22**(4): 637-651. https://doi.org/https://doi.org/10.1016/0009-2509(67)80047-2.

Guo, Y., Huang, J., Xiao, F., Yin, X., Chun, J., Um, W., Neeves, K.B. and Wu, N. 2016. Bead-based microfluidic sediment analogues: fabrication and colloid transport. *Langmuir* **32**(36): 9342-9350. https://doi.org/10.1021/acs.langmuir.6b02184.

Guo, Z., Zheng, C. and Shi, B. 2002. Discrete lattice effects on the forcing term in the lattice Boltzmann method. *Physical Review E* **65**(4): 046308. https://doi.org/10.1103/PhysRevE.65.046308.

He, X., Shan, X. and Doolen, G.D. 1998. Discrete Boltzmann equation model for nonideal gases. *Physical Review E* **57**(1): R13. https://doi.org/10.1103/PhysRevE.57.R13.

Hlushkou, D., Gritti, F., Daneyko, A., Guiochon, G. and Tallarek, U. 2013. How microscopic characteristics of the adsorption kinetics impact macroscale transport in chromatographic beds. *The Journal of Physical Chemistry C* **117**(44): 22974-22985. https://doi.org/10.1021/jp408362u.

Hlushkou, D., Gritti, F., Guiochon, G., Seidel-Morgenstern, A. and Tallarek, U. 2014. Effect of adsorption on solute dispersion: a microscopic stochastic approach. *Analytical Chemistry* **86**(9): 4463-4470. https://doi.org/10.1021/ac500309p.

Iassonov, P., Gebrenegus, T. and Tuller, M. 2009. Segmentation of X-ray computed tomography images of porous materials: A crucial step for characterization and quantitative analysis of pore structures. *Water Resources Research* **45**(9): 1-12. https://doi.org/10.1029/2009WR008087.

Icardi, M., Boccardo, G., Marchisio, D.L., Tosco, T. and Sethi, R. 2014. Pore-scale simulation of fluid flow and solute dispersion in three-dimensional porous media. *Physical Review E* **90**(1): 013032. https://doi.org/10.1103/PhysRevE.90.013032.

Israelachvili, J.N. 2011. *Intermolecular and surface forces*, third edition. Waltham, MA: Academic Press.

Jiménez-Hornero, F.J., Giráldez, J.V. and Laguna, A. 2005. Simulation of tracer dispersion in porous media using lattice Boltzmann and random walk models. *Vadose Zone Journal* **4**(2): 310-316. https://doi.org/10.2136/vzj2004.0090.

Johnson, P.R. and Elimelech, M. 1995. Dynamics of colloid deposition in porous media: Blocking based on random sequential adsorption. *Langmuir* **11**(3): 801-812. https://doi.org/10.1021/la00003a023

Johnson, P.R., Sun, N. and Elimelech, M. 1996. Colloid transport in geochemically heterogeneous porous media: Modeling and measurements. *Environmental Science and Technology* **30**(11): 3284-3293. https://doi.org/10.1021/es960053.

Kaiser, K. and Guggenberger, G. 2000. The role of DOM sorption to mineral surfaces in the preservation of organic matter in soils. *Organic Geochemistry* **31**(7-8): 711-725. https://doi.org/10.1016/S0146-6380(00)00046-2.

Khirevich, S. 2011. *High-Performance Computing of Flow, Diffusion, and Hydrodynamic Dispersion in Random Sphere Packings*. PhD Thesis, Philipps-Universität Marburg, Germany (2010). https://doi.org/10.17192/z2011.0057.

Kim, S. and Karrila, S.J. 2013. *Microhydrodynamics: principles and selected applications.* Butterworth-Heinemann, Newton, MA: Dover Publications. https://doi.org/10.1002/cite.330641004.

Kim, S.H. and Pitsch, H. 2007. A generalized periodic boundary condition for lattice Boltzmann

method simulation of a pressure driven flow in a periodic geometry. *Physics of Fluids* **19**(10): 108101. https://doi.org/10.1002/cite.330641004.

Koponen, A., Kataja, M. and Timonen, J. 1996. Tortuous flow in porous media. *Physical Review E* **54**(1): 406. https://doi.org/10.1103/PhysRevE.54.406

Kretzschmar, R., Barmettler, K., Grolimund, D., Yan, Y.D., Borkovec, M. and Sticher, H. 1997. Experimental determination of colloid deposition rates and collision efficiencies in natural porous media. *Water Resources Research* **33**(5): 1129-1137. https://doi.org/10.1029/97WR00298.

Krüger, T., Kusumaatmaja, H., Kuzmin, A., Shardt, O., Silva, G. and Viggen, E.M. 2017. *The Lattice Boltzmann Method: Principles and Practice*. Switzerland: Springer International Publishing. https://doi.org/10.1007/978-3-319-44649-3.

Kupershtokh, A.L. 2004, New method of incorporating a body force term into the lattice Boltzmann equation. *Proc.*, 5th International EHD Workshop, University of Poitiers, Poitiers, France, 30-31 August 2004, 241-246.

Ladd, A.J.C. and Verberg, R. 2001. Lattice-Boltzmann simulations of particle-fluid suspensions. *Journal of Statistical Physics* **104**(5-6): 1191-1251. https://doi.org/10.1023/A:1010414013942.

Lerman, A. 1979. *Geochemical processes. Water and sediment environments*. New York: John Wiley and Sons, Inc.

Lin, Q., Al-Khulaifi, Y., Blunt, M.J. and Bijeljic, B. 2016. Quantification of sub-resolution porosity in carbonate rocks by applying high-salinity contrast brine using X-ray microtomography differential imaging. *Advances in Water Resources* **96**: 306-322. https://doi.org/10.1016/j.advwatres.2016.08.002.

Lindquist, W., Lee, S., Coker, D. A., Jones, K. W. and Spanne, P. 1996. Medial axis analysis of three dimensional tomographic images of drill core samples. *Journal of Geophysical Research* **101**(B4): 8297–8310.

Liu, G., Zheng, C. and Gorelick, S.M. 2004. Limits of applicability of the advection-dispersion model in aquifers containing connected high-conductivity channels. *Water Resources Research* **40**(8): 1-19. https://doi.org/10.1029/2003WR002735.

Lowe, C.P. and Frenkel, D. 1996. Do hydrodynamic dispersion coefficients exist? *Physical Review Letters* **77**(22): 4552. https://doi.org/10.1103/PhysRevLett.77.4552.

Maier, R.S., Kroll, D.M., Bernard, R.S., Howington, S.E., Peters, J.F. and Davis, H.T. 2000. Pore-scale simulation of dispersion. *Physics of Fluids* **12**(8): 2065-2079. https://doi.org/10.1063/1.870452.

Mauret, E. and Renaud, M. 1997. Transport phenomena in multi-particle systems—I. Limits of applicability of capillary model in high voidage beds-application to fixed beds of fibers and fluidized beds of spheres. *Chemical Engineering Science* **52**(11): 1807-1817.

Molins, S., Trebotich, D., Steefel, C.I. and Shen, C. 2012. An investigation of the effect of pore scale flow on average geochemical reaction rates using direct numerical simulation. *Water Resources Research* **48**(3): 1-11. https://doi.org/10.1029/2011WR011404.

Molnar, I.L., Johnson, W.P., Gerhard, J.I., Willson, C.S. and O'Carroll, D.M. 2015. Predicting colloid transport through saturated porous media: A critical review. *Water Resources Research* **51**(9): 6804-6845. https://doi.org/10.1002/2015WR017318.

Newman, M.S. and Yin, X. 2013. Lattice Boltzmann simulation of non-Darcy flow in stochastically generated 2D porous media geometries. *SPE Journal* **18**(01): 12-26. SPE-146689-PA. https://doi.org/10.2118/146689-PA.

Ogata, A. and Banks, R.B. 1961. A solution of the differential equation of longitudinal dispersion in porous media: fluid movement in earth materials, USGS, 2 February 2012, https://pubs.er.usgs.gov/publication/pp411A (accessed 25 April 2018).

Otsu, N. 1979. A threshold selection method from gray-level histograms. *IEEE Transactions on Systems, Man, and Cybernetics* **9**(1): 62-66.

Park, C.H., Beyer, C., Bauer, S. and Kolditz, O. 2008. An efficient method of random walk particle tracking: accuracy and resolution. *Geosciences Journal* **12**(3): 285-297.

Perkins, T.K. and Johnston, O.C. 1963. A review of diffusion and dispersion in porous media. *Society of Petroleum Engineers Journal* **3**(01): 70-84, SPE-480-PA. https://doi.org/10.2118/480-PA.

Pham, N.H., Swatske, D.P., Harwell, J.H., Shiau, B.J. and Papavassiliou, D.V. 2014. Transport of nanoparticles and kinetics in packed beds: A numerical approach with lattice Boltzmann simulations and particle tracking. *International Journal of Heat and Mass Transfer* **72**: 319-328. https://doi.org/10.1016/j.ijheatmasstransfer.2013.12.075.

Privman, V., Frisch, H.L., Ryde, N. and Matijević, E. 1991. Particle adhesion in model systems. Part 13.—Theory of multilayer deposition. *Journal of the Chemical Society, Faraday Transactions* **87**(9): 1371-1375. https://doi.org /10.1039/FT9918701371.

Quigley, R.M., Yanful, E.K. and Fernandez, F. 1987. Ion transfer by diffusion through clayey barriers. *Geotechnical Practice for Waste Disposal Special Publication* **13**: 137-158.

Rhodes, M. E. 2008. *Transport in Heterogeneous Porous Media*. PhD thesis, Imperial College, London, UK (2008). https://doi.org/10.1088/0031-8949/1987/T19B/033.

Rhodes, M. E., Bijeljic, B. and Blunt, M.J. 2009. A rigorous pore-to-field-scale simulation method for single-phase flow based on continuous-time random walks. *SPE Journal* **14**(01): 88-94. SPE-106434-PA. https://doi.org/10.2118/106434-PA.

Robinson, R.A. and Stokes, R.H. 2002. *Electrolyte solutions*, second edition. Mineola, NY: Dover Publications.

Rod, K., Um, W., Chun, J., Wu, N., Yin, X., Wang, G. and Neeves, K. 2018. Effect of chemical and physical heterogeneities on colloid-facilitated cesium transport. *Journal of Contaminant Hydrology* **213**: 22-27. https://doi.org/10.1016/j.jconhyd.2018.03.012.

Sader, J.E., Carnie, S.L. and Chan, D.Y. 1995. Accurate analytic formulas for the double-layer interaction between spheres. *Journal of Colloid and Interface Science* **171**(1): 46-54. https://doi.org/10.1006/jcis.1995.1149.

Salles, J., Thovert, J.F., Delannay, R., Prevors, L., Auriault, J.L. and Adler, P.M. 1993. Taylor dispersion in porous media. Determination of the dispersion tensor. *Physics of Fluids A: Fluid Dynamics* **5**(10): 2348-2376. https://doi.org/10.1063/1.857309.

Sato, H., Yui, M. and Yoshikawa, H. 1996. Ionic diffusion coefficients of Cs^+, $Pb2^+$, $Sm3^+$, $Ni2^+$, $SeO2^{-4}$ and TcO^{-4} in free water determined from conductivity measurements. *Journal of Nuclear Science and Technology* **33**(12): 950-955. https://doi.org/10.1080/18811248.1996.9732037.

Scheibe, T.D., Perkins, W.A., Richmond, M.C., McKinley, M.I., Romero-Gomez, P.D., Oostrom, M., Wietsma, T.W., Serkowski, J.A. and Zachara, J.M. 2015. Pore-scale and multiscale numerical simulation of flow and transport in a laboratory-scale column. *Water Resources Research* **51**(2): 1023-1035. https://doi.org/https://doi.org/10.1002/2014WR015959

Shan, X. and Chen, H. 1993. Lattice Boltzmann model for simulating flows with multiple phases and components. *Physical Review E* **47**(3): 1815. https://doi.org/10.1103/PhysRevE.47.1815.

Song, L. and Elimelech, M. 1992. Deposition of Brownian particles in porous media: Modified boundary conditions for the sphere-in-cell model. *Journal of Colloid and Interface Science* **153**(1): 294-297. https://doi.org/10.1016/0021-9797(92)90321-C.

Succi, S. 2001. *The lattice Boltzmann equation: for fluid dynamics and beyond*. Oxford, UK: Oxford University Press.

Szymczak, P. and Ladd, A.J.C. 2003. Boundary conditions for stochastic solutions of the convection-diffusion equation. *Physical Review E* **68**(3): 036704. https://doi.org/10.1103/PhysRevE.68.036704.

Taylor, G.I. and Green, A.E. 1937. Mechanism of the production of small eddies from large

ones. *Proc. R. Soc. Lond. A* **158**(895): 499-521. DOI: 10.1098/rspa.1937.0036.

Tompson, A.F. and Gelhar, L.W. 1990. Numerical simulation of solute transport in three-dimensional, randomly heterogeneous porous media. *Water Resources Research* **26**(10): 2541-2562. https://doi.org/10.1029/WR026i010p02541.

Tompson, A.F., Vomvoris, E.G. and Gelhar, L.W. 1987. Numerical simulation of solute transport in randomly heterogeneous porous media: Motivation, model development, and application. No. UCID-21281, Lawrence Livermore National Lab., Livermore, CA.

Tungittiplakorn, W., Lion, L.W., Cohen, C. and Kim, J.Y. 2004. Engineered polymeric nanoparticles for soil remediation. *Environmental Science and Technology* **38**(5): 1605-1610. https://doi.org/10.1021/es0348997.

van Genuchten, M.T. and Wierenga, P.J. 1976. Mass transfer studies in sorbing porous media I. Analytical solutions 1. *Soil Science Society of America Journal* **40**(4): 473-480. doi:10.2136/sssaj1976.03615995004000040011x.

Verwey, E.J.W. and Overbeek, J.T.G. 1948. *Theory of the stability of lyophobic colloids*. Amsterdam: Elsevier Publishing.

Wiest, R. J. 1969. *Folw Through Porous Media*. New York: Academic Press.

Wildenschild, D., Vaz, C.M.P., Rivers, M.L., Rikard, D. and Christensen, B.S.B. 2002. Using X-ray computed tomography in hydrology: systems, resolutions, and limitations. *Journal of Hydrology* **267**(3-4): 285-297. https://doi.org/10.1016/S0022-1694(02)00157-9.

Wood, W.W., Kraemer, T.F. and Hearn, P.P. 1990. Intragranular diffusion: An important mechanism influencing solute transport in clastic aquifers. *Science* **247**(4950): 1569-1572. https://doi.org/10.1126/science.247.4950.1569.

Wu, K., Van Dijke, M.I., Couples, G.D., Jiang, Z., Ma, J., Sorbie, K.S., Crawford, J., Young, I. and Zhang, X. 2006. 3D stochastic modelling of heterogeneous porous media–applications to reservoir rocks. *Transport in Porous Media* **65**(3): 443-467. https://doi.org/10.1007/s11242-006-0006-z.

Xiao, F. and Yin, X. 2016. Geometry models of porous media based on Voronoi tessellations and their porosity–permeability relations. *Computers and Mathematics with Applications* **72**(2): 328-348. https://doi.org/10.1016/j.camwa.2015.09.009.

Yuan-Hui, L. and Gregory, S. 1974. Diffusion of ions in sea water and in deep-sea sediments. *Geochimica et Cosmochimica Acta* **38**(5): 703-714. https://doi.org/10.1016/0016-7037(74)90145-8.